SANDIA REPORT

SAND94-3266 · UC-704
Unlimited Release
Printed February 1995

2/22/95

*RECEIVED
FEB 27 1995
OSTI*

Dynamic Properties of Ceramic Materials

D. E. Grady

DISCLAIMER

Dynamic Properties of Ceramic Materials

D. E. Grady
Experimental Impact Physics Department 1433
Sandia National Laboratories
Albuquerque, NM 87185

Abstract

The present study offers new data and analysis on the transient shock strength and equation-of-state properties of ceramics. Various dynamic data on nine high strength ceramics are provided with wave profile measurements, through velocity interferometry techniques, the principal observable. Compressive failure in the shock wave front, with emphasis on brittle versus ductile mechanisms of deformation, is examined in some detail. Extensive spall strength data are provided and related to the theoretical spall strength, and to energy-based theories of the spall process. Failure waves, as a mechanism of deformation in the transient shock process, are examined. Strength and equation-of-state analysis of shock data on silicon carbide, boron carbide, tungsten carbide, silicon dioxide and aluminum nitride is presented with particular emphasis on phase transition properties for the latter two. Wave profile measurements on selected ceramics are investigated for evidence of rate sensitive elastic precursor decay in the shock front failure process.

3

4

Acknowledgments

The author would like to thank Marlin Kipp for providing most of the supporting computational analysis and Ron Moody For conducting the shock compression experiments.

Contents

1 Introduction and Summary

The current program focuses on the measurement of response properties of high-strength ceramic materials to support modeling activities facilitating computational and engineering analyses of ceramic structures under dynamic loads. As material response models and calculational methods mature, computational analysis will play an increasingly important role as cost-effective and time-efficient tools for the design, optimization, and evaluation of such structures.

The material response models for high-strength brittle solids are currently in a state of rapid development. A number of such models are currently available. A clear consensus as to the most appropriate modelling framework, or the critical deformation and equation-of-state features which must be implemented in these models, has not yet emerged.

Thus the present experimental study, in which controlled impact experiments and velocity interferometry diagnostics are used to acquire high-resolution shock compression data, is timely and performs several important functions critical to the development of adequate computational models for ceramic materials. First, a base of engineering dynamic strength and equation-of-state data is being acquired which establishes material constants necessary to all of the models. Second, time-resolved shock-wave profile measurements are being provided which are used to benchmark and validate existing computational models. Finally, and perhaps most importantly, the present shock-wave measurements provide a window into the physical mechanisms of dynamic deformation which are active in brittle solids subjected to transient impact loading. This latter contribution is critical to the thoughtful development of the most appropriate models for describing the dynamic behavior ceramic materials.

A range of activities has been completed since the last reporting period [Grady and Wise, 1993] which are included in the present report. Some were released earlier as Technical Memoranda while others have been prepared for recent technical conferences. References will be cited where relevant open literature is available.

In Section 2 previously unpublished shock compression and release profiles for aluminum oxide — Coors AD995 — are reported. The VISAR experiment used to measure the velocity histories is described and the data are used to examine the mechanisms of failure and deformation within the rise of the shock compression front. Although convincing arguments for neither ductile (dislocation processes) nor brittle (fracture processes with local loss of cohesion) failure in the shock front are available, the latter (brittle) mechanism is assumed. Microstructural features of the dynamic fracture process consistent with energy and time constraints are explored. Characteristic microfracture spacings and crack-opening displacements are developed.

In Section 3 the concept of failure waves, recently put forth and investigated experimentally be several authors, is considered within the context of uniaxial shock waves. The failure wave is examined within the context of both a subsonic wave and a delayed kinetic process. Previously reported stress (both axial and transverse) and particle velocity measurements associated with passage of the failure wave, along with kinematic constraints of

the uniaxial loading conditions, are used to reach the conclusion that dilatancy (a transfer of lattice strain to void volume) must accompany the failure wave process. Estimates of dilatant void volume for failure waves in glass are made.

Section 4 provides a discussion of the dynamic tensile (spall) strength of brittle solids. The planar-impact spall experiment is described and data for eight ceramics are provided. The spall data are compared with calculated theoretical spall strength values and a theory of the dynamic spall process based on both inherent flaw and fracture energy concepts is presented. Strain rate dependent relations between static tensile strength and spall strength for brittle solids is developed.

In Section 5 brittle fracture in the shock wave front is again assumed and the theory of Griffith for failure of a brittle solid under a general state of stress is examined. In particular the ratio of the Hugoniot elastic limit to the spall strength predicted by the Griffith failure criterion is calculated and compared with the experimental data for the ceramics reported in Section 4. The comparison is not inconsistent with brittle failure in the shock process.

Parts of Section 2, 4 and 5 are included in a paper prepared for a Workshop on Fracture and Damage in Quasibrittle Structures, Prague, Czech Republic, September 21-23, 1994, and was published in the Proceedings of that Workshop [Grady, 1994a].

Shock wave profile data for silicon carbide and boron carbide are presented in Section 6 and are used to examine the starkly different dynamic strength and shock equation-of-state properties of these two carbide ceramics. The wave profile signature of silicon carbide is characteristic of high strength metal behavior and is readily modeled with standard work-hardening elastic-plastic models. In contrast, post-yield dynamic flow properties of boron carbide suggest a catastrophic near or total loss of strength, and details of the VISAR measurement indicate a heterogeneous deformation process. The wave-profile measurements for boron carbide are open to other interpretations, however, and the possibility of an unusual shock-induced lattice compression (phase transition) needs to be considered further. The content of Section 6 was prepared for publication in the International DYMAT Conference proceedings, Oxford, England, September 26-30, 1994 [Grady, 1994b].

In Section 7 new shock-wave data for aluminum nitride ceramic, principally targeting dynamic effects of the hexagonal-to-cubic phase transformation under shock compression in this material, are presented. The principal effort in this study is concentrated on the modelling issues necessary to the presentation of this large $\Delta \upsilon$ phase change in computational simulations. Section 7 has also been published in the 1994 International DYMAT Conference [Kipp and Grady, 1994].

New shock equation-of-state and spall data for several liquid-phase sintered tungsten carbide ceramics are provided in Section 8. One material was extracted from the core of the BS-41 armor piercing round. The relatively low Hugoniot elastic limit, strong hardening characteristics, and large spall strength presumably reflect the metal-ceramic properties of this material.

In Section 9 several tests on silicon dioxide (quartz rock) are presented which focus on exploring a critical stress level in the shock-induced α-quartz-to-stishovite phase transition in this material. Features of this transition were previously reported by workers in the former Soviet Union [Zhugin and Krupnikov, 1987] using manganin gauge techniques, and the present effort was a cooperative study using VISAR diagnostics [Grady and Zhugin, 1994]. There are interesting technical reasons that this critical transition anomaly has eluded discovery in this country over the several decades of study concentrated on quartz and quartz rock materials.

In Section 10 new wave profile data along with previously reported data are examined for properties of elastic wave precursor decay in the shock compression of ceramics. This feature is believed to be a sensitive indicator of rate-dependent deformation in the shock-compression failure of materials. With the possible exception of boron carbide, the ceramics investigated indicate no, or very little, elastic precursor attenuation. These observations, in contrast to some of the results discussed in earlier Sections, are not consistent with a rate-sensitive fracture process in the shock front.

Taken collectively, the new results provided here offer an interesting perspective on the dynamic behavior of ceramic materials. Brittle versus ductile deformation in the shock front is still an open issue. Although magnitudes and relative levels of Hugoniot elastic limits and spall strengths are not inconsistent with brittle failure, the lack of rate sensitivity suggested by the precursor evolution data in Section 10 speaks strongly for plasticity processes in the shock front.

The spall failure of ceramic materials is clearly a brittle fracture process as is the unconfined compressive failure initiated under Hopkinson bar loading conditions. The failure wave may be the missing key in linking failure under shock compression to dynamic failure in the tensile and unconfined compressive environment. The characteristic time for the failure wave event is intermediate between the shock front failure process and the compression bar experiment. The identification of failure waves in ceramic materials other than glass, and determination of the related properties of failure waves are the critical next steps in uncovering the nature of shock-induced deformation of brittle solids.

Shock-induced solid state phase transformation is an integral component of the dynamic deformation of high-strength ceramics within the pressure range of interest in the present study. At least three, and possibly as many as six, of the nine ceramic materials referred to in the present report undergo shock-induced phase transitions. Work in progress indicates that the inclusion of phase transformation in the computational analysis of projectile-structure interactions can significantly influence predictions.

The outline above summarizes the key issues investigated in the present ongoing study. The work adds substantially to the body of data available on high-strength brittle materials. More importantly, the effort has identified critical research directions necessary to a fuller understanding of the dynamic compressibility of ceramics.

2 Failure in Ceramics in the Compressive Shock Front

A broad class of brittle solids (the attention here focuses principally on high-strength monolithic ceramics) subjected to large amplitude shock waves can support substantial shear stress (of order 5-15 GPa), and the accompanying elastic strain energy, within the compressive shock-wave front, without failing due to the very limited slip systems in these materials. When failure occurs under sufficiently intense shock loading, the effect is usually observed as a wave splitting in the compressive shock front, and details of the failure process can be inferred from features in the measured shock-wave profiles. Because of the high confining stress state associated with the failure event in the shock compression environment, it is no longer clear whether the microstructural processes of deformation are brittle or ductile. Some, although by no means sufficient, evidence supports a brittle deformation mechanism in the hard materials of interest within the range of present discussion. Other evidence, however, argues for microplasticity processes within the shock front.

If brittle mechanisms control failure in the shock front for a least some of the ceramic materials of interest, then details of the activation and growth of brittle fracture and flow in the shock compression process are poorly understood. Mechanisms for the shear failure process including the process-zone characteristics of individual shear cracks and fracture densities can only be surmised. In this Section we present new wave-profile data representative of the shock compression behavior of many high-strength ceramics. These data are used to explore some of the microstructural deformation issues of interest, and to provide estimates of shear fracture properties within the deformation shock wave.

2.1 Compression Waves in Ceramics

The compression failure in a ceramic body, subjected to a complex stress state, is achieved when some measure of the stress difference such as the octahedral shear stress,

$$\tau_{oct} = \frac{1}{3}\sqrt{(\sigma_x - \sigma_y)^2 + (\sigma_y - \sigma_z)^2 + (\sigma_z - \sigma_x)^2}, \tag{2.1}$$

achieves a critical condition which may depend, for example, on the mean stress, $p = (\sigma_x + \sigma_y + \sigma_z)/3$, the rate of loading, $\dot{\varepsilon}$, and the temperature of the body. One particularly unique loading path is achieved under a constraint of uniaxial strain in which the two transverse stress components are equal, say $\sigma_y = \sigma_z$, and are proportional to the axial stress according to,

$$\sigma_y = \frac{v}{1-v}\sigma_x, \tag{2.2}$$

where v is Poisson's ratio.

The latter stress loading path is of particular interest because it is readily achieved in the controlled planar impact of two plates and the technology for performing such experi-
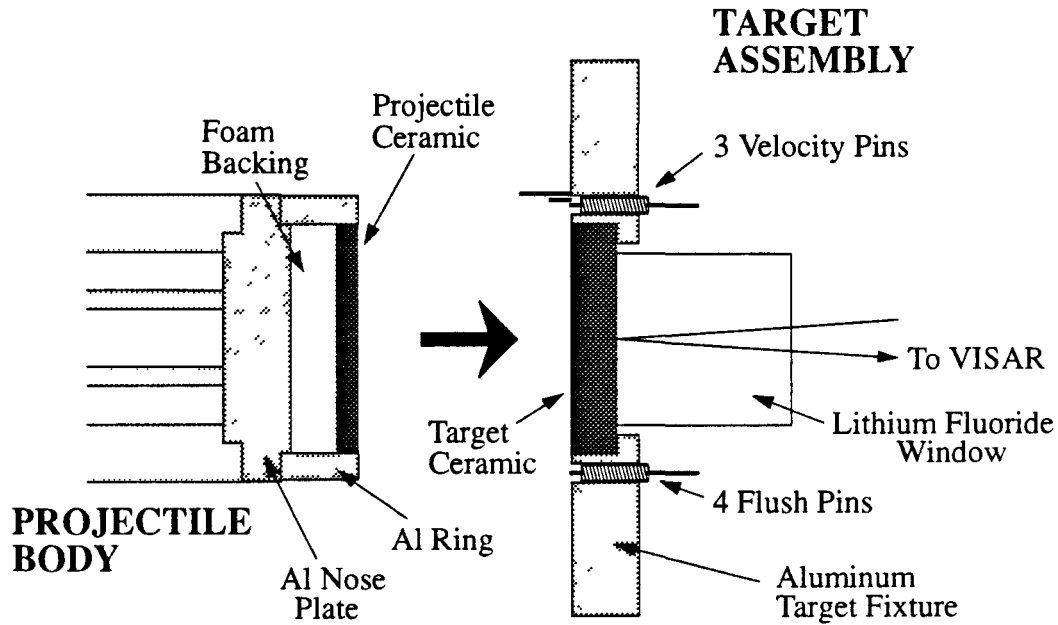
Figure 2.1   Experimental configuration for shock- and release-wave experiments on ceramic.

ments and diagnosing the consequences of such tests have achieved a mature state of development.

One test technology for probing the response of solids under uniaxial strain compression loading is illustrated in Figure 2.1 [Grady, 1992a; Grady, 1992b]. A disc of the ceramic being tested is mounted in the projectile and is supported on the main projectile body by a disc of low density polyurethane foam. For the target, a similar disc of the ceramic is mounted in the stationary supporting target fixture. An optical quality disc of single crystal lithium fluoride is intimately bonded with epoxy to the back of this ceramic sample. All critical surfaces are lapped and polished, and are typically flat to within a few bands of sodium light. The bonded lithium fluoride surface is first lightly diffused and vapor-deposited with about 100 nm of aluminum. The ceramic-lithium fluoride epoxy bond thickness is approximately 10 to 20 μm.

The ceramic-on-ceramic planar impact produces a compressive wave of uniaxial strain which propagates across the stationary ceramic specimen and through the ceramic-lithium fluoride interface. An equivalent compressive wave propagates through the projectile ceramic specimen and reflects at the low-impedance foam interface as a release wave which unloads the compressed ceramic. Dimensions of the ceramic discs are selected such that lateral release waves from the boundaries of the disc do not interfere with the central motion until after the primary experimental measurement is completed.

13

The compression and release wave behavior is measured by monitoring the time-resolved longitudinal motion at the center of the ceramic-lithium fluoride interface with laser velocity interferometry (VISAR) techniques [Barker and Hollenbach, 1972]. Measurements are recorded on transient digitizers. Lithium fluoride is used as the laser window material because, although its mechanical impedance is somewhat lower than the ceramic being tested, it is the only material which has been optically calibrated and which remains transparent when subjected to the 10 to 50 GPa shock stresses generated in the present experiments [Wise and Chhabildas, 1985].

The interference fringes measured with the VISAR system are converted to a time-resolved history of the velocity of the interface using the method of Barker and Hollenbach (1972), with a time resolution of approximately 1 ns. The amplitude resolution is approximately 2% per fringe and typically two to three fringes are achieved in the interface acceleration through the compressive shock front. From these records the dynamic stress and strain characteristics of the ceramics are determined through further computational and analytic techniques.
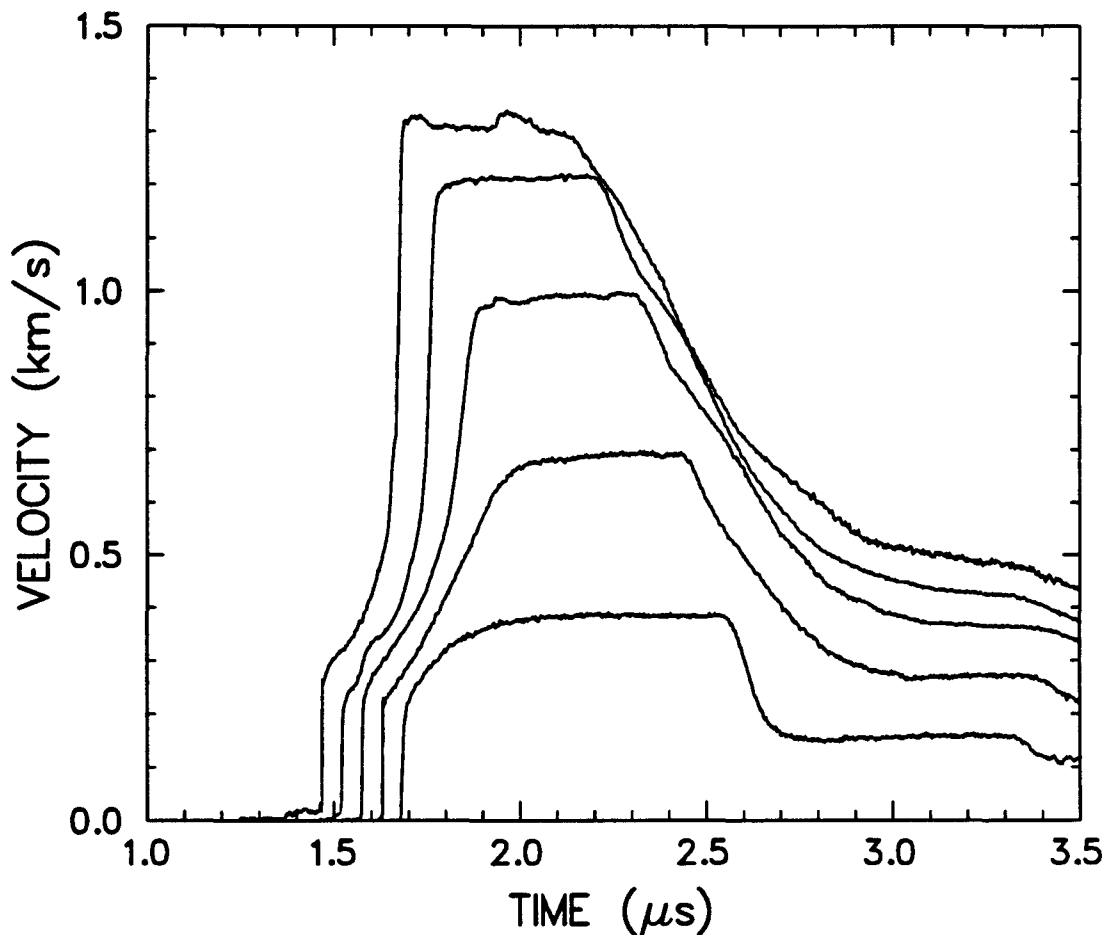

Figure 2.2   Shock-compression and release wave profiles for aluminum oxide measured with velocity interferometry (VISAR) diagnostics with the experimental configuration of Figure 1.

14

Measured wave profiles from a series of compression and release wave experiments performed on aluminum oxide ceramic are shown in Figure 2.2. The lowest impact velocity achieved a Hugoniot state just in excess of the Hugoniot elastic limit. The remaining experiments ranged up to Hugoniot states of approximately 40 GPa which is about six times the Hugoniot elastic limit of this material. The impact velocities and experimental dimensions for this series of experiments are provided in Table 2.1.

Table 2.1:
Shock Compression Wave-Profile Experiments on Aluminum Oxide Ceramic[1]

Test Number	Impact Velocity	Target[2] Thickness	Impactor[3] Thickness	Shock Velocity	Particle Velocity	Stress	Specific Volume
	(km/s)	(mm)	(mm)	(km/s)	km/s)	(GPa)	(m^3/Mg)
CE-57	1.070	10.006	5.019	8.54	0.535	19.1	0.242
CE-58	1.572	10.008	5.008	8.29	0.786	27.6	0.234
CE-59	1.943	10.007	5.013	8.56	0.972	34.1	0.229
CE-60	2.329	9.998	5.005	8.80	1.165	41.7	0.224
CE-61	0.561	9.987	4.989	9.18	0.281	11.0	0.250

[1] The material tested was AD-995 ceramic provided by Coors Porcelain Company. The density is 3890 kg/m^3, longitudinal elastic velocity is 10.56 km/s, and shear velocity is 6.24 km/s.
[2] Lithium fluoride windows 25.4 mm in thickness and 50.5 mm in diameter were used in all tests.
[3] Polyurethane foam densities backing impactors were 320 kg/m^3 for Tests CE-57, 58, 59, 61 and 640 kg/m^3 for Test CE-60.

The wave profile data as shown in Figure 2.2 can be used to determine the Hugoniot properties of the aluminum oxide ceramic. Here Hugoniot states refer to the peak stress versus specific volume states achieved in the shock compression process. The amplitude of the initial precursor corresponds to onset of shear failure (the Hugoniot elastic limit) and for the present aluminum oxide ceramic was determined to be 6.2 ±0.4 GPa while the precursor velocity was determined to be 10.74 km/s. Hugoniot states calculated from the wave profile data are provided in Table 2.1.

Both the Hugoniot elastic limit and the subsequent final stress versus specific volume Hugoniot states are shown in Figure 2.3. The shock data can be compared with the static x-ray diffraction data to 12 GPa on sapphire of Sato and Akimoto (1979). The latter static data have been extrapolated to 30 GPa with a Birch-Murnaghan equation of state to provide a measure of the hydrostatic compressibility of Al_2O_3. The offset between the static and shock data illustrates, and is commonly used to assess, the sustained nonhydrostatic stress state following the shock compression wave alluded to in the opening paragraph of this section. Shock temperature would account for less than 0.1 GPa of the offset. Impuri-
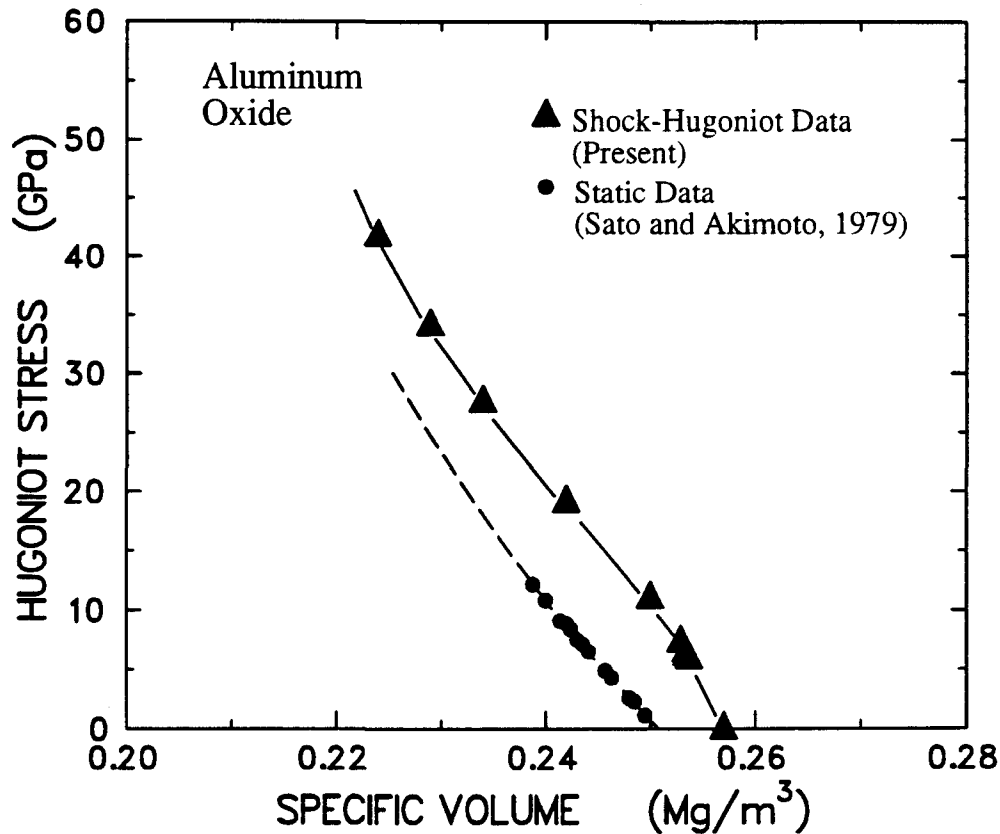
Figure 2.3   Hugoniot states for shock-compressed aluminum oxide compared with extrapolation of hydrostatic x-ray diffraction data.

ties and porosity, however, can seriously complicate a detailed evaluation of the deviator stress state under shock compression by this method.

2.2   Compression Failure Process

It is the compressive failure and deformation properties of ceramics under the shear stress loading brought about by the shock compression process which contributes to the richness in the compressive shock-wave characteristics of these materials. Volumetric lattice compressibility for the intermetallic light weight compounds of interest is usually a decreasing function of pressure in the shock stress range of concern, and would, of itself, lead to the propagation of a single steady shock wave. The exception occurs in those materials in which phase changes brought about by lattice instabilities at critical levels complicate the volumetric compressibility, a not uncommon occurrence in the present intermetallic compounds.

As compression within the shock front increases during the shock loading process in materials with strength, shear stresses will ultimately achieve levels in excess of the critical strength of the material. Stresses will be amplified at microscopic defects within the solid, and at these points inelastic deformation accompanied by stress relaxation will lead to per-

16

vasive shear failure in the material. It is these deformation-induced convexities in the stress-versus-strain curve for ceramics which provide the complexities observed in the compression wave-profile structure.

Features of inelastic shearing slip emanating from defects within the shock front can be identified as ductile or brittle. Ductile slip is associated with shearing motions in which material displacements normal to the slip planes never exceed atomic dimensions and such that material cohesion is retained. Brittle slip (or shear fracture), in contrast, involves the normal separation of material points over dimensions in excess of atomic dimensions; consequently, cohesion of the material is lost and internal stress-free surfaces are introduced.

Metals are generally associated with ductile failure, while ceramics are usually considered to be brittle. This intuitive classification becomes less certain, however, when a confining pressure component of the stress field is considered. In principle, sufficient confining pressure can be applied to cause any material to undergo a brittle-to-ductile transition. Consequently, the possibility of ductile shear failure within the shock front in ceramics cannot be ruled out.

Spall experiments, in which shock wave tests were designed to first dynamically compress the specimen and then test the tensile strength of the specimen, have been used to examine the residual cohesion of a material after shock compression. It has been argued that the loss of spall strength observed in numerous ceramics, when first shock compressed above the Hugoniot elastic limit, supports a brittle failure process in the compressive failure of ceramics. However, even these results are not unambiguous since reverse shear yield is usually achieved on decompression before a tensile axial stress is achieved. The significantly lower confining pressure associated with the reverse yielding would much more readily accommodate brittle failure and loss of cohesion than would the initial failure on shock compression.

The reasonable agreement of shock compression spall and Hugoniot elastic limit data with predictions based on a Griffith brittle failure criterion to be presented in a subsequent section might also be construed as further evidence for shear fracture in the shock compression process. Even here the evidence is weak and other explanations are possible.

Nevertheless, shear fracture during the shock compression process does appear to be a viable mechanism for inelastic deformation, and speculation on physical details of the fracture mechanisms in the shock front is worth pursuing. The shock compression profile in ceramics generally looks like the example for aluminum oxide shown in Figure 2.4(a). There are notable exceptions, however. Boron carbide, for example, is observed to exhibit marked stress softening in post-failure behavior under shock compression [Grady, 1992b; Grady, 1994].

The compressive wave profile is characterized by three distinct regions. The first is a sudden elastic rise to the failure limit or Hugoniot elastic limit. (The experimental definition of the Hugoniot elastic limit is discussed further in Section 10.) For high-strength ceramics elastic stresses of 5-20 GPa are achieved at failure with corresponding elastic volume

17

and shear strains of about 2%-5%. Second, the failure ramp identifies a region of rapidly changing compressibility, although only small additional strains are accommodated by the material during passage of this wave segment. It is likely that only precursors to the inelastic failure process occur within this time such as incipient fracture incubation and nucleation processes. Finally, formation of a steady rapidly-rising deformation shock is demanded by the intrinsic nonlinearity and upward concavity of the volumetric elastic compressibility of the solid. The preponderance of inelastic shear deformation due to shear fracture growth is presumed to be accommodated within the deformation shock wave. The width of this wave segment is governed by kinetic and time-limited deformation processes.
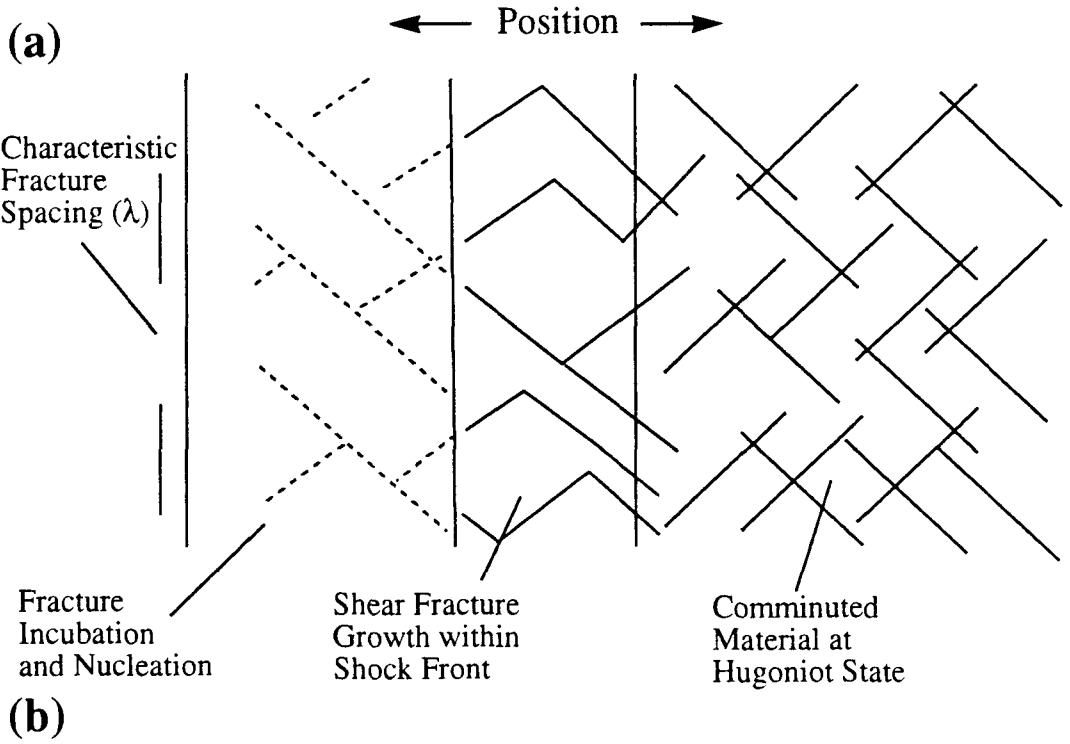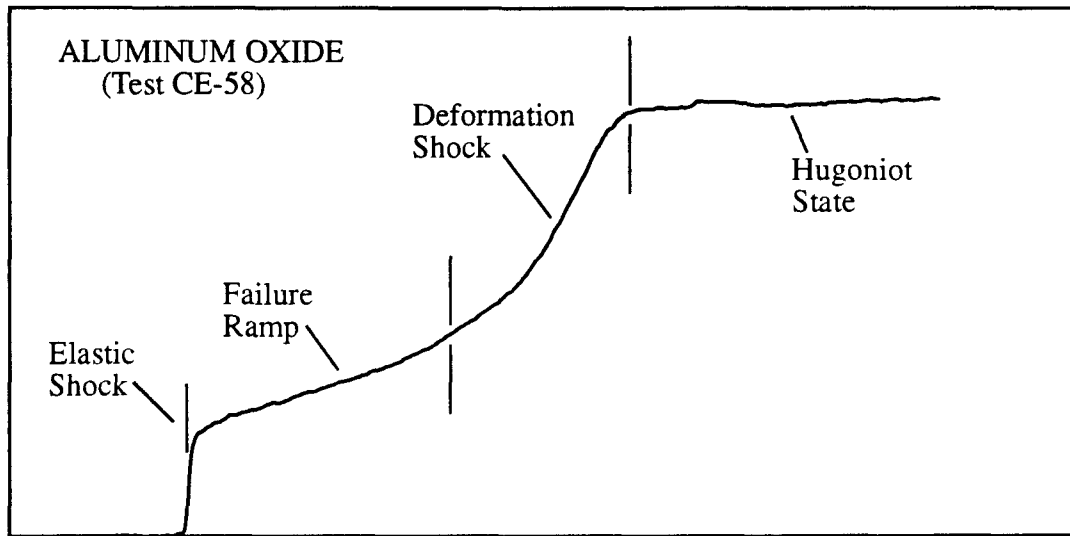

Figure 2.4   Shock wave compression profile for aluminum oxide (a) and schematic of brittle shear fracture process within the shock-wave front (b).

18

A reasonable physical model of the shear fracture process within the shock front is shown in Figure 2.4. Figure 2.4(a) illustrates the stress (or particle velocity) wave profile propagating toward the left through the solid. Material to the left of the elastic front is undisturbed. Material to the right is fully comminuted due to passage of the shock. Shear fracture incubation and nucleation occurs within the failure ramp — mature shear cracking and inelastic fracture deformation follows within the deformation shock wave.

In the failure ramp and the early deformation shock wave, confining pressures are of order 3 - 10 GPa and can rise to values of 30 - 60 GPa or more as the Hugoniot state is approached. Clearly then, the material must be capable of locally (microscopically) supporting stress gradients of this same order if material displacements consistent with brittle deformation and loss of cohesion are to occur in the zone of fracture. Such behavior could readily be accommodated in microscopic shear fracture if a film of ultra-fine debris were generated within the fracture process zone and persisted to support the walls of the shear fracture during mature growth and subsequent arrest as illustrated in Figure 2.5.

Size of the fracture zone debris and width of the fracture can be bounded from the size dependence of the strength of brittle objects based on energy balance arguments,

$$\delta = \frac{2E\gamma}{P_e^2},$$ (2.3)

where δ is the characteristic debris size, E is the elastic modulus, γ is the cohesive surface energy and P_e is the effective stress determining the elastic strain energy within the supporting particle. Based on $E = 400$ GPa and $\gamma = 5$ J/m^2, which are appropriate properties for aluminum oxide, and P_e equal to the local confining pressure of about 5-10 GPa, a characteristic particle size and fracture zone dimension of $\delta \sim 40\text{-}160$ nm is calculated. Values for P_e appreciably higher than the confining pressure would be expected due to stress concentration near the environment of the supporting particles and, consequently, estimates for δ probably represent an upper bound. A small degree of local dilatancy is expected to accommodate the shear-fracture free volume. The parameter δ will decrease through the deformation shock as confining pressures approach the Hugoniot state. The corresponding crushing of fracture zone debris would lead to local energy dissipation and elevated temperatures. Under certain material conditions localized melting and transition to near fluid shear zones within the fracture region late in the deformation shock may be expected [Grady, 1980].

The characteristic spacing of fractures in the shock process zone λ (see Figure 2.4(b)) may be predictable from an energy balance approach to fragmentation which has been successful in other applications [Grady, 1982; Grady, 1988]. The theory leads to,

$$\lambda = \left(\frac{48\gamma}{\rho\dot{\varepsilon}^2}\right)^{1/3},$$ (2.4)

based on the shearing strain rate $\dot{\varepsilon}$ in the shock wave and the fracture energy γ. The strain rate can be calculated from $\dot{\varepsilon} \approx 3\Delta\sigma_m/2\eta$ where η is the solid viscosity within the shock

19
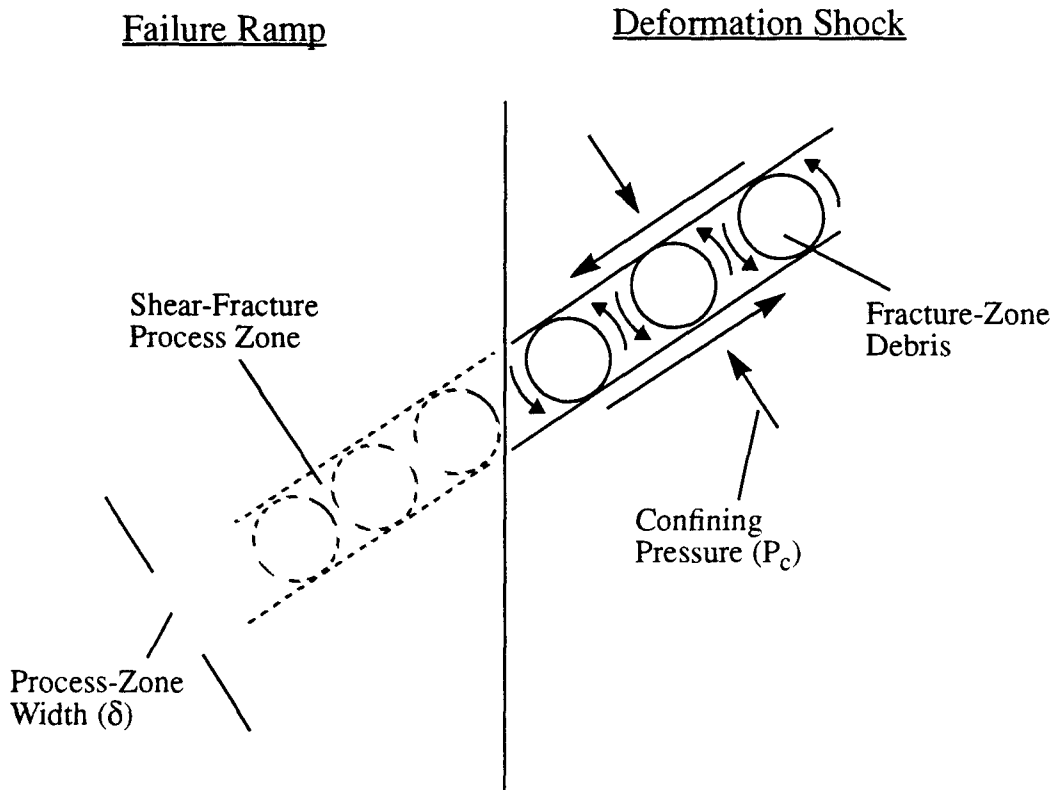
Figure 2.5   Indicates the incubation and growth of shear fracture in
the ramp and deformation shock front.

front and $\Delta\sigma_m$ is the stress jump through the deformation shock wave. Although properties in the shock which determined this viscosity are not understood, measurements of shock widths in brittle materials can be used to estimate deformation strain rates.

For example, in the aluminum oxide reported in the present work (Figure 2.2), a shock state of 19 GPa leads to a strain rate in the shock front of about 1.7×10^5/s and a fracture spacing from Equation 2.4 of approximately 130 μm. In contrast, the highest shock stress of 42 GPa yields a shock front strain rate in excess of 1.0×10^7/s and a fracture spacing of less than 8 μm. Material parameters of $\rho = 3890$ kg/m^3 and $\gamma = 5$ J/m^2 were used in Equation 2.4. Such predictions of fracture spacing exceed the fracture process zone dimension δ by about three orders of magnitude and at the lower strain rates are well above the characteristic grain size of this material.

20

3 Failure Waves

The emergence and evolution of structure in a compressive shock wave such as illustrated for aluminum oxide in Figure 2.2 is critically dependent on the amplitude of the input stress load. If the input stress level is less than the Hugoniot elastic limit, it is expected that an elastic wave of finite amplitude will propagate in the brittle solid. This expected response for waves of uniaxial compression has been brought into question by recent experimental shock wave studies on K-2 glass by Kanel′ et al. (1992). That work has provided evidence for the propagation of a delayed front of fracture following the initial elastic compression wave. This new, and not yet well understood, phenomenon has been identified as a failure wave, and is presumed to be a shear fracture process which is driven by the large shear strain energy residing in the body behind the large-amplitude elastic uniaxial-strain compression wave.

Further evidence supporting the observations of Kanel′ and coworkers has been provided by the studies of Brar et al. (1991) on a similar soda-lime glass, and those of Raiser et al. (1994) on an alumina-silicate glass. In the former work, transverse stress gages provided definitive evidence for substantial increase in the transverse stress component σ_y upon passage of the failure wave, thus significantly reducing the shear stress $\tau = (\sigma_x - \sigma_y)/2$. Brar et al. (1991) also tested the tensile strength of glass behind the initial elastic shock wave both before and behind the failure wave through the appropriate design of the spall experiments. These tests indicated a tensile strength in excess of 3 GPa for glass in front of the failure wave and nearly zero strength behind, suggesting a transition to fully comminuted material following passage of the failure wave. Failure wave effects were noted by Brar et al. (1991) for soda-lime glass for compressive stress levels in excess of about 4 GPa but below the Hugoniot elastic limit of approximately 6.5 GPa. Raisor et el. (1994) investigated surface roughness effects at the impact as a source for initiation of the failure wave but found no influence. Spall experiments on alumina-silicate glass before and behind the failure wave were also in agreement with the results of Brar et al. (1991).

Earlier researchers have suggested that the failure wave may be a propagating fracture front trailing the initial elastic shock wave at a velocity substantially less than the shock velocity [Kanel′ et al. 1992]. A failure wave velocity closer to the Rayleigh wave speed has been proposed [Raisor and Clifton, 1993] although evidence for this result is not yet convincing.

A viable alternative is that the delay time between the shock wave and failure wave is governed by the kinetics of fracture nucleation and growth. Incubation of the shear fracture process would initiate immediately after passage of the elastic shock front. The failure wave occurring somewhat later would then manifest the catastrophic fracture growth phase accompanied with observable changes in the longitudinal and transverse stress state.

Thus, the dwell time between shock front and failure wave could be loosely likened to the ramp region of the higher amplitude wave profile illustrated in Figure 2.4. It is a regime of

the profile in which time-dependent preparatory conditions are being established prior to the pervasive dynamic shear failure process.

The reported changes in the state of material upon passage of a failure wave are difficult to reconcile without rather unusual assumptions regarding material response. Several of the critical observations are:

(1) Velocity interferometry measurements indicate small or negligible change in particle velocity through the failure wave.

(2) Transverse and normal stress measurements indicate that the stress difference $\sigma_x - \sigma_y = 2\tau$ reduces substantially during passage of the failure wave but most of the change is due to an increase in σ_y; there is little change in σ_x.

(3) The failure wave is reported to propagate at a velocity significantly reduced from the longitudinal elastic velocity in glass. Values of order 2 km/s have been inferred from experimental data. The evidence here is weak and any velocity up to the longitudinal sound velocity — including time and ampitude dependence — should be considered possible.

Consider the possibility that the material response leads to a failure wave with a characteristic velocity $V_{failure}$, and that passage of the failure wave corresponds to a complete loss of the stress deviator. If the volumetric compressibility behind the failure wave continues to correspond to fully dense glass then the situation shown in Figure 3.1(a) will apply. State 1 precedes the failure wave and state 2 is achieved following the passage of the wave. The velocity of the failure wave is determined from the slope of the chord connecting state 1 and state 2 according to,

$$V_{failure} = \sqrt{\frac{\Delta\sigma}{\rho\Delta\varepsilon}}.$$

(3.1)

The difficulty with this assumed behavior is that a significant increase in particle velocity $(\Delta u = \Delta\varepsilon V_{failure})$ would be expected which is not consistent with the first observation.

A second possibility is that material behavior through the failure wave represents the catastrophic relaxation of the shear stress due to a time-dependent fracture nucleation and growth process. Consider the possibility in Figure 3.1(b) in which complete relaxation of the stress deviator at constant strain is achieved through the failure wave. Again, in order to achieve the volumetric compression curve of fully dense glass identified as state 2 in Figure 3.1(b), one of the critical observations is violated. Namely, a substantial drop in σ_x through the failure wave — approximately twice the increase in σ_y.

There is another possible material behavior, illustrated in Figure 3.1(c), which could be consistent with the three experimental observations. This explanation involves a change in the volumetric compressibility through the failure wave. The alternative pressure (mean stress) versus volume curve is initiated due to shear fracture induced dilatancy in the failure wave. As illustrated in Figure 3.1(c), the process could lead to a fixed failure wave velocity and occurs with small changes in particle velocity and longitudinal stress through the failure wave. The dilatant void volume required to accommodate the behavior can be

22
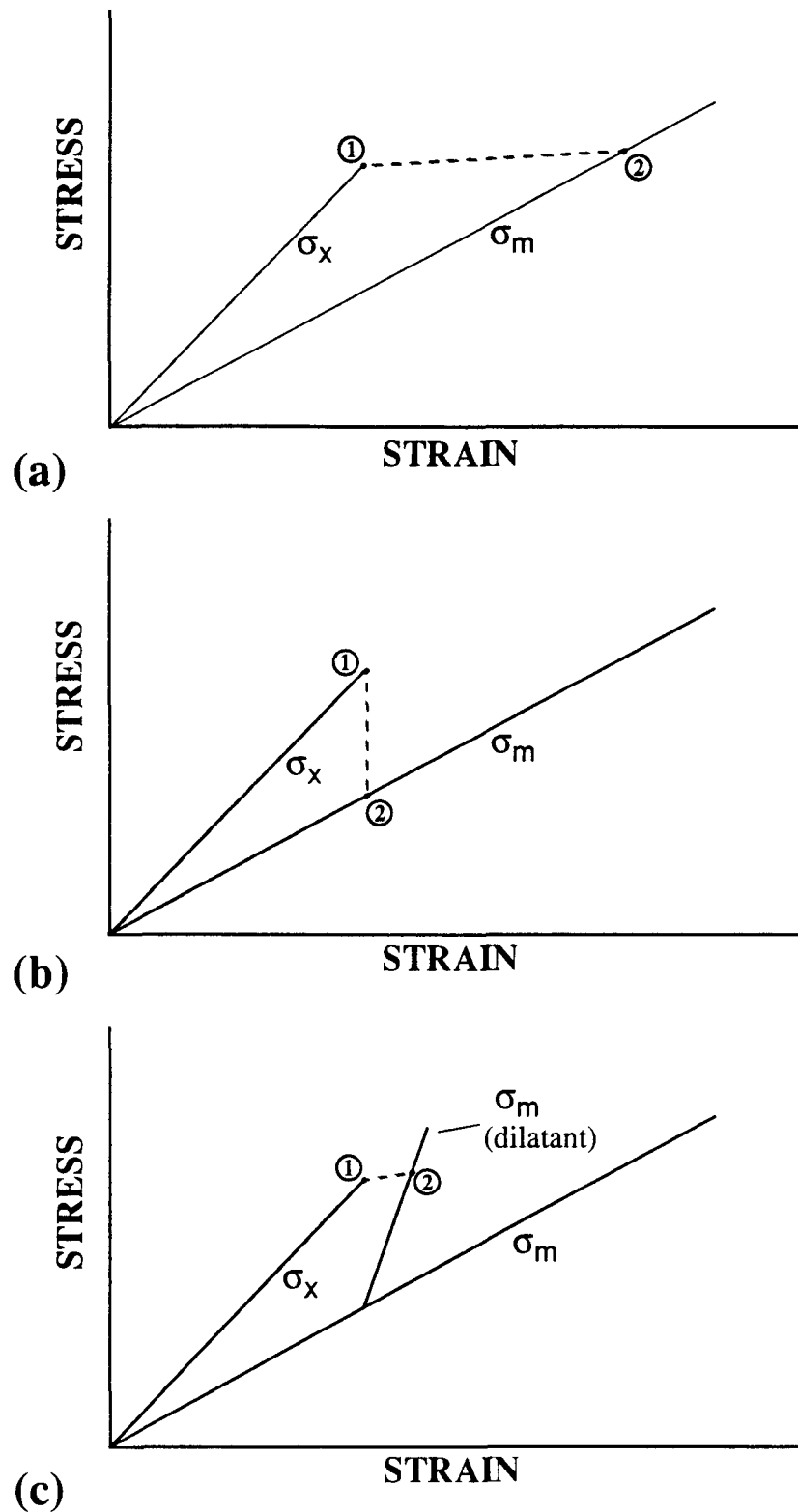
Figure 3.1   Transition states for failure waves in brittle solids. In each example the shock state at point one is below the Hugoniot elastic limit. σ_x and σ_m represent uniaxial strain and mean stress loading paths, respectively.

estimated. A pressure change is related to volumetric lattice strain υ_{lat} through the bulk modulus K according to

$$dp = -K\frac{d\upsilon_{lat}}{\upsilon_{lat}}, \qquad (3.2)$$

However, if dilatant void volume $d\upsilon_{dil}$ is introduced, the total specific volume change is $d\upsilon = d\upsilon_{lat} + d\upsilon_{dil}$ and

$$dp = -\frac{K}{\upsilon_{lat}}(d\upsilon - d\upsilon_{dil}) . \qquad (3.3)$$

For the purpose of simplicity assume a constant strain process through the failure wave, $d\upsilon = 0$, and,

$$\frac{d\upsilon_{dil}}{\upsilon} \cong \frac{dp}{K} . \qquad (3.4)$$

If it is further assumed that $d\sigma_x = 0$ and that $\sigma_x = \sigma_y$ after passage of the failure wave, then $dp \cong 4\tau/3$, where τ is the shear stress in the elastic state preceding the failure wave, and

$$\frac{d\upsilon_{dil}}{\upsilon} \cong \frac{4}{3}\frac{\tau}{K} . \qquad (3.5)$$

For glass shocked to about 5 GPa on the Hugoniot, $\tau \approx 1.7$ GPa, $K \approx 56$ GPa, predicting a dilatant strain of about 4%. The complete transfer of elastic shear strain energy to dilatant strain energy yields a comparable result.

The concept of failure waves clearly contributes an intriguing added dimension to the processes of dynamic failure of brittle solids, and extends a challenge to the emerging constitutive models intended to describe such failure. Further experimental effort is needed to more carefully constrain the observable features of failure waves. Dilatant inelastic strain within the compressive failure process should be examined further. It is critical to identify other materials in which the effect occurs.

4 Dynamic Spall Process

Shock compression techniques also offer the unique opportunity of testing the dynamic tensile properties of matter without the complications of sample structure or surface preparation considerations. In the high-strength ceramics, dynamic tensile (spall) strengths are typically about one to two orders of magnitude lower than the corresponding dynamic compressive strength. Spall strengths have previously been related to fracture surface energy with some success [Grady, 1985; Grady, 1988], and such comparisons are examined further in the present work with spall data for selected ceramics.

4.1 Spall Strength of Ceramics

When an isolated and stationary plate of test material is impacted by a thinner plate of a selected impact material, shock waves are created in both samples at the impact plane. The transmitted shock waves reflect as waves of decompression at the respective free surfaces, meet within the thicker plate, and carry the interior plane at the collision point of the waves rapidly into tension. If the tensile stress and duration is sufficient, interior frac-
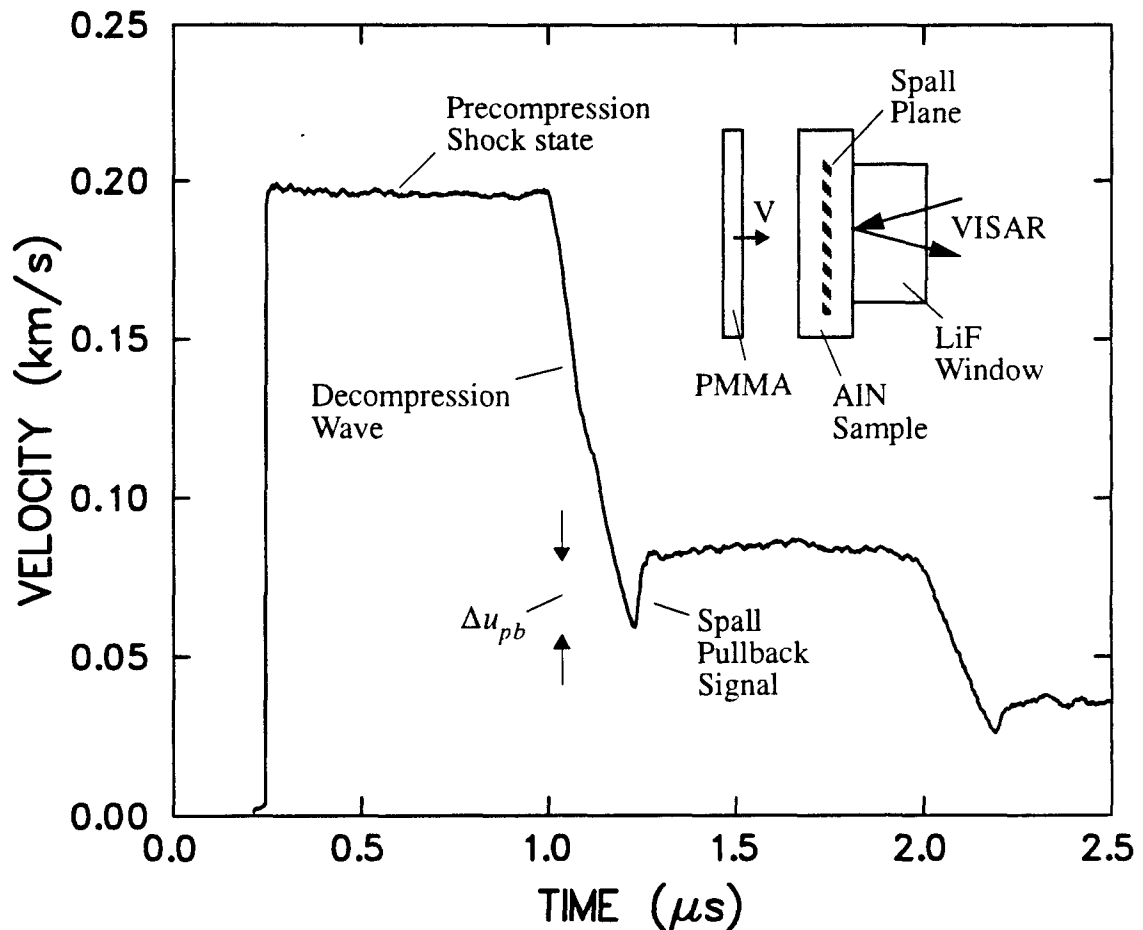
Figure 4.1   Velocity interferometry profile for a dynamic tensile fracture experiment in aluminum nitride ceramic illustrating elastic shock precompression and subsequent spall signal.

tures will nucleate, grow and coalesce at this plane, causing material separation and relaxation of the tensile stress to zero.

Such a spall experiment can also be performed if a low impedance VISAR window material is bonded to the back of the stationary test plate — the amplitude of the reflected decompression wave is determined by the impedance difference between the sample and window plates. The resulting interface velocity profile from such a spall experiment, in which a plate of aluminum nitride ceramic backed by a lithium fluoride transparent window material was subjected to planar impact by a thinner plate of polymethyl methacrylate (PMMA), is shown in Figure 4.1. Laser velocity interferometry (VISAR) was used to monitor the interface velocity history.

The initial jump in velocity amplitude quantifies the magnitude of the precompression shock wave. The release wave feature identified as the pullback signal images, at the recording interface, the tension magnitude and duration occurring at the spall plane. Spall strength values are calculated from the tensile magnitude of this signature through consideration of material impedance differences [Grady and Kipp, 1993]. To first order the spall stress can be calculated from,

$$\sigma_{sp} = \frac{1}{2}(Z_s + Z_w)\Delta u_{pb},$$ (4.1)

where Z_s and Z_w are the elastic impedances of the sample and window, respectively, and Δu_{pb} is the magnitude of the pullback signal as seen in Figure 4.1. Further discussion of experimental spall relations is provided in Section 8 of this report which deals with wave profile measurements on tungsten carbide.

Spall data for selected ceramics are provided in Table 4.1. The shock precompression in the experiments providing this spall data was appreciably less in magnitude than the corresponding Hugoniot elastic limit for the material. For later comparisons Hugoniot elastic limit data are also provided along with other selected properties.

4.2 Calculations of Spall Strength

If the interior of a crystalline body is subjected to a tensile stress, and if the body is free of microstructural or atomic defects, then the spall strength of that body is determined by the forces necessary to overcome the molecular cohesive energy of the material. One estimate for the magnitude of this spall strength is provided by the approximation of Orowan (see Lawn and Wilshaw (1975)),

$$\sigma_{th} \approx \frac{E}{\pi}.$$ (4.2)

This expression is recognized to over-estimate the theoretical tensile strength and more reasonable values based on models of the intermolecular forces have been obtained. Such studies have been performed for ceramics [Izotov and Lazarev, 1985; Kozhusko et al., 1987] and theoretical tensile strengths σ_{th} from their work are provided in Table 4.1.

26

Table 4.1:
Elasticity and Dynamic Strength Properties of Ceramics

	ρ (kg/m^3)	E (GPa)	ν	b_c (nm)	σ_{th} [1] (GPa)	σ_{hel} (GPa)	σ_{sp} (GPa)	γ_{th} [2] (J/m^2)	γ_{meas} (J/m^2)
AlN	3250	321	.24	.19	44.9	7-9	0.5-0.6	1.2/6.2	28-48
Al$_2$O$_3$	3970	401	.24	.19	59.5	11-12	0.5-0.8	2.1/7.7	15-61
B$_4$C	2510	462	.17	.16	64.5	17-19	0.4-0.5	1.4/7.5	23-40
SiC	3120	434	.16	.19	55.9	15-16	0.3-0.4	1.4/8.4	7-17
SiO$_2$	2630	90	.08	.16	24.0	7-9	.08-.11	1.0/1.5	5-14
TiB$_2$	4510	523	.05	.24	42.6	14-17	0.4-0.5	0.8/12.7	20-34
WC	14930	627	.21	.25	52.2	4-6	2.5-3.0	1.0/15.9	490-845
ZrO$_2$	6030	218	.31	.20	69.4[3]	13-16	1.5-1.9	4.4/4.4	640-1300

[1] Izotov and Lazarev, 1985 (see text).
[2] Equation 4.12/ Equation 4.4 (see text).
[3] Based on $\sigma_{th} = E/\pi$ (see text).

Measured spall strengths of engineering ceramics (as provided in Table 4.1) are observed to be about two orders of magnitude lower than the theoretical strengths, indicating that the inherent or induced flaw structure of the material is crucial in determining the dynamic tensile strength of ceramics.

High quality ceramics are usually exceedingly homogeneous. It is only on the microstructural scale that material heterogeneities emerge which are responsible for the stress concentrations that nucleate internal fracture and spall. Influence of the flaw structure on the spall strength may also depend on the rate of tensile loading during the spall process.

The strain rate and flaw structure sensitivities of spall in brittle materials which have emerged from previous theoretical studies can be explored within the context of the plot in Figure 4.2. For an unflawed material the spall strength will reside on the theoretical strength curve (upper curve in Figure 4.2) as discussed previously. In general the spall strengths of engineering ceramics fall within the bounding curves identified.

The fracture-producing flaw structure of a ceramic plays a critical role in the processes of spall failure. Such a flaw structure may be inherent due to defects, incompatibilities, or internal stress states in the initial microstructure. In addition, flaw structure may be induced by large-amplitude compressive shocks which precede dynamic tensions and can cause microstructural compressive fracture damage.

A possible extension of the latter is the failure wave following the compressive shock which would be expected to dramatically alter the flaw structure. In either case the materi-
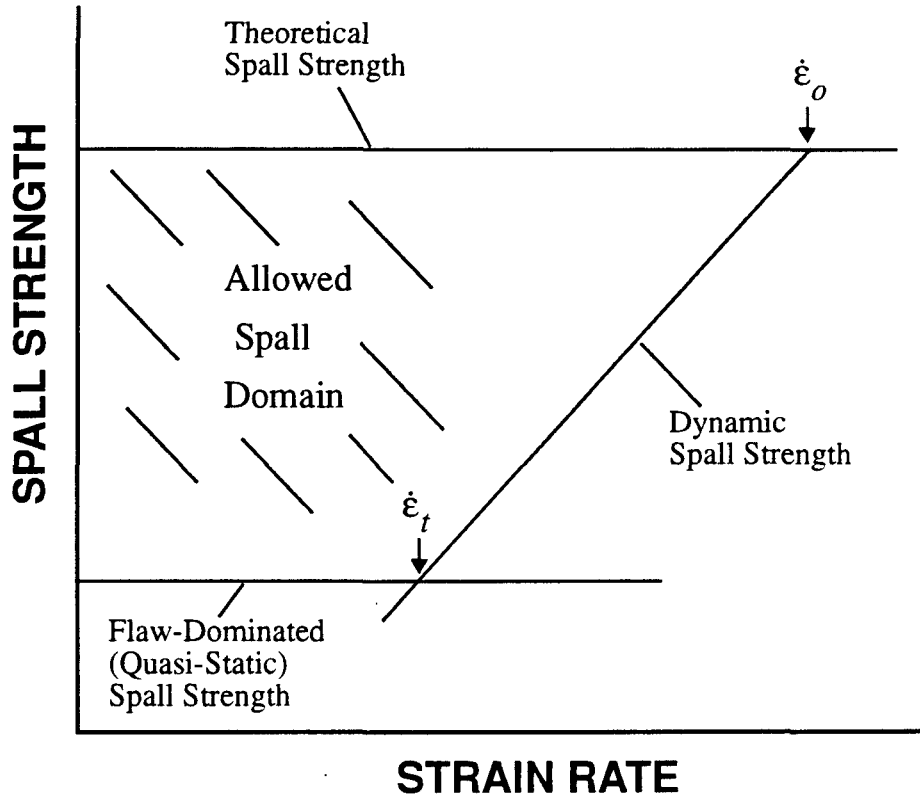
Figure 4.2   Regions of spall behavior inferred from energy-based theories of tensile failure of brittle solids.

ized by a critical flaw size a_c. The characteristic length a_c is regarded as a property of the material which leads to catastrophic spall fracture when a Griffith criterion,

$$\sigma_{sp} = \sqrt{\frac{\pi E \gamma}{2 a_c}},$$ (4.3)

is achieved, and when strain rates in tension are sufficiently low. Equation 4.3 is based on the solution for internal penny-shaped cracks of radius a_c. The parameter γ is the surface energy which must be overcome by the elastic strain energy to initiate fracture growth, and is also a property of the material.

In the limit of ideal brittle fracture the surface energy is that necessary to separate molecular planes over the cohesion dimension b_c and, from the Orowan analysis [Lawn and Wilshaw, 1975], is estimated to be,

$$\gamma = \gamma_{th} = \frac{b_c \sigma_{th}^2}{E}.$$ (4.4)

More generally, extension of a fracture involves additional dissipation through plasticity or comminution processes and the fracture surface energy can be written as,

28

$$\gamma = \alpha \gamma_{th},$$

(4.5)

where α is greater than unity.

Using Equation 4.3-4.5 the relation for spall strength can be scaled to the theoretical tensile strength of the unflawed crystal,

$$\sigma_{sp} = \sqrt{\alpha \frac{\pi}{2} \frac{b_c}{a_c} \sigma_{th}}.$$

(4.6)

For $\alpha = 1$ (theoretical surface energy γ_{th}) the spall strength is provided by the lower horizontal line in Figure 4.2. For dissipative fracture ($\alpha > 1$), the spall strength will lie within the interior of the region.

When tensile strain rates achieve levels in which the characteristic crack of dimension a_c no longer responds in a quasi-static manner to the time-varying stress field, spall strengths are predicted to become dependent on the tensile loading strain rate and independent of the length scale a_c. Strain rate dependent spall has been investigated through the time-dependent stress intensity factor of a single crack [Kipp et al., 1980], through statistical crack distributions [Grady and Kipp, 1989], and, more recently, through thermodynamic energy conditions for spall fracture [Grady, 1988]. These studies all suggest the same functional dependence for the spall strength, and the latter provides the strain rate dependent criteria,

$$\sigma_{sp} = \left(6\rho^2 c^3 \gamma \dot{\varepsilon} \right)^{1/3}.$$

(4.7)

Again $\gamma = \alpha \gamma_{th}$ is the surface energy dissipation in crack extension, and c is the elastic wave velocity.

Equation 4.7 predicts a spall strength which is independent of the length scale characterizing the flaw structure at sufficiently high strain rates. This strain-rate regime is bounded from below by the transition strain rate $\dot{\varepsilon}_t$ to the flaw-dominated strength and from above by the critical strain rate $\dot{\varepsilon}_o$ shown in Figure 4.2. The spall strength resides on this line when $\gamma = \gamma_{th}$ and above it otherwise. The dynamic spall strength converges to the theoretical strength when the higher strain rate is approached. The dynamic (high-strain-rate) spall strength can be related to the theoretical strength,

$$\sigma_{sp} = \left(\alpha \frac{\dot{\varepsilon}}{\dot{\varepsilon}_o} \right)^{1/3} \sigma_{th}.$$

(4.8)

The critical strain rate $\dot{\varepsilon}_o$ can be interpreted as the rate at which the velocity of separation of atomic planes is such that the kinetic energy of relative separation is comparable to the cohesive energy. This threshold strain rate,

29

$$\dot{\varepsilon}_o = \frac{1}{6}\sqrt{\frac{\gamma_{th}}{\rho b_c^3}},$$ (4.9)

is functionally the same as the crystal Debye frequency and numerically similar. The assumption of reasonable properties for ceramics (see Table 4.1) yields an $\dot{\varepsilon}_o$ of the order of $10^{12}/s\text{-}10^{13}/s$ — well above the strain-rate range experienced in application. The excess surface energy parameter α can be expected to depend on strain rate since the spall strength cannot exceed the theoretical strength in Equation 4.8.

A lower transition to flaw-dominated spall, characterized by the dominant flaw length scale a_c, occurs at the strain rate,

$$\dot{\varepsilon}_t = \frac{1}{6}\sqrt{\left(\frac{\pi}{2}\right)^3 \frac{\gamma_{th}}{\rho a_c^3}}.$$ (4.10)

Equation 4.10 would also be applicable for $\gamma = \alpha\gamma_{th}$ by replacing γ_{th} with γ. Assuming the reasonable values of $\gamma_{th} = 5\ J/m^2$, $\rho = 4000\ kg/m^3$, and $a_c = 10\ \mu m$ leads to an $\dot{\varepsilon}_t \sim 10^5/\sigma$. Thus characteristic flaw dimensions in excess of about 10 μm are expected to be necessary to accommodate the dynamic spall behavior predicted by Equation 4.7 since strain rates of this order are typically achieved in the impact spall experiment. Dynamic and static spall can be related through,

$$\sigma_{sp}(\text{dyn}) = \left(\frac{\dot{\varepsilon}}{\dot{\varepsilon}_t}\right)^{1/3}\sigma_{sp}(\text{stat}).$$ (4.11)

The theoretical surface energy of a crystalline solid is subject to some uncertainty. Based on the Orowan analysis, one estimate leads to [Lawn and Wilshaw, 1975],

$$\gamma_{th} = \frac{Eb_c}{\pi^2}.$$ (4.12)

Alternatively, Equation 4.4 relates surface energy directly to the theoretical strength of the material. Values from both relations are provided in Table 4.1 for the ceramics of concern, providing a measure of both the magnitude and the uncertainty in calculating the theoretical surface energy.

The spall data for the same materials are used, through the relation (Equation 4.7),

$$\gamma_{meas} = \frac{\sigma_{sp}^3}{6\rho^2 c^3 \dot{\varepsilon}},$$ (4.13)

to estimate the surface energy consistent with measured dynamic tensile failure. The strain rate consistent with the impact tests has some uncertainty. Here we have used the ampli-

30

tude and the duration (width at half maximum) of the spall pullback signal to calculate the strain rate. Values between 10^4/s to 10^5/s were determined depending on the material. The wave velocity $c = \sqrt{E/\rho}$ was used in Equation 4.13. The theory leading to Equation 4.13 does not specify this elastic property in detail.

Experimental values of γ_{meas} are provided in Table 4.1 and can be compared with estimated theoretical surface energies. For most of the materials the measured value is less than one order of magnitude higher than the theoretical value, consistent with their expected brittle nature. Tungsten carbide and zirconium dioxide are about two orders of magnitude higher; consistent with the additional deformation complexities of these two materials. The tungsten carbide was a liquid-phase sintered ceramic (see Section 8) and the zirconium dioxide was a transformation toughened material.

5 A Failure Criterion

A criterion for the onset of fracture within the shock process has been sought by various authors to describe the behavior of high-strength brittle solids. The familiar Tresca and von Mises criterion, under constraint of uniaxial strain loading, both reduce to,

$$\left| \sigma_x - \sigma_y \right| = T_o, \tag{5.1}$$

where the unconfined tensile failure stress T_o is a property of the material. While this criterion has been reasonably successful in describing the response of shock-loaded metals, it has not been adequate for ceramics. Other workers have attempted to develop more general pressure and rate dependent criteria to better describe dynamic failure in ceramics [Steinberg, 1991; Johnson and Holmquist, 1993; Curran et al., 1993]. Recently Rosenberg (1993) has suggested the applicability of the Griffith failure criterion for ceramics and has demonstrated the ability of this criterion to capture several of the unique shock effects in these brittle materials.

The criterion developed by Griffith (1924) is based on the stress concentrations at the tips of a population of microcracks assumed to pervade the material subjected to a stress load. The theory identifies a critical stress state at which favorably oriented cracks achieve a value characteristic of the material at which crack growth initiates. The analysis carried out by Griffith was strictly two dimensional and resulted in the criterion,

$$(\sigma_x - \sigma_y)^2 = 8T_o(\sigma_x + \sigma_y), \quad \text{if } \sigma_x + 3\sigma_y > 0, \tag{5.2}$$

$$\sigma_y = -T_o, \quad \text{otherwise.} \tag{5.3}$$

Compressive stresses are positive and Equation 5.2 and 5.3 apply when $\sigma_x > \sigma_y$. The material constant T_o is again the uniaxial tensile strength.

A rigorous three-dimensional extension of the Griffith criterion has not apparently been carried out. Rosenberg (1993) has proposed a direct application of the Griffith form (Equation 5.2) to the three dimensional uniaxial geometry ($\sigma_x \neq \sigma_y = \sigma_z$),

$$(\sigma_x - \sigma_y)^2 = 8T_o(\sigma_x + \sigma_y), \quad \text{if } \sigma_x + 3\sigma_y > 0, \tag{5.4}$$

Murrel (1963) has suggested a logical modification to three dimensions based on geometric symmetry considerations. When reduced to the uniaxial environment this criterion becomes,

$$(\sigma_x - \sigma_y)^2 = 12T_o(\sigma_x + 2\sigma_y), \quad \text{if } \sigma_x + 5\sigma_y > 0, \tag{5.5}$$

Although differences in absolute predictions between the two extensions of Griffith's criterion are noted, the important trends are similar. The unconfined compressive strength Y_o
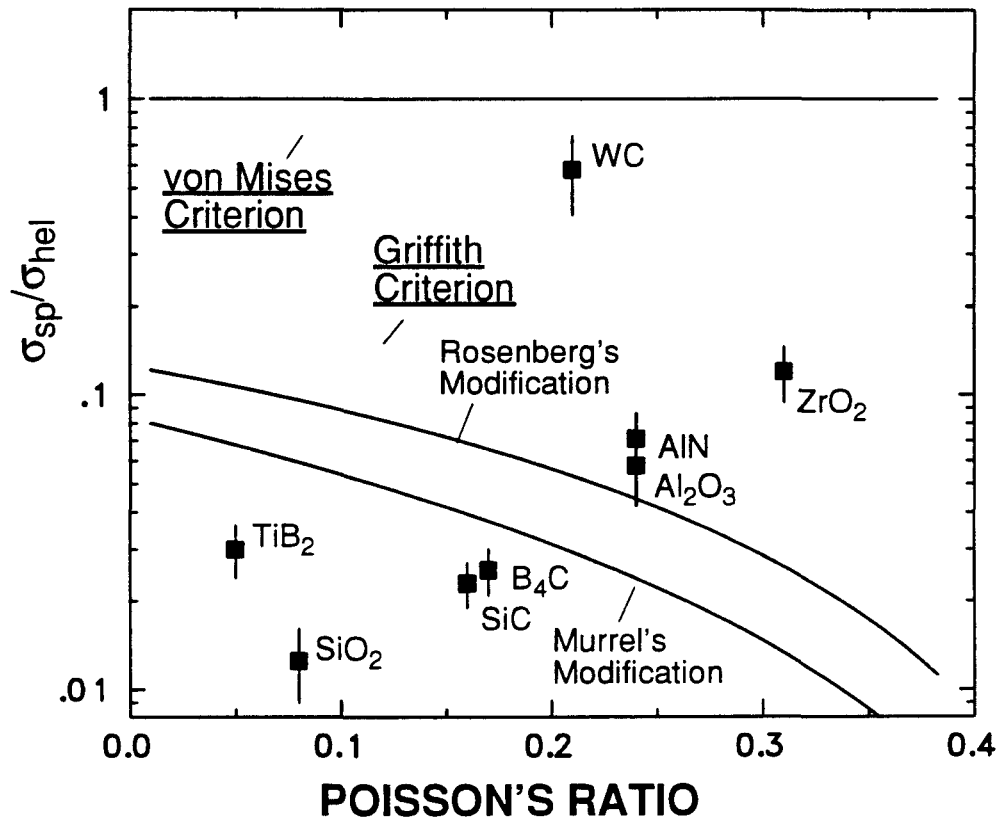
Figure 5.1 Comparison of the spall/HEL ratio for selected ceramics with predictions based on von Mises and Griffith failure criteria.

is significantly higher than the tensile strength — in agreement with observed behavior of ceramics. For Rosenberg's extension $Y_o = 8T_o$ while for Murrel's extension $Y_o = 12T_o$.

In the shock wave environment the spall strength is equal to the unconfined tensile strength, $\sigma_{sp} = T_o$, while the Hugoniot elastic limit σ_{hel}, or compressive strength under uniaxial strain loading conditions, can be related to the spall strength. Rosenberg's extension yields,

$$\sigma_{hel} = 8\frac{(1-v)}{(1-2v)^2}\sigma_{sp},$$ (5.6)

whereas Murrel's modification results in,

$$\sigma_{hel} = 12\frac{\left(1-v^2\right)}{(1-2v)^2}\sigma_{sp}.$$ (5.7)

In Figure 5.1 a plot of the ratio of the spall strength to the Hugoniot elastic limit for selected ceramics is provided from data in Table 4.1. Also shown are the predicted tensile failure levels based on von Mises and Griffith failure criteria. Relating the tensile yield based

33

on a von Mises criteria to the ductile spall strength is not strictly correct although plastic strains at yield appear to initiate cavity nucleation and growth [Curran *et al.*, 1987] and observed ductile spall strengths are usually comparable to or somewhat higher than the yield stress.

Although agreement in detail is not observed, the Griffith criteria for brittle failure is consistent in trend with low value of this ratio for most ceramics. Tungsten carbide has shown other indications of nonbrittle behavior, while the zirconium dioxide tested was a transformation toughened material, possibly accounting for the higher spall strengths and higher values in Figure 5.1. The low value for SiO_2, the one geological material included, is consistent with comparisons of the Griffith criterion with strength of other rock materials, [e.g., Janach (1977)].

Like the Griffith criterion, the dynamic relation for spall in brittle materials (Equation 4.7) also follows from thermodynamic energy principles. Consequently, it is reasonable to explore the Griffith failure criterion within the dynamic regime of behavior through inclusion of the early spall relation. Working with Murrell's modification (Equation 5.5) a prediction for the Hugoniot elastic limit based on fundamental material properties is

$$\sigma_{hel} = 12\frac{\left(1-v^2\right)}{(1-2v)^2}\left(6\rho^2 c^3 \gamma \dot{\varepsilon}\right)^{1/3}. \tag{5.8}$$

Using reasonable properties for aluminum oxide ($v = 0.23$, $\rho = 4000$ kg/m^3, $c = 10^4$ m/s, $\gamma = 5$ J/m^2) and assuming an effective strain rate range of 10^5/s-10^6/s, yields a Hugoniot elastic limit of about $\sigma_{hel} \approx 14$-30 GPa which can be compared with values of 6-12 GPa for reasonably competent alumina ceramics.

Equation 5.8 is not intended as an accurate predictor of the shock strength properties of brittle materials. It should be regarded as a first-order expression for the dynamic compressive failure of an ideal flawed brittle material in the sense of Griffith. Numerous microstructural issues known to influence dynamic strength (i.e., grain structure, porosity) are not accounted for. Nonetheless, the reasonable agreement with measured strengths of ceramics would lend support for the brittle failure mechanics leading to Equation 5.8 and provides additional argument for a fracture-dominated process controlling failure in the compressive shock loading environment.

Equation 5.8 also predicts a strong cube root strain rate dependence of the Hugoniot elastic limit. As will be discussed in Section 10, examination of elastic precursor decay in ceramics does not support this aspect of Equation 5.8, and weakens the argument for a brittle mechanism in the shock wave front.

34

6 Shock-Wave Strength Properties of Boron Carbide and Silicon Carbide

Time-resolved velocity interferometry measurements have been made on boron carbide and silicon carbide ceramics to assess the dynamic equation-of-state and strength properties of these materials. Hugoniot precursor characteristics, and post-yield shock and release wave properties, indicated markedly different dynamic strength and flow behavior for the two carbides.

Thus, in this study, shock and release wave profiles in boron carbide and silicon carbide have been measured from peak stress states that are just in excess of the Hugoniot elastic limit to peak stresses approaching 60 GPa. Silicon carbide reveals an uncommonly high Hugoniot elastic limit (~15-16 GPa) compared to many materials. Post-yield strength of silicon carbide, determined by comparison of Hugoniot uniaxial strain and calculated hydrodynamic response, reveals neutral or increasing strength with subsequent deformation beyond the initial dynamic yield. Boron carbide exhibits a somewhat higher Hugoniot elastic limit (~18-20 GPa). In contrast, however, subsequent deformation indicates a dramatic loss in strength supporting capability. Hugoniot and hydrodynamic response for boron carbide converge at stresses approaching about twice the Hugoniot elastic limit, suggesting little or no shear stress component at higher Hugoniot states. The contrasting dynamic strength characteristics of silicon carbide and boron carbide are further amplified in the release properties of these materials from the Hugoniot state. The release paths for silicon carbide indicate reverse yielding and continued strength characteristics of elastic-plastic material behavior. The unloading stress-volume paths for boron carbide closely parallel the calculated hydrodynamic behavior suggesting near fluid-like response with sustained loss of strength. Further features in the measured wave profiles indicate heterogeneous deformation in boron carbide in contrast to homogeneous deformation in silicon carbide. Microscopic mechanisms which may be responsible for the strikingly different shock and deformation properties of these two ceramics are considered.

6.1 Materials and the Shock-Wave Experiment

The silicon carbide tested in the present study was supplied by Eagle Picher Industries. The density of this material is 3177 kg/m^3. The longitudinal and shear elastic velocities are 12.02 and 7.67 km/s, respectively. The material has a porosity of approximately 1% and a nominal grain size of 7 μm. Knoop hardness for this ceramic is 22.3 [Grady, 1994]. Shock wave data for this material have previously been reported [Kipp and Grady, 1989; Grady and Kipp, 1993]. The boron carbide investigated in the current work was provided by Dow Chemical Company. The density is 2506 kg/m^3. Longitudinal and shear elastic velocities are 14.03 and 9.65 km/s, respectively. The nominal grain size is 3 μm, porosity of the order of 1%, and Knoop hardness is 25.6. Properties and microstructure differ slightly from another boron carbide provided by Eagle Picher Industries for which shock-wave data have previously been reported [Kipp and Grady, 1989].

Planar shock and release wave experiments were performed on the monolithic ceramic samples with a single stage powder gun capable of 2.5 km/s maximum projectile velocity.
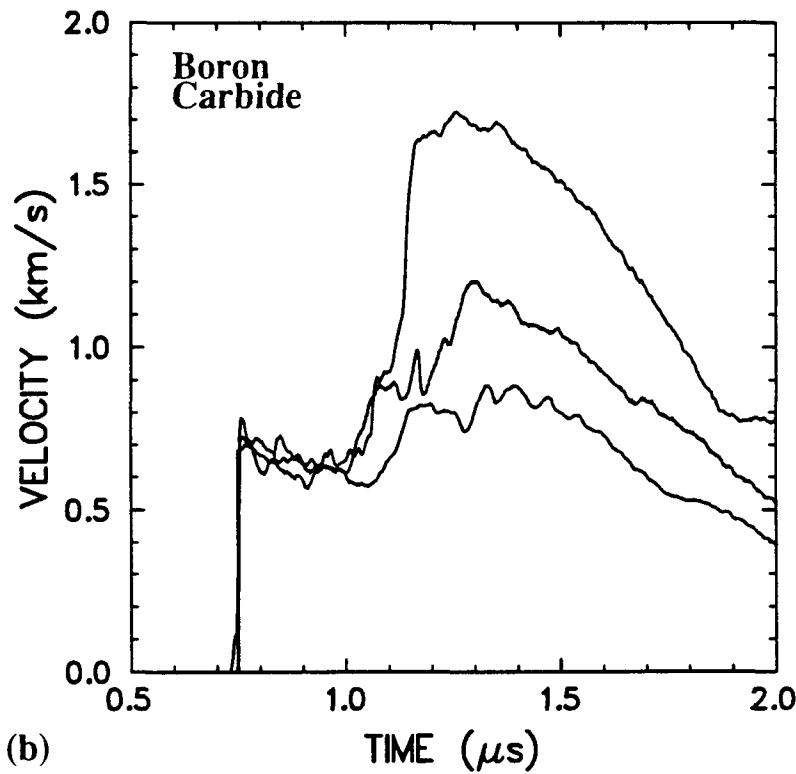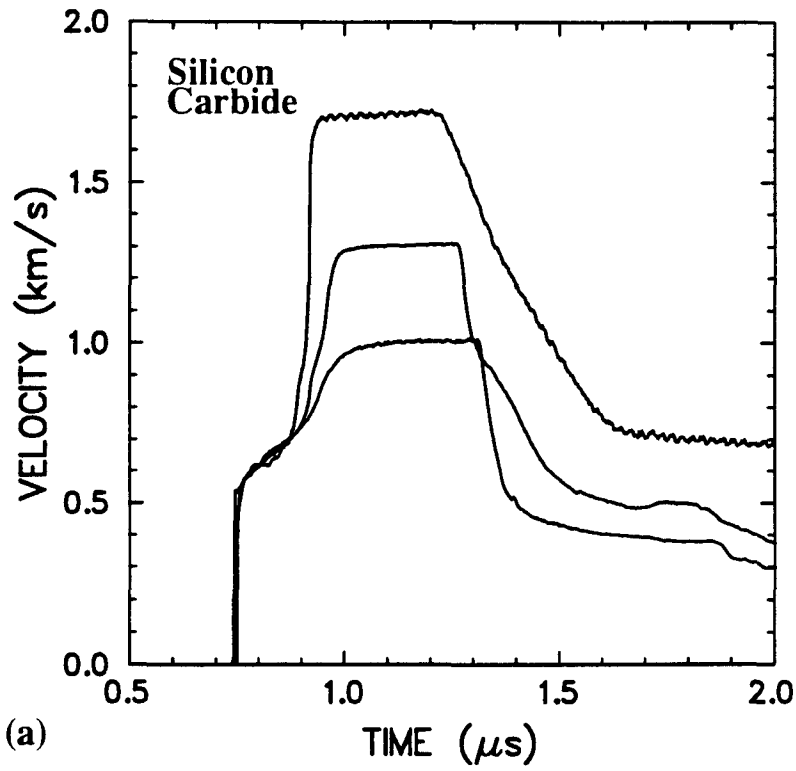
Figure 6.1   Shock and release wave profiles for silicon carbide and boron carbide
ceramics measured with velocity interferometry diagnostics.

Plates of the same ceramic, or a high density metal, were backed by low density polyurethane foam, mounted on the projectile, and caused to impact stationary target plates of the test ceramic. Target samples were backed by lithium fluoride windows approximately 25 mm in thickness and 50 mm in diameter. The transmitted particle velocity profiles produced by the impact-generated shock waves were measured with laser velocity interferometry (VISAR) techniques [Barker and Hollenbach, 1972]. Details of the experimental method have been reported earlier [Grady, 1992a; Grady, 1992b]. Measured shock and release wave profiles for silicon carbide and boron carbide are provided in Figure 6.1. Experimental dimensions are noted in Table 6.1. In all tests the peak stress (ranging between about 25 and 50 GPa) exceeded the Hugoniot elastic limit of the ceramic. Striking differences in wave profile characteristics relating to the elastic precursor wave, the Hugoniot state, and the release structure are noted between the two ceramics. These differences are discussed further in the subsequent subsections.

Table 6.1:
Experimental Conditions for Impact Tests.

Test Number	Foam[a] Density (kg/m^3)	Projectile Material	Projectile Thickness (mm)	Target Material	Target Thickness (mm)	Impact Velocity (km/s)
CE-4	320	SiC	3.987	SiC	8.939	1.542
CE-5	640	SiC	3.995	SiC	8.940	2.100
CE-31	640	Tantalum	1.516	SiC	8.956	2.118
CE-17	320	B_4C	4.831	B_4C	10.322	1.633
CE-18	640	B_4C	4.815	B_4C	10.346	2.076
CE-26	640	Tantalum	1.514	B_4C	9.680	2.059

[a] Polyurethane foam discs backing the projectile impact plate were approximately 6 mm in thickness.

6.2 Elastic Precursor Characteristics

Details of the elastic precursor waves for silicon carbide and boron carbide are shown in Figure 6.2. The Hugoniot elastic limit is defined here as the break in slope following the steep rise of the initial wave arrival — a profile velocity of about 0.55 km/s for silicon carbide and about 0.7-0.8 km/s for boron carbide. Stress values for the Hugoniot elastic limit calculated by impedance matching methods are about 15-16 GPa for silicon carbide and 18-20 GPa for boron carbide. Post-yield characteristics of the precursor waves are dramatically different for the two materials, however. For silicon carbide the positive slope of the precursor wave reveals a subsequent hardening with further deformation to stresses in excess of 20 GPa. Whether pressure hardening or deformation hardening plays the more dominant role cannot be uniquely determined from the shock wave data. Nevertheless,
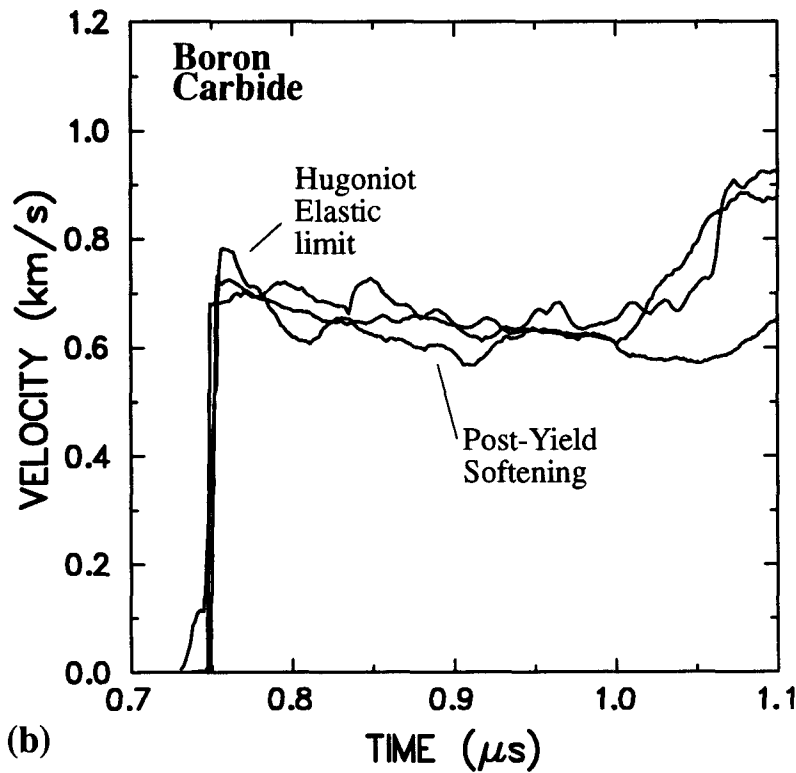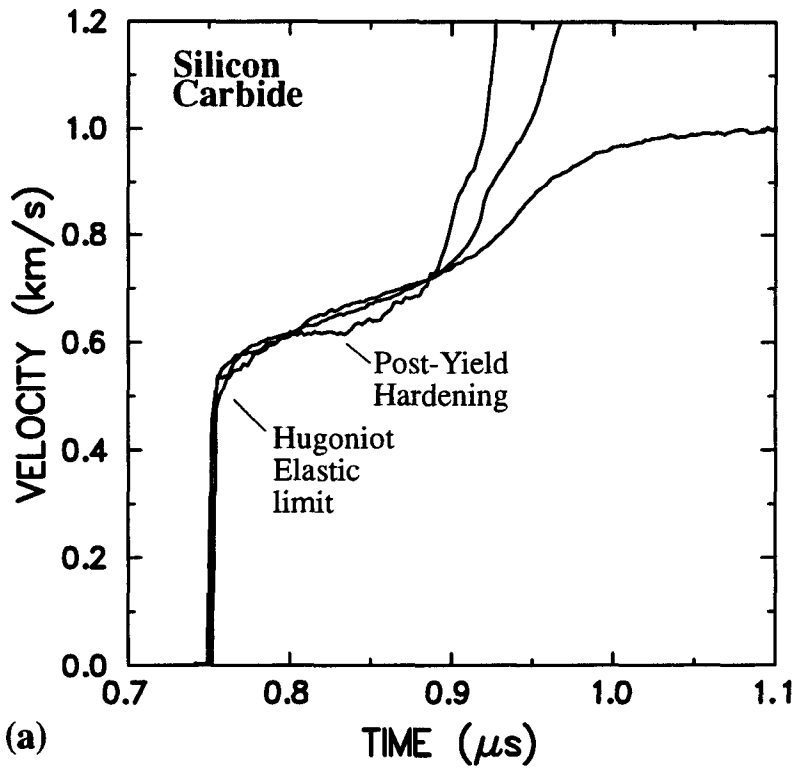
Figure 6.2   Details of the elastic precursor wave profiles measured with VISAR
diagnostics for silicon carbide and boron carbide.

38

significant resistance to dislocation plasticity or compressive shear fracture continues to persist in silicon carbide as dynamic shear deformation in the shock process proceeds.

Precursor waves for boron carbide, in contrast, indicate post-yield stress softening. Stress relaxation suggests a rate-sensitive deformation process, probably accompanied by precursor attenuation with propagation distance. The latter behavior has been confirmed by shock profile measurements on thinner samples (see Section 10).

Finally, it is worth noting in Figure 6.2 the nearly a factor of two difference in time separation of the elastic wave and first indication of the following deformation shock wave between silicon carbide and boron carbide. This feature also reveals distinct differences in post-yield strength characteristics of the two ceramics.

6.3 Hugoniot Properties

Hugoniot states achieved in the shock process are assessed by estimates of the elastic and deformation shock velocity from the profile data, and particle velocities from either the symmetry of the impact, the known Hugoniot curve of the impactor material, or the measured amplitudes from the wave profiles. The velocity of the elastic precursor was not measured in the present study. Instead the longitudinal elastic velocity was augmented by an estimate of the non-linearity of the material at the Hugoniot elastic limit $U_{hel} = C_l + Su_{hel}$, assuming a representative value of $S = 1$, to provide the elastic shock velocity U_{hel}. This estimated elastic shock velocity is about 4 to 5 percent larger than the elastic wave speed C_l. The deformation shock velocity is then referenced to the elastic shock wave velocity.

Shock velocity versus particle velocity data for silicon carbide and boron carbide are shown in Figure 6.3. Both Hugoniot elastic limit and final Hugoniot states are identified. The dashed curve represents the bulk sound velocity, $C_o^2 = C_l^2 - 4C_s^2/3$, determined from ultrasonic data of Manghnani (1994) to 2 GPa and extrapolated to higher pressure using the reported values for the zero pressure bulk moduli K_o and the pressure derivative K_o'. Hugoniot states for silicon carbide are in good agreement with the extrapolated bulk velocity and consistent with a material which retains a shear strength at the Hugoniot pressure comparable to the strength at the Hugoniot elastic limit. In contrast, shock velocities for boron carbide are markedly lower than bulk velocities suggesting significant reduction in the shear strength at the Hugoniot state. Open circles for boron carbide represent the new data (Figure 6.1 and Table 6.1). Closed circles correspond to an earlier material which exhibited a slightly reduced Hugoniot elastic limit and somewhat higher deformation shock velocities [Kipp and Grady, 1989].

Hugoniot states are plotted in stress versus specific volume space in Figure 6.4. In addition to the data from Figure 6.3, Hugoniot states for one experiment each for silicon carbide and boron carbide below the Hugoniot elastic limit reported previously [Kipp and Grady, 1992] are shown. Also a recently measured Hugoniot point to nearly 58 GPa, using a two-stage light gas gun on a 3-mm thickness boron carbide sample, is included. Also shown in Figure 6.4 are estimates of the bulk pressure versus volume response of both ceramics, again based on the ultrasonic data of Manghnani (1994). A serious uncertainty in
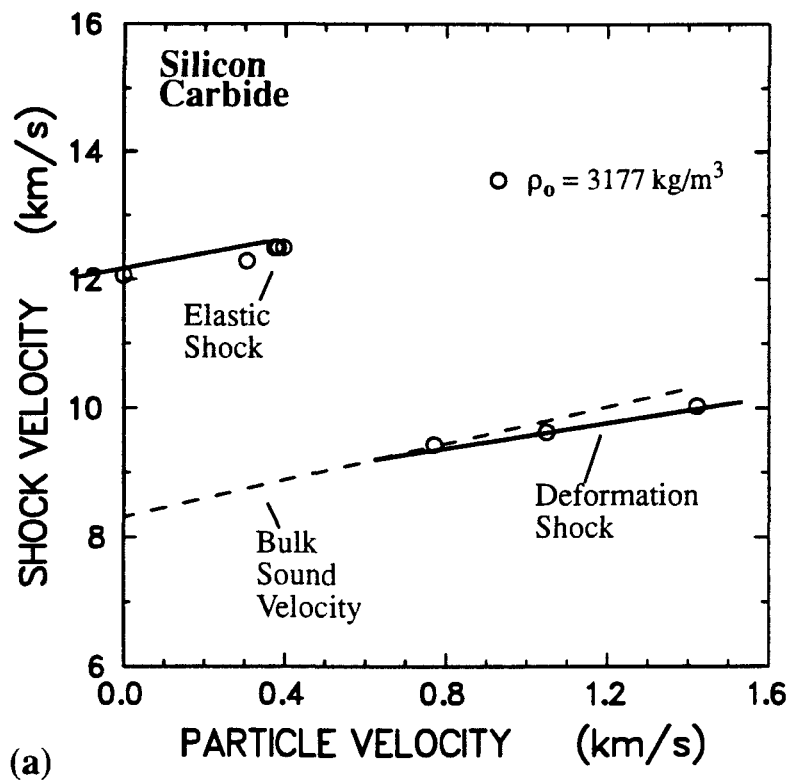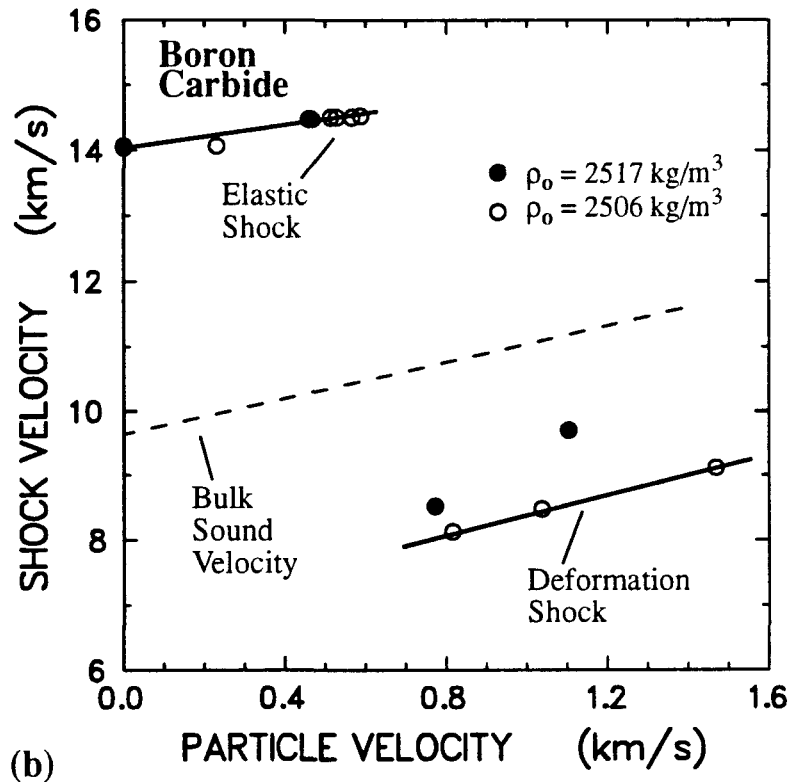
Figure 6.3   Hugoniot shock velocity versus particle velocity data for silicon carbide and boron carbide.

this construction arises from an unclear knowledge of the theoretical density of the ceramic materials. Ideally the theoretical density appropriate to this development should represent the zero porosity material accounting for any sintering impurities or differences in chemistry from the common formula unit. The reference densities used in Figure 6.4 simply account for the nominal 1% porosities of these ceramics and may be uncertain by as much as a percent either way.

Comparisons of the Hugoniot data in Figure 6.4 with the estimated bulk response generally support observations relating to shock velocity data in Figure 6.3. For silicon carbide the measured Hugoniot states are offset substantially from the pressure-volume curve indicating retention of a substantial shear stress component. Boron carbide, on the other hand, upon exceeding the Hugoniot elastic limit, exhibits a dramatic increase in compressibility and achieves final Hugoniot states near the bulk pressure-volume curve. Post-yield behavior for boron carbide would suggest nearly complete loss of shear strength. The fact that the 40 and 58 GPa Hugoniot points actually lie to the left of the estimated pressure-volume curve is of some concern. It may simply reflect the uncertainty in the initial theoretical density of this ceramic. It should be remembered, however, that the unique deformation processes initiated during shock compression could potentially lead to enhanced volumetric lattice compression (with corresponding change in lattice structure) which exceeds the calculated stable lattice compression based on the lower pressure ultrasonic data. Considering the unusual, very open structure of the boron-carbide lattice [Emin, 1987], an anomalous volume compression under shock loading should not be ruled out.

Finally, complete shock and release wave profiles from several of the tests have been matched with one-dimensional wave code calculations by Kipp [Kipp and Grady, 1989; Grady and Kipp, 1993] using adjustable parameter computational models. The three dashed curves for silicon carbide and two for boron carbide in Figure 6.4 represent the stress-volume load and release curves corresponding to a satisfactory fit to these wave profiles. The nature of the curves for silicon carbide corresponds remarkably well to a high-strength elastic-plastic material. Simulations of the boron carbide wave profiles, on the other hand, suggest loss of strength above the Hugoniot elastic limit and near-fluid-like behavior on stress release.

6.4 Discussion

Markedly different dynamic compression and release behavior are noted in the shock compression characteristics of silicon-carbide and boron-carbide ceramics. The common methods of contrasting shock compression states with measured or estimated hydrostatic pressure-volume behavior suggests near-metal-like shock properties for silicon carbide in its strength-retention characteristics under a cycle of shock-wave compression and release. A similar comparison for boron carbide, however, indicates catastrophic loss of strength above the Hugoniot elastic limit with near-fluid behavior during subsequent deformation in the shock load and release cycle. Such comparisons can be misleading, however, and other interpretations of the data are possible. The possibility of a phase-change-like volume collapse in boron carbide under shock compression should not be ruled out.

41
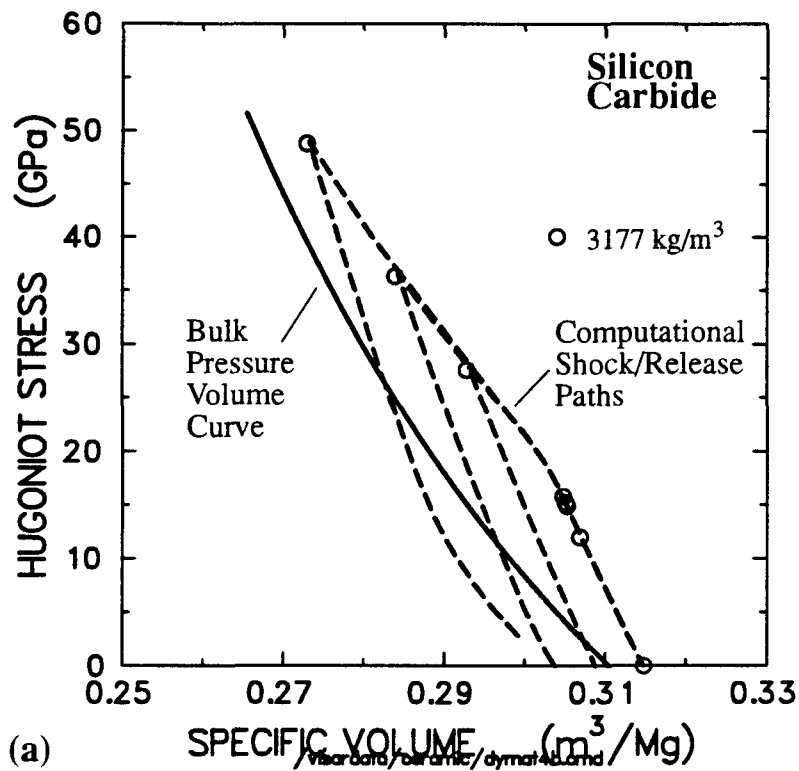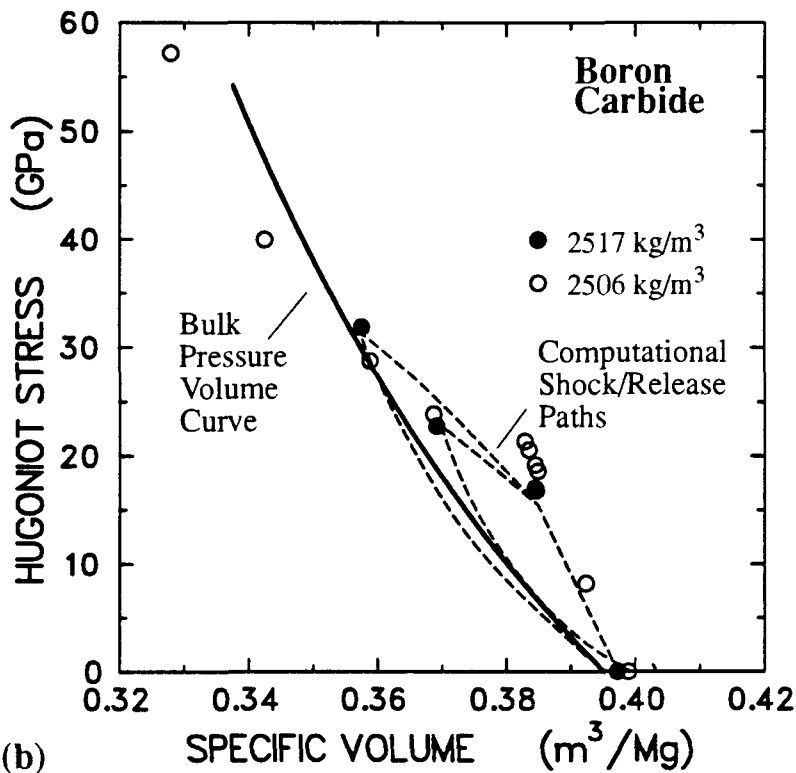
Figure 6.4   Data points are elastic and final shock Hugoniot states. The solid curve is the bulk pressure versus volume behavior from extrapolation of ultrasonic data. Dashed curves correspond to wavecode solutions to experimental VISAR profiles.

Another intriguing feature in the velocity interferometry data of Figure 6.1 should be noted. Profiles for silicon carbide are smooth and regular whereas corresponding profiles for boron carbide show an erratic and irregular component to the measured motion. The VISAR laser beam is focused to a spot of about 25-50 μm in diameter in these experiments. Consequently the measured motion represents an average over this spot size. Other workers [Atroshenko *et al.*, 1990; Meshcheryakov *et al.*, 1991] have discussed the effect on VISAR data of differential interface motion at various spatial scales. Differential motion on a scale less than the spot size will lead to reduction in VISAR contrast because interference maxima and minima at different points within the spot will be achieved at different times. Differential motion on a scale larger than spot size will not appreciably affect contrast. Random elastic wavelets from nearby points removed from the laser spot and undergoing differential motion can, however, lead to irregular motions at the recording point. VISAR data on both the subscale (less than spot size) and mesoscale (greater than spot size) for silicon carbide indicate homogeneous motion under shock loading. VISAR data for boron carbide, however, suggests homogeneous motion on the subscale, but heterogeneous motion on the mesoscale. The latter result may suggest a heterogeneous deformation process under shock loading within the 50-500 μm spatial scale. The concentration of deformation energy into discrete deformation zones along with localized material softening or melting has been proposed as a mechanism for reduced-strength fluid-like behavior in brittle solids under shock wave load and release [Grady, 1980].

7 Shock Phase Transformation and Release Properties of Aluminum Nitride

Aluminum nitride is characterized by a non-recoverable volume phase transformation from the wurtzite (hexagonal) to the rocksalt (cubic) structure that commences under shock compression at about 22 GPa. The phase transformation has been reported by Vollstädt, et al. (1990) in static high pressure experiments, and by Kondo, et al. (1982) in shock wave experiments. In the latter study, the discrete data, obtained with pin and electromagnetic gage techniques, clearly indicated the presence of the phase transformation. The current study expands on that uniaxial data with time-resolved measurement of particle velocity histories of the shock and release states. Four experiments are reported, all with peak impact pressures of approximately 40 GPa, well above the phase transformation pressure. The evolution of the shock wave with propagation distance is addressed with variations of the target layer thickness. Details of the material response are obtained by numerical analysis techniques developed to examine the response of several other ceramics to shock loading [Kipp and Grady, 1990]. The data obtained in the present study provide a basis for development of accurate computational models that can represent the response of this ceramic to high strain-rate loading in shock wave propagation codes. Such models can then be used to examine the consequences of the large energy-absorbing aspect of the volumetric phase transformation of this ceramic during shock loading events. Useful data for aluminum nitride have also been provided in the longitudinal and lateral shock wave measurements of Brar, et al. (1992), and shock compression studies of phase transformations by Nakamura and Mashimo (1994). Elastic properties and their pressure and temperature dependence have been investigated by Gerlich, et al. (1986), while Van Camp, et al. (1991) have explained equation of state issues in aluminum nitride as well as other binary nitrides. Shock and equation-of-state properties of aluminum nitride have recently been reviewed by Dandekar et al., (1994).

7.1 Materials and Experiment

The aluminum nitride used in this study was produced by DOW Chemical Corporation. The nominal reference density of the aluminum nitride was 3262 kg/m^3. Ultrasonic measurements on samples of this material indicate a longitudinal velocity of 10730 m/s and a shear velocity of 6320 m/s. Associated elastic properties derived from these velocities are a Poisson's ratio of $v = 0.234$, and bulk sound speed of 7866 m/s. The hot-pressed ceramic had a nominal porosity of 1% and a grain size of approximately 2 μm.

Pure tantalum and tungsten impactors were used in order to obtain initial shock amplitudes well above the phase transition point of the aluminum nitride at the impact velocities attainable with the impact facility employed. The lithium fluoride used as the laser window material in the present impact experiments was optically clear [100] oriented single crystals [Wise and Chhabildas, 1985].

Uniaxial-strain compressive shock and release waves were produced in the aluminum nitride with a single-stage powder-gun facility as discussed in Section 2. The impactors were either tantalum backed by polyurethane foam or tungsten backed by polymethyl

methacrylate (PMMA) and were accelerated with the powder gun to velocities of about 2200 m/s, providing shock amplitudes between 37 and 41 GPa in aluminum nitride. The thicknesses of the tungsten and tantalum impactor plates were about 1.5 mm. The plate impactor thicknesses in these experiments were designed so that the complete shock and release profile could be measured at the recording interface.

The suite of target ceramic thicknesses led to variations in available time for both the development of the shock wave structure and the subsequent interaction of the release wave with the propagated shock wave. Table 7.1 lists the key parameters associated with these experiments.

Table 7.1:
Uniaxial Strain Impact Experiments on Aluminum Nitride

Test No.	Density (kg/m³)	Thickness (mm)	Impactor Materials	Impactor Velocity (m/s)	Impactor Thickness (mm)	Hugoniot Stress (GPa)
CE 44	3265	2.507	PMMA / Tungsten	2281	1.502	41
CE 43	3262	2.510	Foam / Tantalum	2207	1.528	37
CE 52	3258	4.183	Foam / Tantalum	2215	1.526	37
CE 37	3265	9.567	Foam / Tantalum	2239	1.508	38

The measured particle velocity profiles of all four experiments are shown in Figure 7.1. The arrival times of the initial, or "elastic", waves correspond to the ultrasonic longitudinal transit time through the aluminum nitride targets. The two highest amplitude wave profiles (both with arrival time at 0.2 μs) are for the tungsten (CE 44) and tantalum (CE 43) projectiles impacting 2.5 mm of aluminum nitride. The impactor thicknesses, impactor velocities, and aluminum nitride target thicknesses are of comparable magnitude for both these experiments (Table 7.1). The higher impedance of the tungsten, and its slightly larger impact velocity results in a larger amplitude particle velocity than for the corresponding tantalum case. This in turn leads to a much earlier arrival of the upper shock wave characterizing the shock-induced phase transformation. The initial break in the shock wave occurs at about 400 m/s, and represents onset of permanent deformation, or "yield", as typically observed in many ceramics tested in this one-dimensional strain configuration [Kipp and Grady, 1990; Grady, 1992]. The second break which appears, at about 900 m/s, is believed to correspond to onset of the wurtzite (hexagonal) to the rocksalt (cubic) phase transformation, with a non-recoverable volumetric phase transformation. The release wave structure substantiates the non-recoverable aspect of this transition, as will be demonstrated by evaluation of the one-dimensional numerical calculations of the experimental wave profiles.

In three experiments, the thickness of the tantalum flyer plate was maintained at approximately 1.5 mm, and the impact velocity was fixed at about 2200 m/s (Table 7.1). Although for the 2.5 mm aluminum nitride target a wave with some time at the peak between
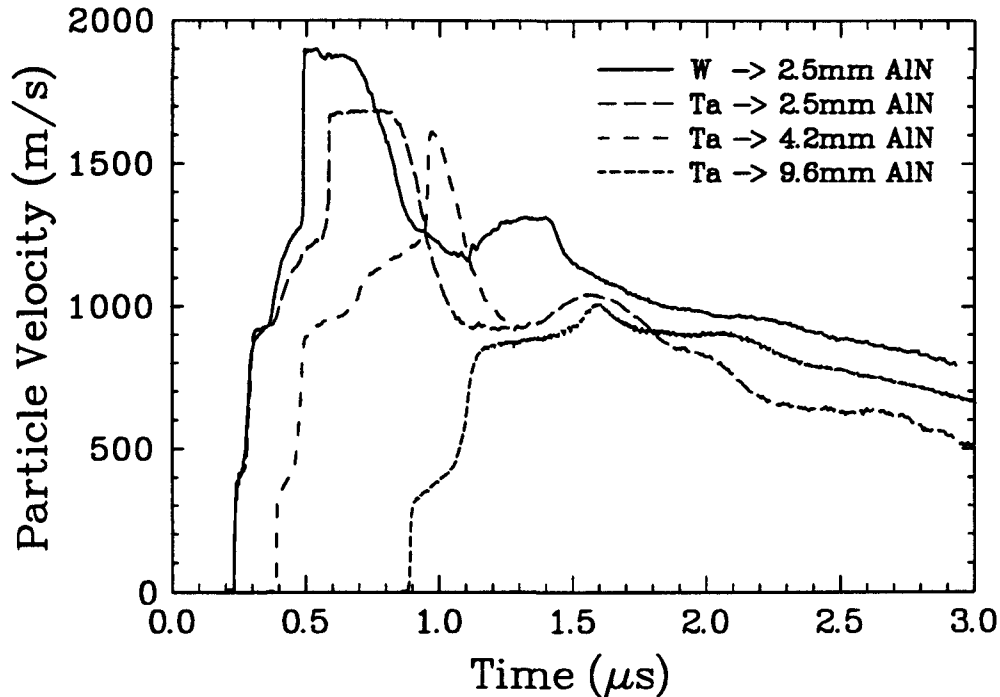
Figure 7.1   Particle velocity records for tungsten impactor (1.5 mm, 2200 m/s) impacting 2.5 mm aluminum nitride target, and tantalum impactor (1.5 mm, 2200 m/s) impacting 2.5 mm, 4.2 mm, and 9.6 mm aluminum nitride targets.

shock and release is recorded, increasing the thickness of the aluminum nitride target effectively extends the propagation distance of both the release wave, which emanates from the trailing low impedance interface of the flyer, and the initial shock wave. Given sufficient propagation distance, the release wave will overtake the lower velocity phase transformation wave, and the interaction will attenuate the amplitude of the initial wave. The third profile in Figure 7.1 (4.2 mm aluminum nitride) shows the upper part of the shock wave just beginning to be eroded by the release wave at the recording interface. The 9.6 mm aluminum nitride target is of large enough thickness that almost complete attenuation of the upper shock wave has occurred by the time the rear surface of the ceramic target has been encountered.

There are two other noticeable trends in the particle velocity records for the tantalum impactor series in which the thickness of the aluminum nitride target increases from 2.5 mm to 9.6 mm: (1) the initial amplitude of the break in the first shock wave decays from about 400 m/s to 320 m/s, and (2) the amplitude of the second break, identified with the phase transformation, drops in amplitude from 900 m/s to 840 m/s.

## 7.2 Compression and Release Properties

The complex structure of the particle velocity history, particularly above the phase transformation point in both the shock and release waves, is a consequence of impedance dif-

ferences at the impact and recording interfaces of the target. The tantalum and tungsten impactors have significantly larger impedances than the aluminum nitride targets, and the impedance of the lithium fluoride window is less than one-half that of aluminum nitride. As a consequence, when the release wave from the trailing interface of the impactor arrives at the impact interface, some unloading will occur. In the same way, at the aluminum nitride / lithium fluoride window interface, the reflected partial release wave will interact with the higher amplitude, slower shock of the phase transformation. The numerical techniques used here account for all these wave interactions, and clarify the original wave structure in the aluminum nitride targets.

Analysis of the data was made with a one-dimensional Lagrangian finite-difference wave propagation code, WONDY [Kipp and Lawrence, 1982]. The aluminum nitride material response was characterized with parameterized sound velocity and strain linear segments, with separate loading and unloading curves defined so that both shock and release properties of the ceramic could be represented [Kipp and Grady, 1990]. Linear variations in sound speed with strain result in a quadratic dependence of the local material modulus on strain. Particular care was required to monitor the current amplitude and rate of loading so that the correct unloading and reloading curves were used for the local material response. The local material modulus was calculated from the sound speed based on the local strain and the appropriate sound speed segment, and determined the increment in axial stress at each time step in the calculation. Ultrasonic data were used to determine the initial loading moduli. The parameters of the sound speed curves for the inelastic response were determined iteratively, tailored to match the particle velocity history for each experiment. By taking account of the interactions of the waves at the lithium fluoride / aluminum nitride and flyer / aluminum nitride interfaces, this approach provided the capability to examine the ceramic response interior to the samples, and in particular, to determine the effect of the volume phase transformation on the transmitted wave structure.

The tantalum and tungsten impactors were modeled with an anisotropic strain hardening model in WONDY [Kipp and Lawrence, 1982]. Shock and release data for each of these materials in this regime of pressure verified the parameters used to characterize these materials. Data for the tungsten were obtained from Chhabildas, et al. (1988) and for the tantalum from Chhabildas and Asay (1992). The release wave that originates at the trailing interface of the impactor is transmitted to the target through the impact interface. It is of particular importance that the initial structure of this transmitted release into the aluminum nitride sample be as accurate as possible. Otherwise, modeling errors in the impactors will corrupt the analysis of the particle velocity data by requiring compensating errors in the model constructed for the aluminum nitride.

Numerical analysis of the experiment in which a 2.5 mm target was impacted with a 1.5 mm tantalum projectile (Experiment CE 43) resulted in the fit to the particle velocity data shown in Figure 7.2(a). Nearly all of the features of the data are captured by this analysis technique; iterations on the sound speed - strain function focused primarily on the first microsecond of the record in order to reproduce the shock and release response of the aluminum nitride in as much detail as possible. The fit to the particle velocity data in which a 2.5 mm aluminum nitride target was impacted by 1.5 mm tungsten projectile (Ex-
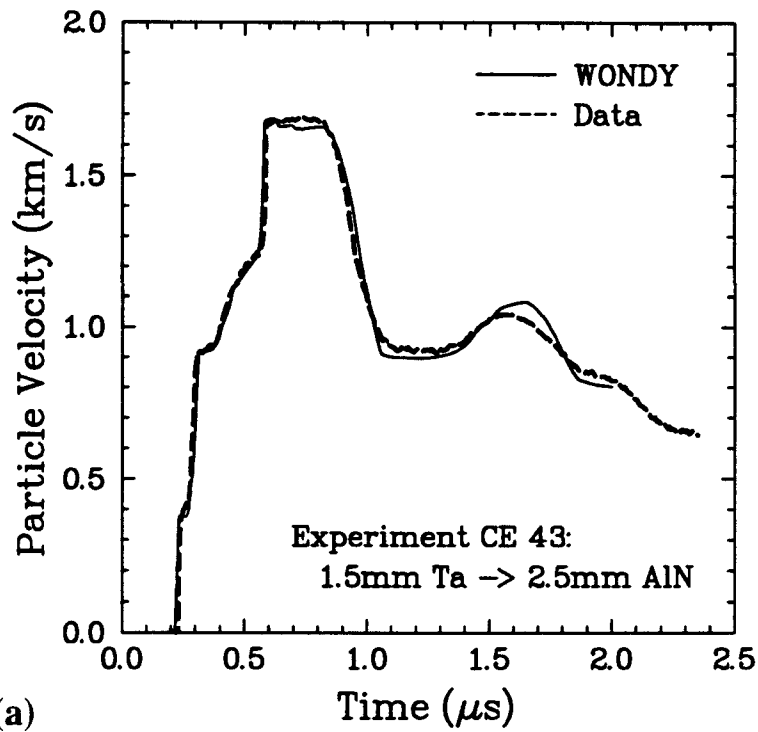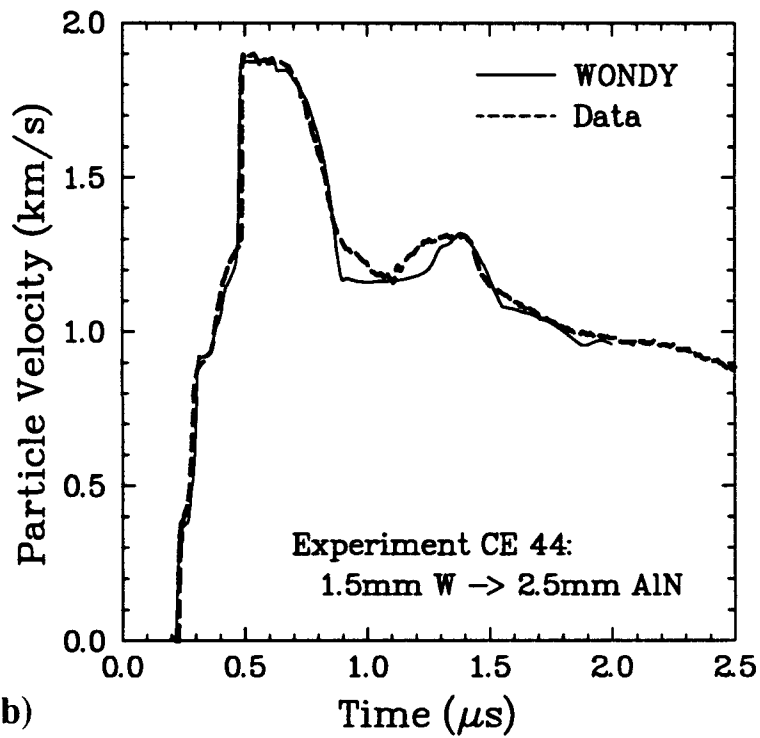
Figure 7.2   (a) Numerical fit to interface particle velocity data for tantalum
impact on 2.5 mm aluminum nitride (CE 43). (b) Numerical fit to
interface particle velocity data for tungsten impact on 2.5 mm
aluminum nitride (CE 44).

48

periment CE 44) is shown in Figure 7.2(b). The sound speed - strain functions used to fit these two experimental profiles differ only slightly at large strains, in order to accommodate the increased velocity of the upper shock at the higher impact pressure. The unloading curves are identical for these two cases.

The appearance of a transmitted stress wave in an aluminum nitride target is recorded in Figure 7.3(a). The three-wave structure is much more well-defined in this representation than in the particle velocity history at the target / window interface, because no interface wave interactions have occurred yet. The structure in the particle velocity data in both Figure 7.2(a) and Figure 7.2(b), beginning at 0.35 μs and ending at about 0.5 μs in the particle velocity interval 900 m/s to 1250 m/s, is all due to wave interactions at the target / window interface, and is not present in the transmitted wave prior to encountering the interface. The three primary waves are identified in Figure 7.3(a) as the initial elastic wave, the deformation (or "plastic) wave, and the phase transformation wave.

The stress - strain response that corresponds to this transmitted wave profile is shown in Figure 7.3(b). The first (elastic) wave has an amplitude of approximately 10 GPa, Figure 7.3(a) and Figure 7.3(b), at which point a break in the curve indicates the onset of yield. This amplitude agrees well with 9-10 GPa reported by Nakamura and Mashimo (1994), and 9.4 GPa reported by Brar, et al. (1992). The next break in the wave occurs at 22 GPa, which compares well with 21±1 GPa shock transition pressure reported by Kondo, et al. (1982), and 19 GPa reported by Nakamura and Mashimo (1994). The total axial strain at the beginning of the phase transformation is about 7.5%. The maximum amplitude of the shock wave in this case corresponds to about 28% strain, with the phase transformation accounting for about 20% strain between the onset and the maximum load. This volumetric compression agrees well with the value of 22% obtained by Kondo, et al. (1982) from shock wave experiments. These results also compare favorably with static measurements, in which a transition pressure of 16.5 GPa and volume strain of 21% were reported by Vollstädt, et al. (1990).

Note that as the aluminum nitride unloads from peak compression of about 40 GPa down to about 10 GPa, the unloading progresses nearly elastically, recovering about 6% strain, and does not follow the initial compression curve that included the phase transformation in Figure 7.3(a). This indicates that no reversal of the phase transformation on unloading to approximately 10 GPa has occurred in the elapsed time of this experimental configuration, and that the deformation (volume strain) accompanying the phase transformation is permanent. Were there a reversal of the phase transformation during unloading, a much more complex representation of the unloading curve would be required.

The functional relationship of sound speed to strain determined for the aluminum nitride that engenders the accurate fit to the particle velocity data in Figure 7.2(a) is shown in Figure 7.4(a). The discrete nature of the sound speed fitting segments and the distinct loading and unloading curves are quite evident in this figure. The reference zero-strain velocity is the ultrasonic velocity, followed by a slight increase (non-linear elastic) to the yield point at about 2% strain. A sudden drop in sound speed to 8300 m/s occurs to represent the "plastic" deformation wave. At the onset of the phase transformation, there is a another large decrease in sound speed to accommodate the volumetric compression of the
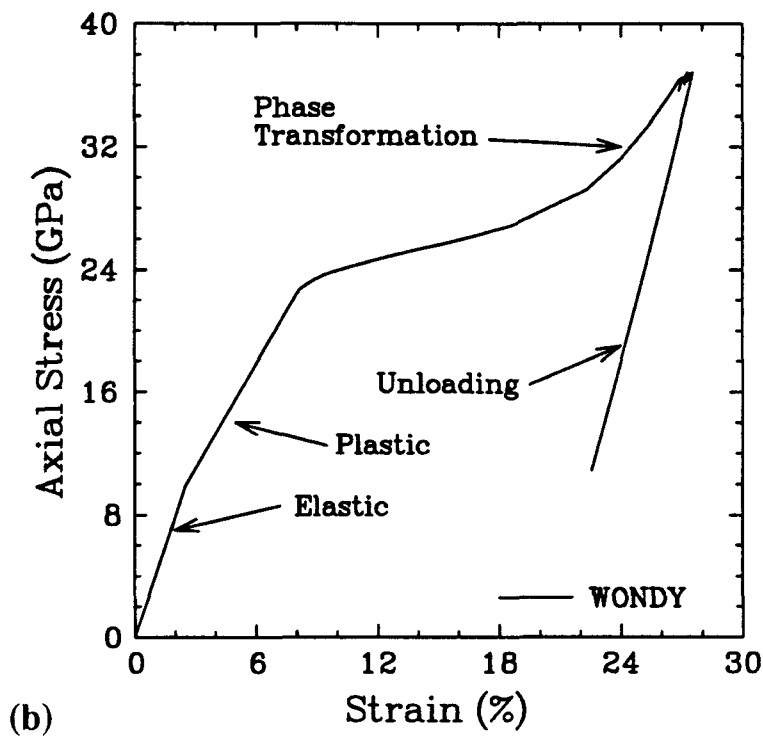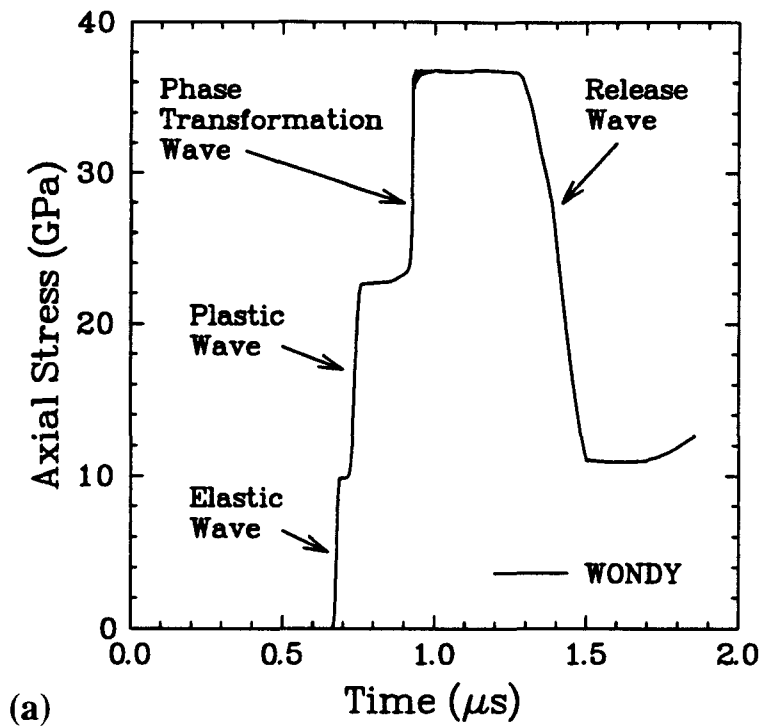
(a)

(b)

Figure 7.3   (a) Transmitted wave profile in aluminum nitride from tantalum
impact. (b) Stress-strain response of aluminum nitride.

50

phase transformation as shown in Figure 7.4(a). The sound speed then gradually recovers with increasing strain as the phase transformation deformation limit is approached. The sound speed function between "onset" and "completion" determines the structure in the particle velocity histories at the recording interface above the "plastic" wave (0.35 - 0.5 µs, Figure 7.2(a) and Figure 7.2(b)). The separate unloading sound speed - strain function (Figure 7.4(a)) accommodates the large change in wave velocities between shock and release states in the aluminum nitride. The parameters for this unloading curve were also derived iteratively to match the release waves in Figure 7.2(a) and Figure 7.2(b). In the calculation, when material begins to unload from compressive states, the local modulus evaluation abruptly changes from the loading curve to the unloading curve.

The shock and particle velocities associated with the transmitted wave profiles for both tantalum (2207 m/s, CE 43) and tungsten (2281 m/s, CE 44) 1.5 mm impactors onto aluminum nitride are plotted in Figure 7.4(b). The shock velocity is calculated from the arrival time of an increment of the stress wave at a chosen monitoring position in the aluminum nitride, and the distance from the impact interface to the monitored point. The displaced position of this monitoring point is included in the shock velocity calculation. Data points from Kondo, *et al.* (1982) are compared with this data extracted from the analysis of the present experiments. We observe that there is a good agreement with the two data points at a particle velocity of 8.6 km/s, defining the shock velocity of the plastic deformation wave. Three other data points from Kondo, *et al.* (1982), in the particle velocity range of these experiments, are also in excellent agreement with the shock velocities determined for the phase transformation wave. The data point near 175 m/s is in the elastic regime, albeit somewhat lower than that obtained in the material of the current study. (The reported longitudinal velocity in [Kondo, *et al.*, 1982] is 10000 - 10400 m/s compared to the 10730 m/s for the material used here.) From the calculated change in shock velocity with particle velocity at the phase transformation wave, an effective coefficient, S, in the linear shock velocity - particle velocity relationship is determined to be about 4.8; this is much larger than the value of about 2.0 determined to be the observed upper limit for shock compression of the preponderance of single phase materials [Jeanloz, 1989]. Kondo, *et al.* (1982) report shock velocity *versus* particle velocity data to about 3000 m/s, and a value of S of at least 3.4 is suggested by their fit to that data. These large values of S indicate that there are significant differences in the nature of compressibilities between single and multiple phase materials.

7.3 Discussion

The present experiments and analysis of aluminum nitride provide substantial evidence for a non-recoverable volumetric phase transformation under shock compression at a pressure of about 22 GPa. The fine time-resolution of the data permit accurate assessment of the initial permanent deformation, the onset of the phase transformation, the loading path through the transformation to final shocked states of 40 GPa, and the unloading behavior from these shocked states. Numerical analysis provides insight into the development of the three wave structure that forms from the initial shock at the impact interface, and is an effective analytical utility for establishing dynamic stress *versus* deformation behavior. The data are generally consistent with previously reported data for aluminum nitride.

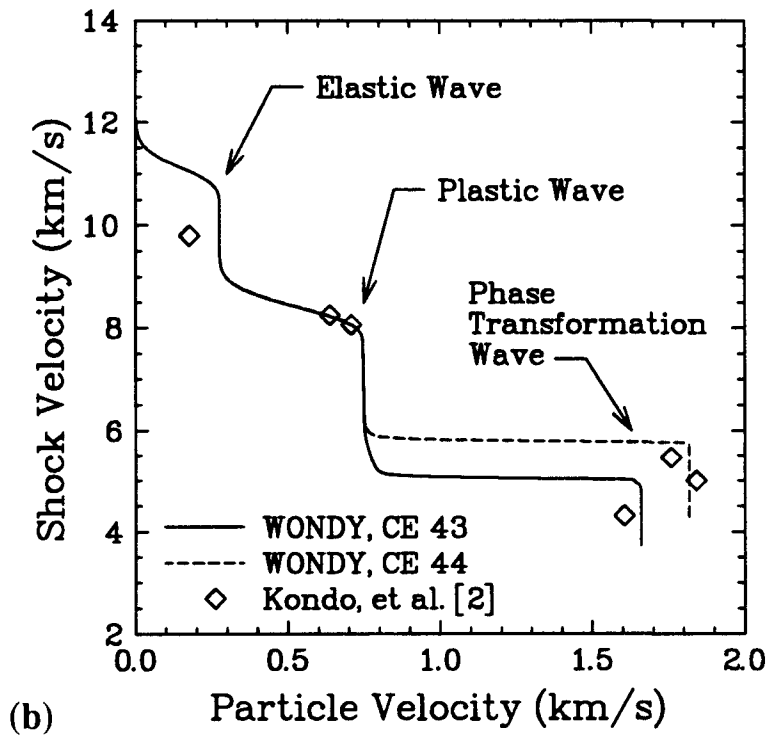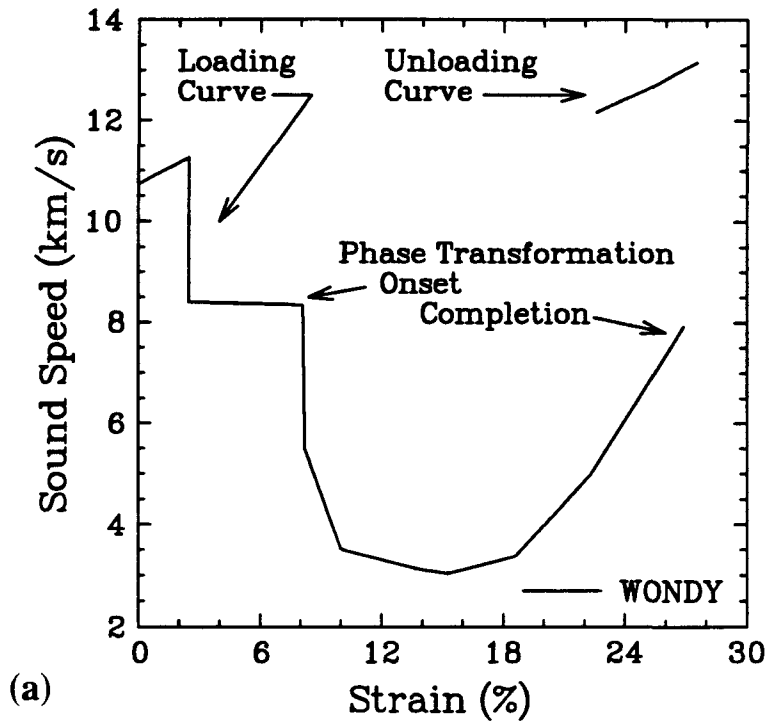Figure 7.4   (a) Characterization of aluminum nitride with sound speed function of strain. (b) Shock velocity *versus* particle velocity response of aluminum nitride.

These data and analyses of deformation provide a solid basis for the construction and evaluation of material models for this material, particularly in the accounting of the large energy dissipation that accompanies the phase transformation.

8 Shock-Compression and Spall Measurements on Tungsten Carbide

Velocity interferometry wave profile measurements have been made on several tungsten carbide ceramics. Hugoniot states for these materials ranging from approximately 5 to 60 GPa were investigated. A Hugoniot elastic limit of approximately 4 GPa, followed by strong hardening behavior, was determined. Several tests examined the spall failure of tungsten carbide and provided measurements of spall strengths in the range of 2.7-3.6 GPa which is markedly larger than for other ceramics. The velocity profiles provided specific shock and high-strain-rate material property data along with response measurements for computational model validation.

8.1 Background

Tungsten carbide is a high density ceramic with reasonably attractive shear and tensile strength properties in certain applications. The current study was undertaken to investigate the dynamic equation of state and strength properties of this material for purposes of computational modelling under high velocity impact applications. The effort was initiated and completed within a relatively short time frame and consequently does not represent a thorough investigation of the dynamic properties of tungsten carbide. Material from two suppliers was tested. Both shock compression and spall data were obtained from the series of seven shock profile measurements conducted.

A search for earlier shock wave data on tungsten carbide was also conducted in this study. Some previous work was uncovered. Hugoniot data on WC-5wt%Co was generated by McQueen et al. (1968; 1970) and has been tabulated in the LANL Shock Hugoniot Compendium [Marsh, 1980]. Also, several compression wave profiles on tungsten carbide using the free-surface capacitor technique were measured by Taylor, and by Hopson, and published in the LANL Shock Wave Profile Compendium [Morris, 1980]. Gust (1980) indicates shock Hugoniot experiments were performed at Lawrence Livermore National Laboratories, however only a Hugoniot elastic limit is provided in this reference. Steinberg (1991) has assimilated the above data and provided partial material property parameters in the framework of the Steinberg-Guinan model.

8.2 Materials and Experiment

Two tungsten carbides prepared by pressureless liquid-phase sintering were tested in this effort. The first was a fully dense tungsten carbide provided by Kennametal Inc. The other was extracted from 14.5 mm AP (BS-41) rounds. The Kennametal tungsten carbide contains 5.7% Co, 1.9% Ta and less than 0.3% Nb and Ti. The reported Rockwell-A hardness is 93 and the compressive strength is 5.8 GPa. The AP material contains 3-4% Ni, 0.4-0.8% Fe and 0.05-0.2% Co. The Rockwell-A hardness is 86-92. Static compressive strength for this material is 44 GPa and split cylinder test results provided a tensile

strength of 240-270 MPa [Holmquist, 1994]. Density and ultrasonic properties for the two materials are provided in Table 8.1.

Table 8.1:
Elastic Properties for Tungsten Carbide

Material	Density (kg/m^3)	C_l (km/s)	C_s (km/s)	C_o (km/s)	Bulk Modulus (GPa)	Poisson's Ratio
KM[1]	14930	6.895	4.165	4.941	364.5	.213
AP[1]	14910	6.918	4.149	4.991	371.4	.219

[1] KM refers to the K68 material obtained from Kennametal Inc. whereas AP identifies the tungsten carbide extracted from 14.5 mm (BS-41) armor piercing rounds.

Uniaxial strain compressive shock and release waves were produced in the tungsten carbide with a single stage powder gun facility as described in Section 2. A disc of impactor material (either tungsten carbide or aluminum in the present tests) was mounted in the projectile and was backed by a disc of polymethyl methacrylate (PMMA).

Table 8.2:
Experimental Conditions for Tungsten Carbide Impact Tests.

Test Number	Projectile[a] Material	Projectile thickness (mm)	Target[b] Material	Target Thickness (mm)	Impact Velocity (km/s)
WC-1	WC (KM)	3.370	WC (KM)	6.566	1.141
WC-2	WC (KM)	3.363	WC (KM)	6.542	1.566
WC-3	Al (6061-T6)	12.87	WC (AP)	2.985	1.039
WC-4	Al (6061-T6)	12.51	WC (AP)	2.994	0.687
WC-5	Al (6061-T6)	1.047	WC (AP)	2.986	0.361
WC-6	Al (6061-T6)	1.038	WC (AP)	2.980	0.446
WC-7	Al (6061-T6)	1.030	WC (KM)	3.357	0.405

[a] All impactors were backed by PMMA.
[b] Target diameters for test WC-1, WC-2 and WC-7 were slightly greater than 63 mm. For tests WC-3 through WC-6 diameters were just under 11 mm.

For the target, a disc of the tungsten carbide ceramic was mounted in the stationary supporting target fixture and an optical quality disc of single crystal lithium fluoride was intimately bonded with epoxy to the back of this ceramic sample. VISAR velocity profiles to be discussed subsequently were obtained by the methods described in Section 2. The impact parameters and component dimensions for the present series of impact experiments on tungsten carbide are provided in Table 8.2

8.3 Dynamic Strength

Compression wave profiles for Tests WC-1, WC-2 and WC-3 are shown in Figure 8.1. Test WC-3, which was performed on an approximately 3 mm sample of the AP tungsten carbide has been scaled to the 6.55 mm thickness of the Test WC-1 and WC-2 KM samples assuming centered wave behavior. Thicknesses of both the elastic and deformation shock for the WC-3 profile is probably unduly spread by this scaling. Comparison of the three profiles indicates consistent shock properties and comparable dynamic strengths for the two materials. Arrival times of longitudinal and bulk elastic waves are indicated to compare with arrivals of the deformation shocks in Figure 8.1. Tests WC-4 through WC-7 also provide compression profile information, although an unusual velocity excursion, which may be an experimental artifact and is discussed later, compromises this data to some extent.

The 6.5 mm thickness Kennametal tungsten carbide samples reveal a fairly distinct transition from the elastic precursor rise to the transition ramp region at approximately 70 m/s. Based on an acoustic impedance calculation this leads to a Hugoniot elastic limit of
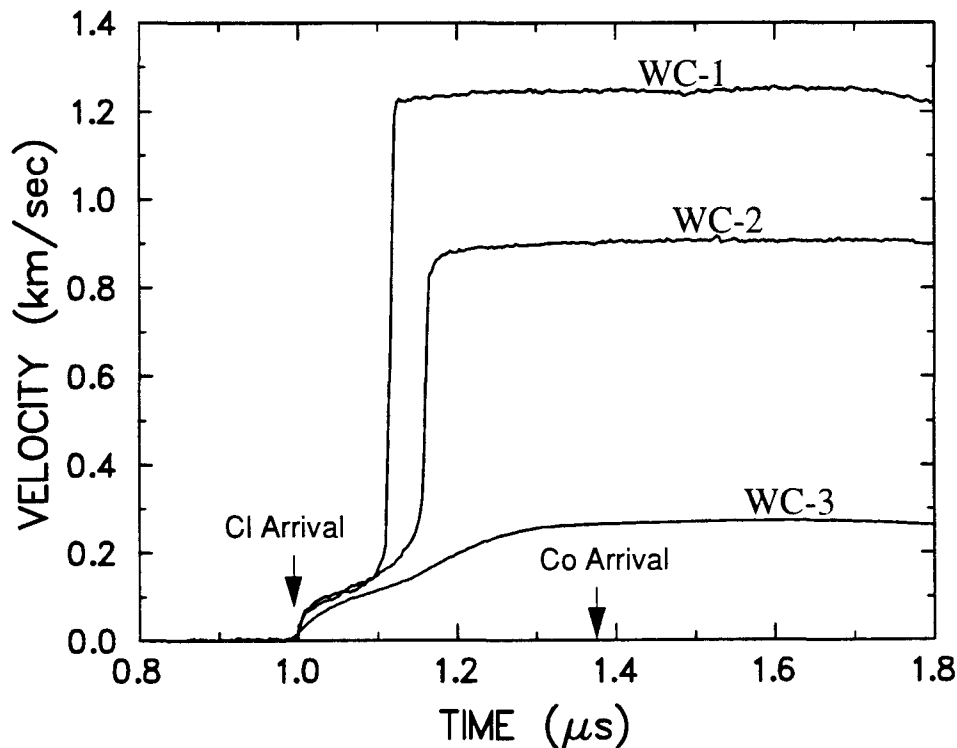

Figure 8.1   Compression shock profiles for tungsten carbide.

4.1 GPa. The thinner AP sample tested, WC-3, did not provide as distinct a transition level, however, a yield at about 70 m/s is not inconsistent with the behavior of this material, and indicates similar yield characteristics for both materials.

Material behavior within the transition ramp regime was analyzed in two ways. First, computational simulations of the precursor and transition ramp portions of the wave profile were performed using the one-dimensional Lagrangian wave code WONDY-IV [Kipp and Lawrence, 1982]. With this technique empirical parameters for the longitudinal modulus as a function of amplitude are adjusted until a best fit to the wave profile in the region of interest is achieved. The stress-strain relation derived from this fit is then accepted as the dynamic response of the tungsten carbide. The experimental profiles for Tests WC-1 and WC-2 are shown with the one-dimensional wave code solution in Figure 8.2.
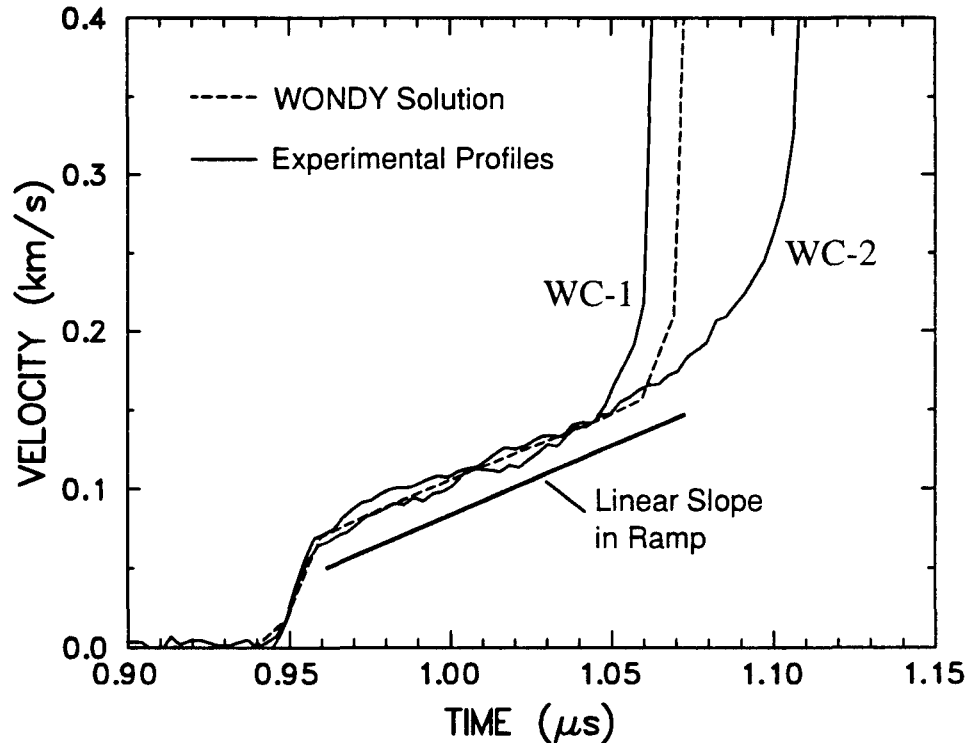
Figure 8.2 Compression shock profiles and WONDY computational solution emphasizing the ramp region of the elastic precusor.

An analytic solution was also performed assuming a linear rising velocity versus time behavior within the region of the ramp (Figure 8.2) and writing the wave velocity as,

$$c_r = \frac{c_e}{1 + \Delta u / \bar{u}},$$ (8.1)

where $\bar{u} = a_r l / c_e$. The precursor velocity is c_e, the thickness of the target plate is l, and a_r is the constant acceleration determined from the slope of the ramp wave in the mea-

sured profile. Also, $\Delta u = u - u_e$, where u_e is the particle velocity at the Hugoniot elastic limit. Both a_r and Δu have been corrected for the impedance difference between tungsten carbide and lithium fluoride assuming an elastic impedance for the WC and LiF, $(\Delta u = (Z_{WC} + Z_{LiF}) \Delta u_{meas}/2Z_{WC})$. Stress and strain are calculated from the Riemann integrals, $d\sigma = \rho_o c_r(u) du$ and $d\varepsilon = du/c_r(u)$.

Results of the stress-versus-strain behavior within the ramp region determined from both the computational simulation and the analytic solution for the axial $\sigma_x - \varepsilon$ behavior are provided in Figure 8.3. Comparison is made with the linear mean stress curve calculated from the ultrasonic bulk modulus and with the difference $3(\sigma_x - \sigma_m)/4$ which would provide the shear stress behavior if the volumetric compressibility during the shock compression process tracked the ultrasonic compressibility.

If there is onset of an inelastic deformation mechanism at the 4 GPa break in the measured wave profile in tungsten carbide, as common understanding of the process tends to support, then the ramp structure in the profile cannot be described with simple von Mises plasticity as indicated in Figure 8.3. Several hardening mechanisms may potentially explain the observed behavior. The elastic loading path could contact a pressure hardening yield surface at the Hugoniot elastic limit (HEL). Subsequent loading would lead to increased stress rise due to the increasing shear stress with confining pressure on the pressure hardening yield surface. Alternatively, the HEL may correspond to the intersection of the elastic loading path with a deformation hardening yield surface. Due to post-yield deformation in the shock wave the initial yield surface would evolve through a succession of
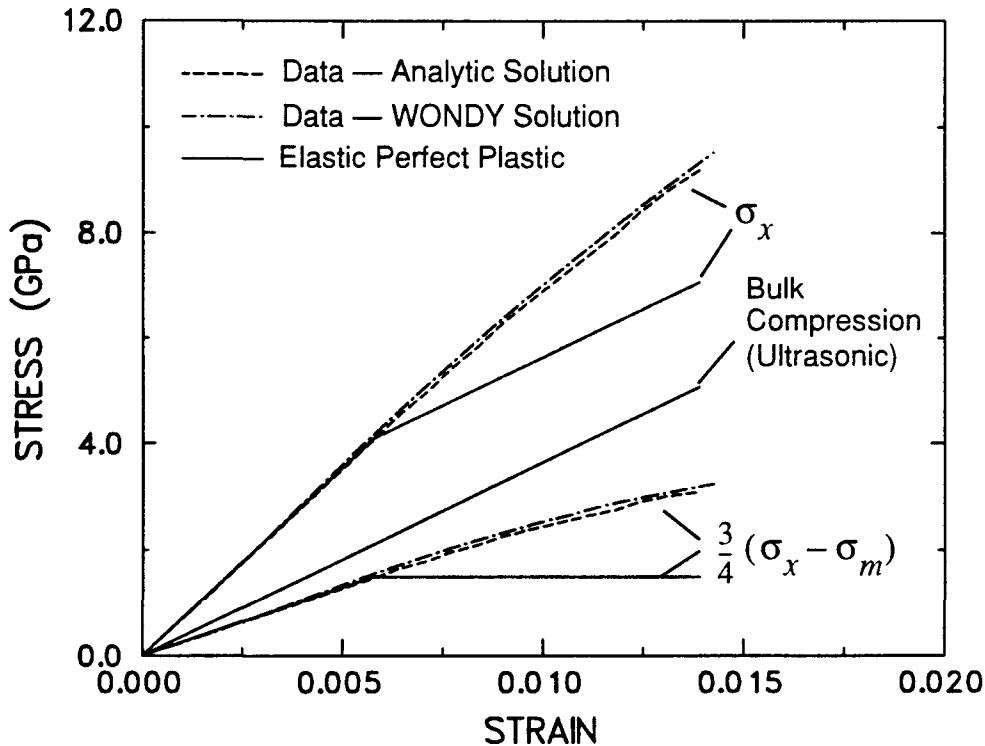

Figure 8.3   Stress versus strain behavior in ramp region of the wave profile.

states to a final yield surface consistent with later states in the ramp wave. Evolution of the yield surface would be determined by a deformation hardening law and could account for the ramp behavior characteristic of the early inelastic deformation.

There is a further, less commonly considered, mechanism for hardening which could account for the observed wave profile structure. Rather than an increase in the stress deviator with inelastic deformation, an increase in the mean stress state above that predicted by compressibility of the fully dense solid, could account for the observed behavior. Such an elevated mean stress versus volume curve is possible if dilatant void volume is generated during the shear deformation process.

Of course, all three of the hardening mechanisms proposed could be operating collectively, and rate dependence of these effects may also be playing a role. Of the three hardening mechanisms, pressure hardening is the most difficult to reconcile with the second order character of the elastic-to-inelastic deformation transition. (The transition to a ramp wave represents a discontinuous jump in the curvature of the stress-versus-strain curve and not the slope.) In principal deformation hardening or dilatancy hardening laws could be constructed which could simulate the observed transition to ramp wave structure.

Although the present wave profile experiments on tungsten carbide serve to illuminate some of the possible mechanisms of inelastic deformation operating in the shock compression of this material, they are not sufficient to discriminate among the initial yield and hardening mechanisms. Further dynamic testing is needed. In particular tests measuring both longitude and transverse stress would be especially revealing.

8.4 Hugoniot Properties

Hugoniot states for the present tungsten carbide were determined assuming a precursor velocity equal to the longitudinal ultrasonic elastic velocity of 6.95 km/s. Hugoniot states for Tests WC-1, WC-2 and WC-3 are shown in a shock velocity versus particle velocity plot in Figure 8.4 and compared with the data of McQueen et al. (1968, 1970). The two higher amplitude states are in reasonable agreement with the date of McQueen. The relatively broad shock wave for Test WC-3 lends some ambiguity to the experimental shock velocity at this amplitude. Nevertheless this data point cannot be reconciled with the measurements of McQueen, although the trend of the lower three or four data points of McQueen tend to fall above the linear expression. Precursor states and ramp region for these data are also indicated in Figure 8.5. Corresponding Hugoniot pressure versus specific volume states for this tungsten carbide are provided in Figure 8.6.

The tungsten carbide tested by McQueen et al. (1968, 1970) was also approximately 5% cobalt by weight, however the reported density of 15,013 kg/m^3 is about 1/2% higher than the present Kennametal material. This density difference accounts for about half of the discrepancy between the McQueen et al. Hugoniot and the present Hugoniot data in Figure 8.6. Since the present Hugoniot states were calculated based on an ultrasonic velocity for the elastic precursor (a lower limit), it appears that the present Hugoniot is slightly stiffer than that reported by McQueen and coworkers.
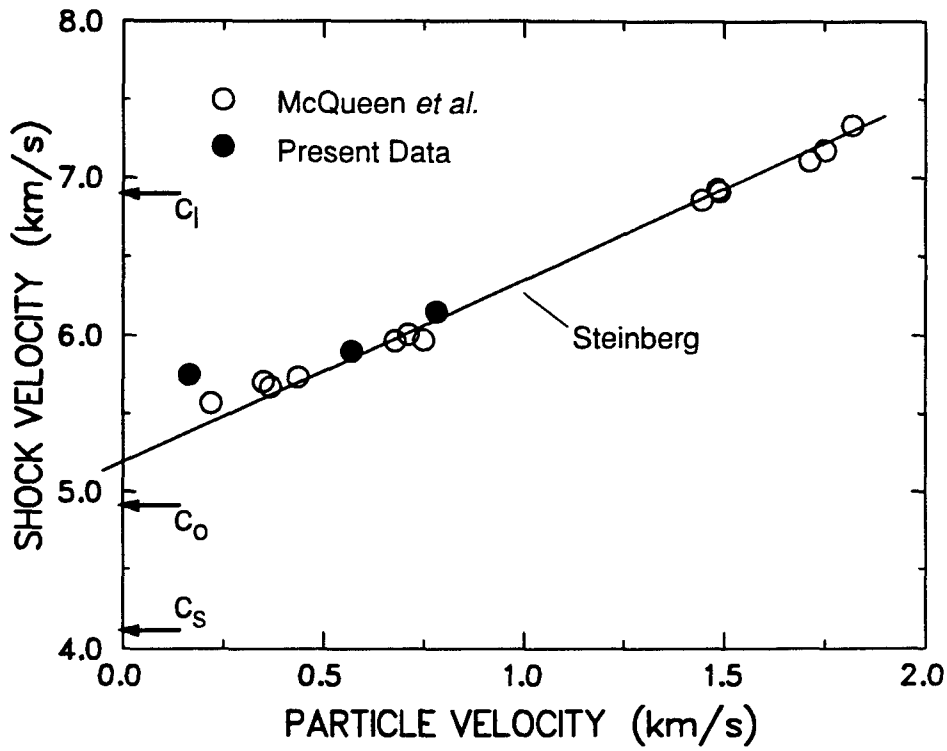
Figure 8.4   Shock velocity versus particle velocity for tungsten carbide.
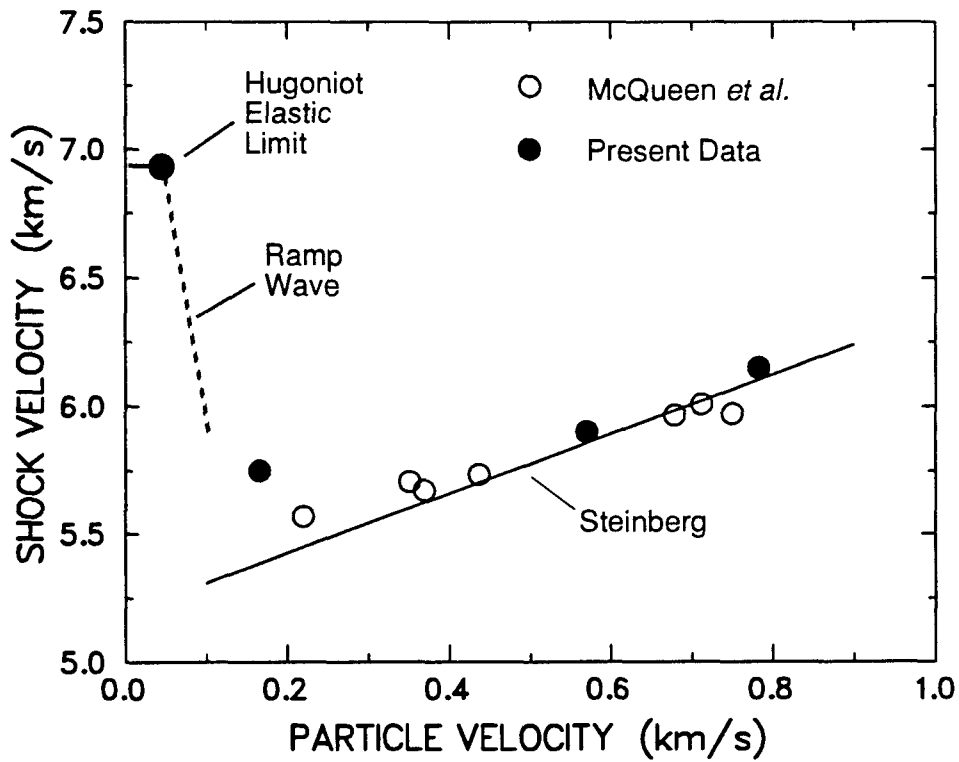
Figure 8.5   Shock velocity versus particle velocity data for tungsten carbide emphasising lower pressure data, including precursor elastic limit and ramp wave region.

60
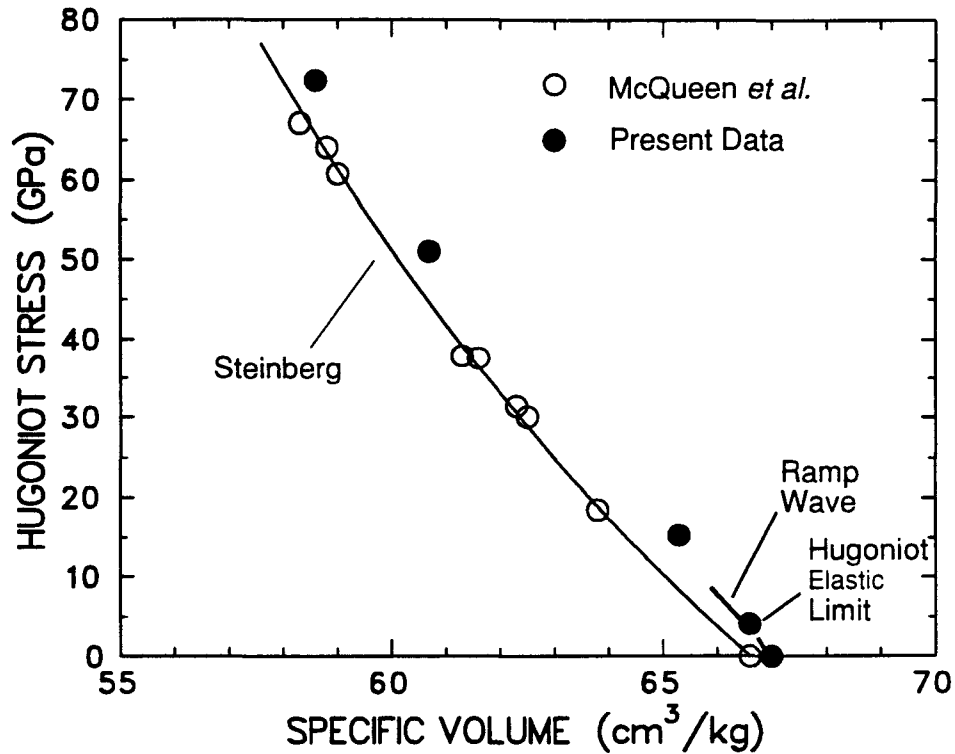
Figure 8.6   Hugoniot stress versus specific volume for tungsten carbide.

8.5 Spall Strength

Release waves originating from the rear of the aluminum impactor and from the lithium fluoride window interface interact within the tungsten carbide samples carrying the material rapidly into tension. The dynamic tensile strength (spall strength) of tungsten carbide was exceeded in the present tests and the time history of the spall process was imaged in the measured spall pullback signal within the velocity profile recorded at the window interface. Interface velocity profiles for test WC-5, WC-6, and WC-7, in which spall occurred, are shown in Figure 8.7.

The spall strength of tungsten carbide can be calculated from the spall pullback signal identified in Figure 8.7. The present data provide an opportunity to compare two methods for determining the spall strength when an interferometer window is used. The appropriate velocity levels are identified for Test WC-6 in Figure 8.7 for the spall analysis. First, if the full amplitude of the pullback is used, then the appropriate relation for the spall strength is

$$\sigma_{sp} = \frac{1}{2}(Z_s + Z_w)(u_{max} - u_{min}) - Z_w u_{max}. \tag{8.2}$$
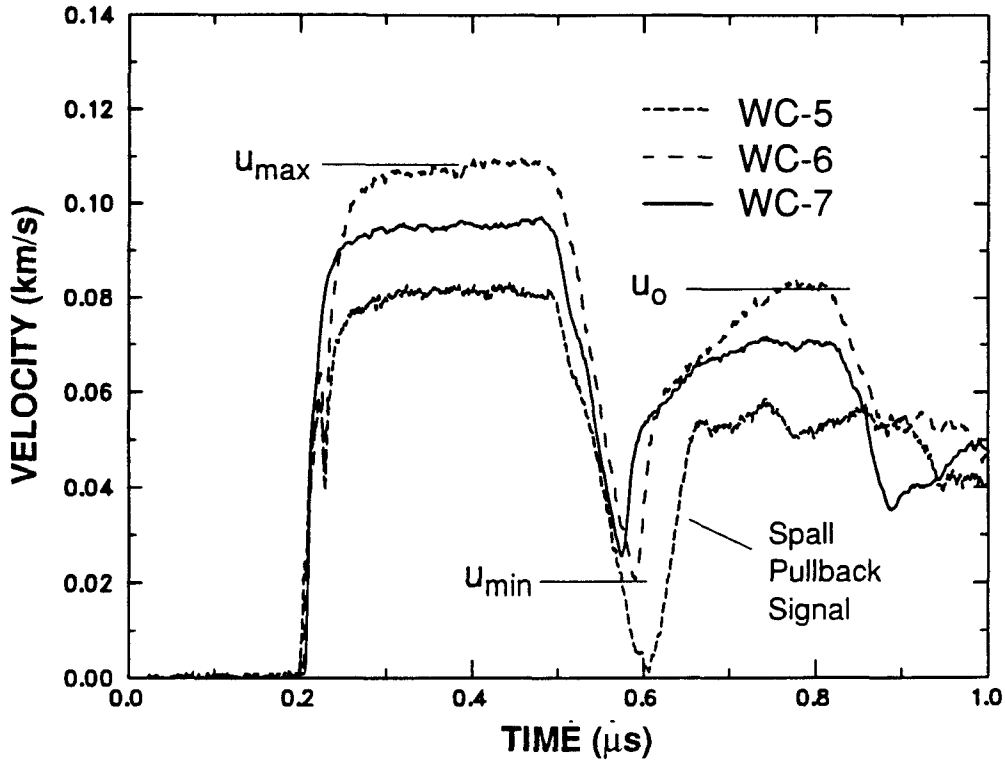
Figure 8.7   Wave profiles emphasizing spall pullback signals in tungsten carbide.

In Equation 8.2 Z_s and Z_w are the shock impedance of the sample material and window material, respectively. Equation 8.2 assumes approximately linear behavior of stress-strain response of the sample and window material and ignores the complications of corrections for wave dispersion and elastic-plastic behavior which have been discussed in the literature [Grady and Kipp, 1993]. The down side of Equation 8.2 is that it can be a difference of two large quantities each of which may have uncertainties. This is not a serious problem with the present data, however.

An alternative expression for the spall stress is provided by the relation,

$$\sigma_{sp} = \frac{1}{2} (Z_s + Z_w) \ (u_o - u_{min}) \ . \tag{8.3}$$

Equation 8.3 does not suffer from the differencing problem of Equation 8.2. On the other hand it assumes that stress at the spall plane has relaxed to zero before the reflected wave has returned to the recording interface. This depends on experiment design and the time history of the spall process, but often this relaxation is not complete and the spall strength calculated from Equation 8.3 is a lower bound. With the present data spall strengths have been calculated with both Equation 8.2 and Equation 8.3. Results are provided in Table 8.3 and plotted in Figure 8.8.

62

Table 8.3:
Spall Properties of Tungsten Carbide

Test Number	Material[1]	u_{max} (m/s)	u_{min} (m/s)	u_o (m/s)	σ_{sp}[2] (GPa)	σ_{sp}[3] (GPa)
WC-5	AP	81	1	56	3.56	3.21
WC-6	AP	108	21	82	3.60	3.56
WC-7	KM	96	26	71	2.75	2.62

[1] KM refers to the K68 material obtained from Kennametal Inc. whereas AP identifies the tungsten carbide extracted from 14.5 mm armor piercing rounds.
[2] Analysis method one (Equation 8.2).
[3] Analysis method two (Equation 8.3).

8.6 Discussion

It is important to recognize that the two tungsten carbide ceramics tested in the present study are, in fact, metal ceramic mixtures and that this feature may profoundly influence the dynamic properties uncovered in this study. Metals added in the ceramic processing congregate at ceramic grain boundaries and junctions, filling most of otherwise porous regions in the ceramic. Volume fraction of metal in the Kennametal (KM) material is 11%-12% while the AP material is slightly less at 8%-10%.

This metal content may be responsible for the reduced strength of tungsten carbide (Hugoniot elastic limit of approximately 4.0 GPa) in comparison with other ceramic materials. On the other hand the strong hardening behavior of this material may also reflect the metal component. The higher compressibility of metal relative to the ceramic would lead to increasing ceramic-ceramic contact with increasing pressure, and consequently increasing manifestation of ceramic strength with pressure.

The remarkably large spall strength of tungsten carbide is probably a consequence of enhanced toughening brought about by the metal component. Differences in spall strength between the Kennametal and AP materials need to be studied further but are most likely a consequence of differences in bonding characteristics of the nickel-iron and the cobalt-tantalum in tungsten carbide. Anomalous excursions (glitches) in the compression velocity profiles for Tests WC-4, WC-5 and WC-6 were noted (see compression profiles for tests WC-5 and WC-6 in Figure 8.7). Considerable effort was expended in attempting to explain these features but we were unsuccessful. They appeared clearly in the data 1 and data 2 traces (90 degree out of phase velocity fringe records) and not in the beam intensity so they appear to record a true velocity excursion. We found nothing in the target geometry that could lead to a wave reflection. Nonetheless, it is our opinion that this feature is an artifact of the experiment.
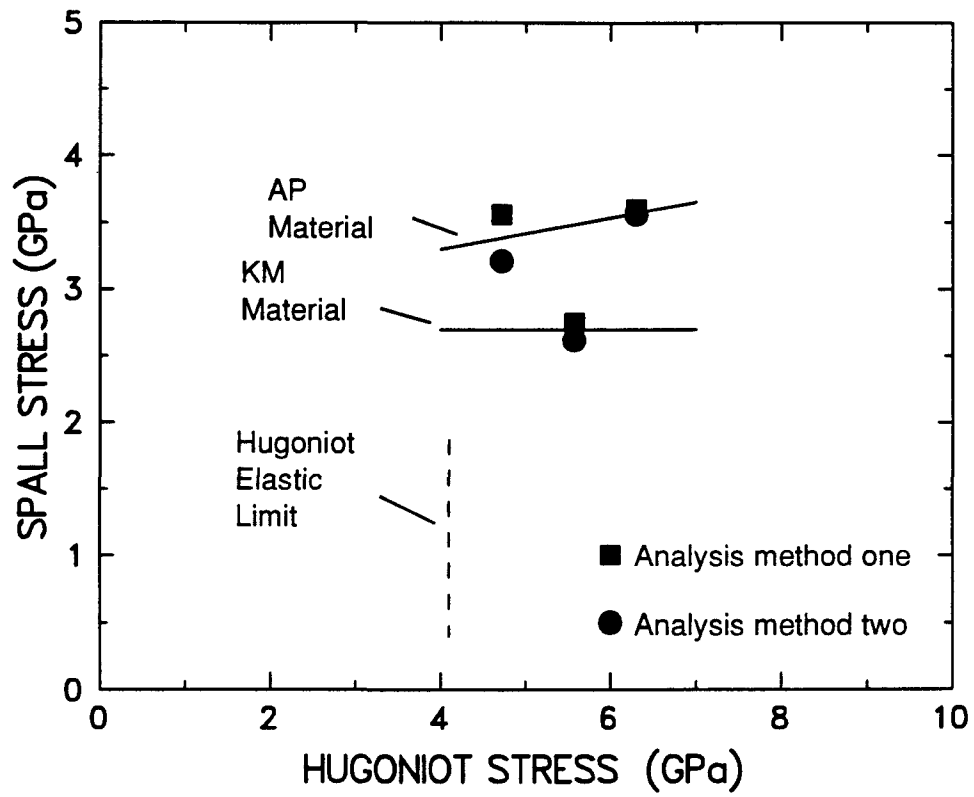
Figure 8.8   Spall strengths determined from the present tests on tungsten carbide.

9 Shock Compression Experiments on Quartz Rock Investigating a Critical Stress Transition in the SiO_2 Structure

Two shock compression experiments on the same quartz rock tested by Zhugin and Krupnikov (1987) have been performed using high resolution velocity interferometry diagnostics [Grady and Zhugin, 1994]. Peak stress levels of approximately 26-28 GPa were achieved in the present tests. A Hugoniot elastic limit of 6.0 GPa and a compression anomaly at 23.4 GPa on the shock Hugoniot were observed in the experimental results. The latter stress value is in good agreement with a transition stress of 23 GPa previously reported by Zhugin and Krupnikov (1987). A critical transition stress level identified in the work of Zhugin and Krupnikov (1987) and in the present study suggests a need for re-examining both earlier interpretations of shock wave results for quartz, and theories of the shock transition process. A closer relation between the shock transition process and the static crystalline-to-amorphous transition at about 20 GPa reported by Hemley et al. (1988) should be considered. Theories of the transformation based on free-energy/kinetic concepts (Sikka, 1992) warrant serious consideration in light of the existence of a critical shock transition level, and the remarkably close dynamic and static transition stress values. Earlier interpretation of a constant shock velocity segment of the Hugoniot through the mixed-phase region over a broad stress range may be erroneous in light of the more complex shock structure observed. Reinterpretation would suggest a concave Hugoniot segment with higher density dynamic compression states at comparable stress levels. The present tests suggest transition toward the high-density 6-coordination structure of SiO_2 rather than the relatively minor crystallographic change associated with the coesite phase. Similarities among the present wave profile measurements on SiO_2 and comparable measurements on ZrO_2 are noted.

9.1 Background

At the All-Union Workshop on Physico-Chemical Properties of Matter convened at Lake Baikal, Russia during the period of August 17-24, 1990, Zhugin and Krupnikov reported the first definitive observation of a wave profile feature indicative of a critical transformation stress in the α-quartz form of SiO_2 [Zhugin and Krupnikov, 1987]. In that work, samples of quartz rock were subjected to plane shock waves between about 21 and 29 GPa. Transmission compressive stress wave profiles were measured with high-resolution piezoresistive manganin stress transducers. A compression anomaly was noted in the data at approximately 23 GPa — presumably related to the onset of lattice instability and phase transformation in the SiO_2 structure. Since a critical transformation stress had not been noted in earlier shock-wave studies on SiO_2, common thinking was that the 4- to 6-coordination transformation was diffused over a broad range of pressure. This behavior was thought to account for the anomalous constant shock velocity and linear Hugoniot segment observed over the correspondingly broad particle velocity range.

At the Lake Baikal Meeting it was concluded that independent measurements of the wave profile characteristics with a different time-resolved diagnostic technique would lend support for this previously unreported feature. Time-resolved velocity interferometry mea-

surements were made at the Sandia National Laboratories Shock-Compression Facilities and the authors of the earlier work kindly provided samples of the same quartz rock tested by them.

9.2 Experimental Method

Controlled-impact planar shock-wave experiments were performed on the propellent launch facility described in Section 2. Projectile and target configuration for the shock experiments on quartzite are illustrated in Figure 9.1. A tungsten impact plate launched at near the maximum velocity of the propellent gun (~2.3 km/s) was judged sufficient to exceed the 23 GPa transition stress reported by Zhugin and Krupnikov (1987). The low density PMMA (polymethyl methacrylate) backing was intended to provide for a partial release wave following the initial compressive shock wave. Velocity history of the compressive shock wave was measured at an interface between the quartz rock sample and a lithium fluoride window with the diffused-surface velocity interferometry (VISAR) method of Barker and Hollenbach (1972).

Two shock-compression experiments of the configuration just described were successfully completed. Dimensions and impact parameters for the two tests are provided in Table 9.1
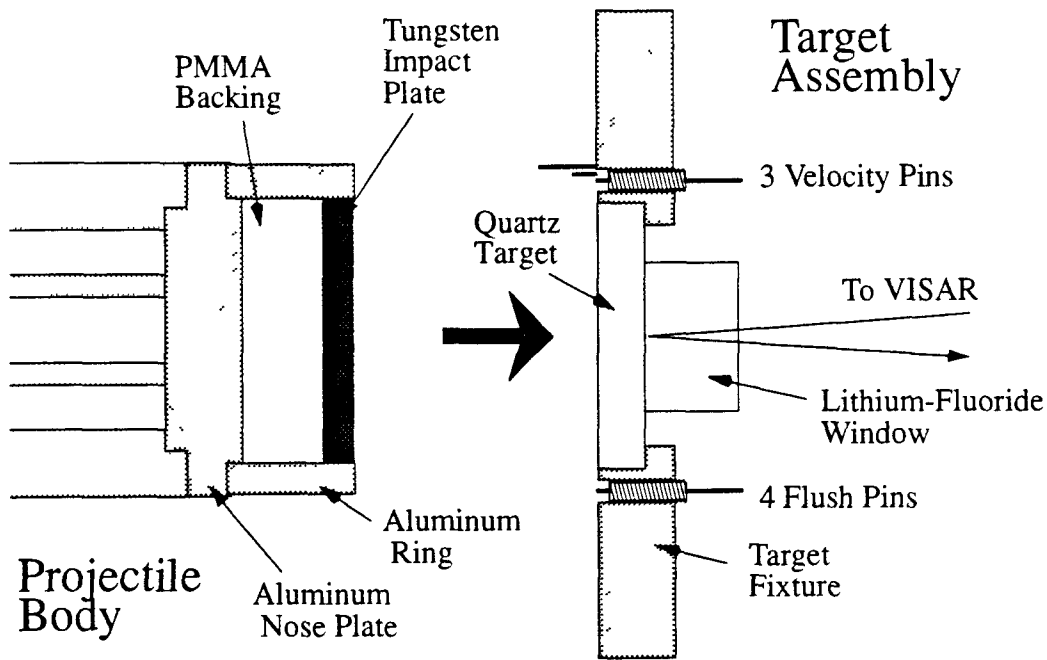

Figure 9.1   Experimental configuration for shock compression and release measurements in quartz rock.

Table 9.1:
Experimental Parameters

Test Number	Sample Density (kg/m^3)	Tungsten Thickness (mm)	Quartz Thickness (mm)	PMMA Thickness (mm)	Impact Velocity (km/s)
SV1	2645	2.990	4.996	6.382	2.19
SV2	2645	2.989	4.936	6.396	2.30
Tungsten disc diameter — 35.0 mm. Quartz disc diameter — 35.0 mm. Lithium fluoride dimensions — 19.1 mm thickness by 25.2 mm diameter.					

9.3 Experimental Results and Analysis

The measured experimental profiles for Tests SV1 and SV2 are provided in Figure 9.2. An expanded view of the wave front is shown in Figure 9.3. The arrival times of the two wave profiles are arbitrary and were selected to easily visualize the separate profiles. The transit time of the elastic shock wave through the quartz sample was not measured.

Lithium fluoride is a reasonably good impedance match for quartz (LiF has a slightly higher shock impedance) and the observed profiles are believed to be representative of the in-material motion history.

An elastic shock wave was clearly observed in both tests with a profile amplitude very close to 0.38 km/s. Based on earlier studies (Grady *et al.*, 1974) on a similar density quartz rock, an elastic shock velocity of 6.2 km/s was assumed in order to perform Hugoniot analysis on the present compressive shock-waves.

A profile amplitude of approximately 1.40 km/s was determined for the second plateau amplitude for both SV1 and SV2 immediately before the ramp in velocity up to the velocity peak. This plateau level is believed to correspond to the transition level identified by Zhugin and Krupnikov (1987) with manganin gage techniques.

Table 9.2:
Hugoniot Data

Profile Velocity (km/s)	Hugoniot Particle Velocity (km/s)	Shock Velocity (km/s)	Hugoniot Stress (GPa)	Hugoniot Specific Volume (cm³/kg)
Elastic Hugoniot State				
0.38	0.363	6.20	5.96	355.9
Transition Hugoniot State				
1.40	1.56	5.50	23.4	273.6

Hugoniot analysis based on impedance match methods was performed using the elastic and transition profile amplitudes determined above. Hugoniot results are provided in Table 9.2. A transition stress amplitude of about 23.4 GPa is in good agreement with the 23 GPa value reported by Zhugin and Krupnikov (1987).
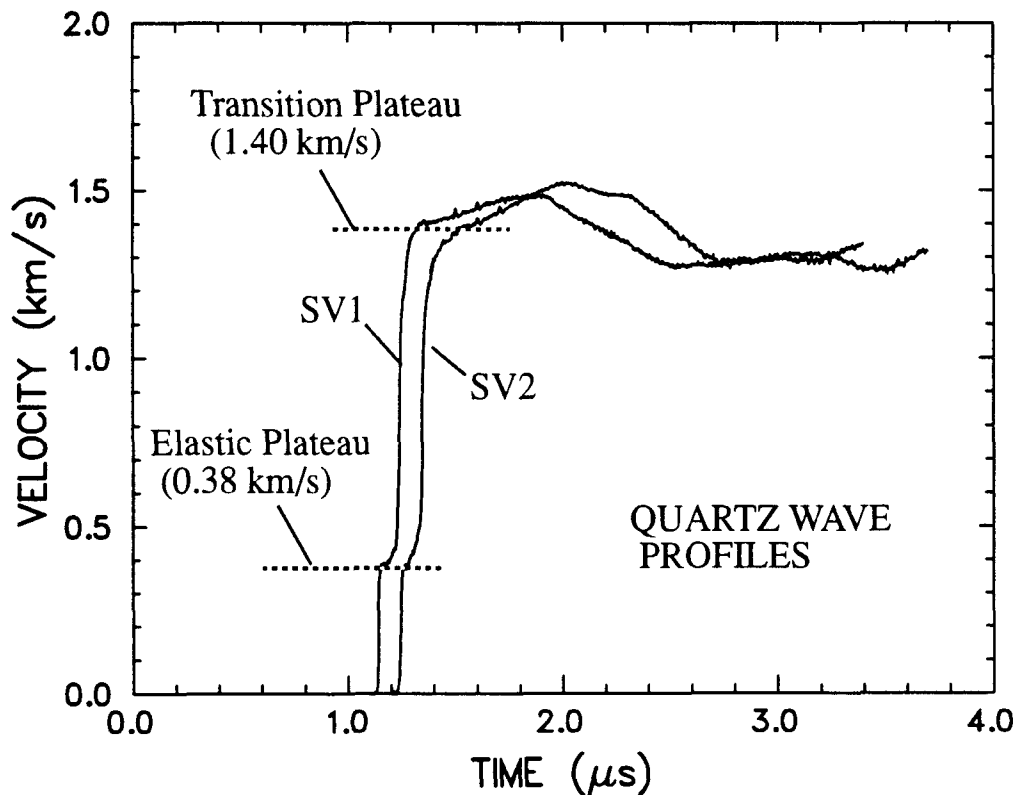

Figure 9.2   Experimental VISAR profiles for Tests SV1 and SV2 on quartz rock.

There are some concerns, however, about the impedance match Hugoniot analysis in light of the dramatic change in compression above the critical state.

A slight inflection in the compression profile was also observed at a compressive profile velocity amplitude of about 1.15 km/s. This inflection was more noticeable in Test SV1 than in Test SV2 (see the Figure 9.3 expanded scale). This difference was believed to be due to a somewhat larger glue bond thickness (~2μm) between sample and lithium fluoride for Test SV2. Consequently, Test SV1 is considered to be the higher resolution wave profile. The source of this inflection is not understood and it was ignored in the Hugoniot analysis.

Above the 1.40 km/s plateau level, particle velocity rises gradually to a peak value. The rate of ramping and peak value for Test SV2 are somewhat higher — consistent with the slightly faster impact velocity for this test (Table 9.1). Overtake by the trailing release wave prohibits achievement of the maximum particle velocity compatible with the impact conditions at the present sample thickness.

Quartz Hugoniot states from the present tests (Table 9.2) are compared with the corresponding stress versus particle velocity Hugoniots for tungsten in Figure 9.4. It is clear that particle velocities at the impact interface closer to 1.85-1.95 km/s were achieved and that significant peak attenuation occurred after transmission through the 5-mm sample thickness. Several assumptions were pursued to estimate the impact compression state.
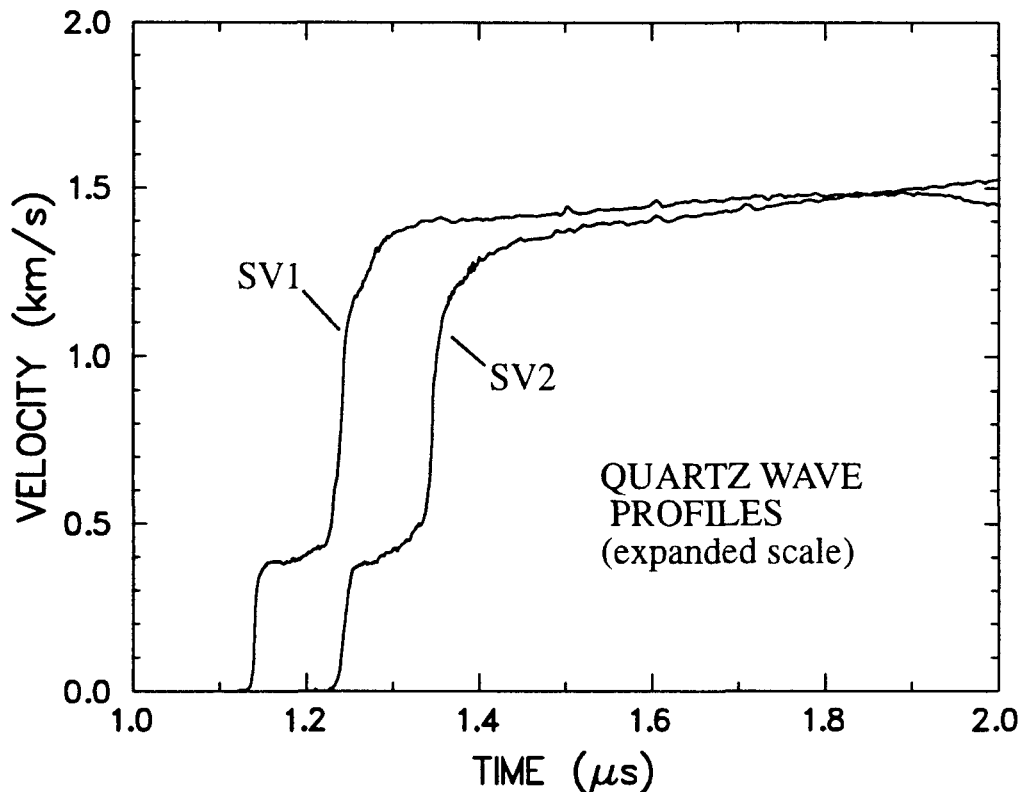

Figure 9.3   Experimental VISAR profiles for Tests SV1 and SV2 on Quartz rock. Expanded scale view of compressive wave.

First, it was assumed that the final state was achieved through a compressive shock that has been overtaken by the release wave. (Test SV1 was considered in this analysis.) The fastest shock velocity possible which is consistent with overtake by the release wave at 5 mm is 3.1 km/s. This leads to a maximum stress jump of 2.6 GPa and a minimum specific volume change of approximately 40 cm^3/kg.

Alternatively, the assumption of a linear ramp to the intersection particle velocity state and simple centered wave propagation led to a lower final stress state and a specific volume change closer to 55 cm^3/kg. Stress profiles measured by Zhugin and Krupnikov (1987) indicated an exponential-like convergence to the peak stress and it seems sensible that the present volume change estimates of 40-55 cm^3/kg represent a lower bound.

9.4 Discussion

Although the present tests provide strong support for the occurrence and stress level of the compression anomaly reported by Zhugin and Krupnikov (1987), they do not demonstrate the definitive three-wave structure, indicative of elastic yield and first-order phase transformation, observed in certain compounds. Clearly, higher amplitude experiments of the present type on the quartz rock would be needed to reveal such wave structure. Unfortunately the required impact velocities could not be achieved on the available impact facili-
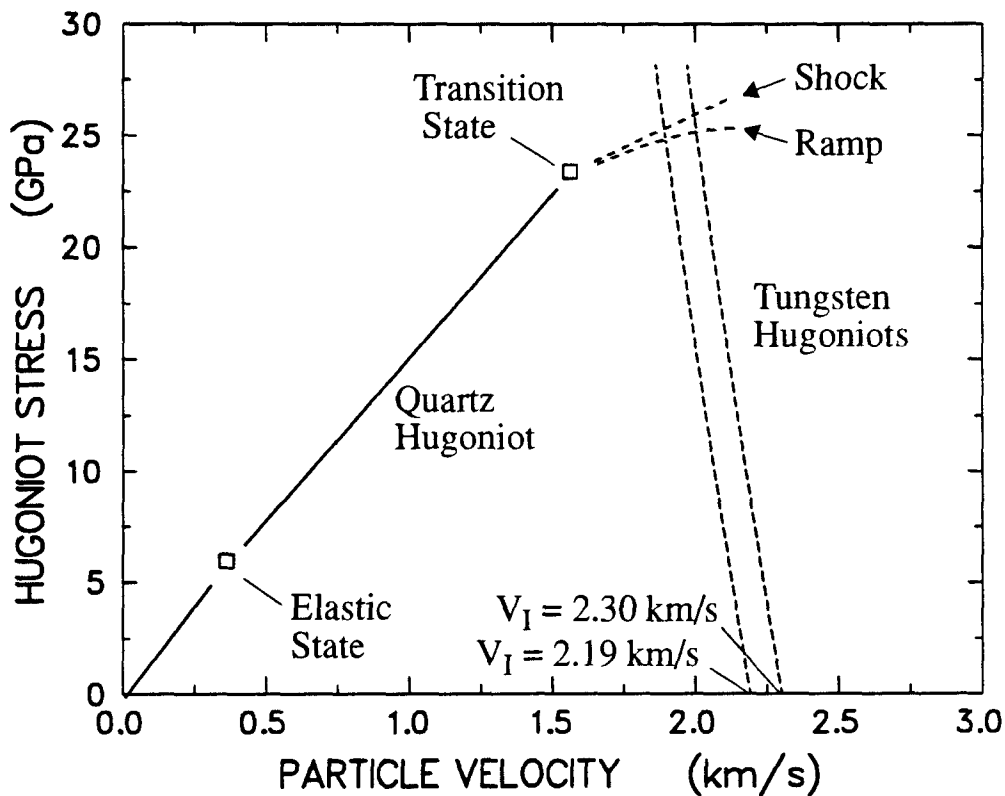

Figure 9.4   Quartz Hugoniot states and assumed interactions with the tungsten Hugoniot for the present shock-wave experiments.
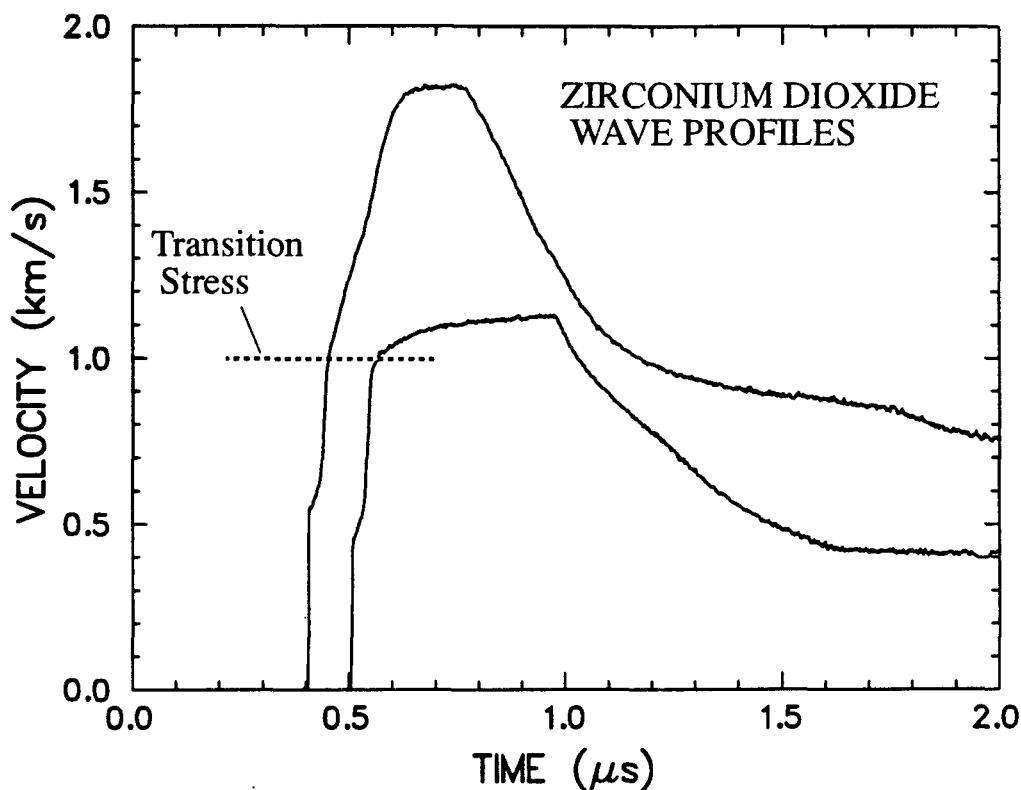
Figure 9.5   Experimental VISAR profiles for ZrO_2 indicating yield and transition characteristics.

ty. Also, other impact configurations, such as reshock or symmetric impact, may be more appropriate to investigate the present phenomenon.

For comparison, however, we show similar VISAR wave profiles measured on another oxide, ZrO_2, in Figure 9.5, which reveal a similar ramp structure above the transition plateau at lower impact velocity and a definitive 3-wave structure at a higher impact amplitude. The existence of similar wave structure in quartz would require further testing.

The occurrence of a critical transformation stress has interesting implications concerning the molecular and microstructure transformation mechanisms in the α-quartz structure. The existence of metastable mixed-phase Hugoniot states over a broad stress range in quartz was inferred from the interpretation of earlier shock data. A theory of microstructural deformation and thermal heterogeneity was proposed (Grady, et al.,1975; Grady, 1980) which was consistent with this metastable Hugoniot along with much of the dynamic and post-shock recovery data.

Because of the new wave profile data which indicates a critical transition level for lattice instability in the quartz structure, both the earlier shock data interpretation and phase transformation theory should be revisited. In light of this observation, recent static compression work of Hemley et al. (1988) should be noted in which a crystal-to-amorphous

transition in quartz at approximately 20 GPa was reported. This transition has been explained in terms of free-energy/kinetics arguments (Sikka, 1992) in which the α-quartz crystalline state is driven by elevated pressure to a high free energy state with respect to both the high density crystalline and amorphous state, but transformation is prohibited by transition kinetics. When the mechanical stability limits are achieved (spinodal decomposition) the material follows the easiest kinetic path to an amorphous high density state. Molecular dynamics simulations of the α-quartz transition have reasonably reproduced the expected transition pressure and volume strain (Tse and Klug, 1992; Chaplot and Sikka, 1992). Clearly this proposed transformation mechanism also warrants consideration for the shock transition process in quartz, considering the remarkably close critical stress levels reported in the static work of Hemley *et al.* (1988), and in the dynamic studies of Zhugin and Krupnikov (1987) and the present experiments.

Earlier interpretation of shock wave results which led to a broad Hugoniot range (approximately 20-35 GPa) in which the shock velocity remained constant with increasing particle velocity also needs to be reexamined. Wave structure above the 20 GPa level is apparently subtle and requires high-fidelity wave profile diagnostics to resolve. Earlier shock-wave diagnostics would have easily missed this additional structure. The consequence would have been to report a constant shock velocity (the transition shock velocity) along with the peak particle velocity. Shock velocities would again begin to increase with particle velocity only after the 23 GPa transition shock was over driven. This experimental interpretation of the constant shock velocity region in quartz seems inherently more reasonable than earlier explanations based on equation-of-state or kinematic arguments.

The implication of this interpretation is that the dynamic compression curve of α-quartz would lie below the previously reported Hugoniot curve, achieving higher densities at corresponding pressures. As noted in the earlier analysis, transition volumes in excess of 40-55 cm^3/kg are suggested for the impact amplitudes achieved. This significantly exceeds the volume strain predicted from reported Hugoniot curves for quartz. The transformation volumes at ambient conditions for the α-quartz-to-coesite structure and the α-quartz-to-stishovite structure are approximately 33 and 143 cm^3/kg, respectively. The present tests would suggest that the shock transition at 23 GPa is proceeding to the high-density 6-coordination structure of SiO_2 rather than toward the relatively minor crystallographic change coesite structure.

10 Precursor Attenuation in Ceramics

Because of the transient times involved in the compressive shock failure and flow process, the possibility of rate-dependent strength properties of ceramic must be considered in the computational evaluation of projectile-target interactions. A manifestation of rate-dependent strength is provided in controlled shock wave experiment through the evolution and attenuation with propagation distance of the elastic-to-inelastic transition precursor wave observed in wave-profile measurements. In the present study shock wave data on ceramics have been surveyed for evidence of rate-dependent precursor decay. The ceramics which have been investigated are aluminum oxide, aluminum nitride, boron carbide, silicon nitride and titanium diboride. Only boron carbide shows evidence of precursor attenuation within the range of the data.

10.1 Background

The stress versus deformation response of solids subjected to intense impulsive loads is expected to depend on the rate of loading. It is common, therefore, to incorporate the rate-sensitive behavior of materials into the constitutive models developed to model the dynamic response.

Specimens of the solid material subjected to controlled plane-wave impact experiments with high-resolution wave profile diagnostics are believed to provide a sensitive test of the extent of rate sensitivity exhibited by the material. In particular, the evolution of the shape of elastic precursor waves as they propagate through increasing distances in a target material is expected to provide strong evidence for the rate dependent yield and flow behavior of solids.

The concept of elastic precursor attenuation and the relation of this effect to the Maxwell-solid behavior of materials has been explored by Duvall (1978). Experimental observations of elastic precursor decay in quartz rock were reported by Ahrens and Duvall (1966), and numerous further examples have been documented in the intervening years. Perhaps the most in-depth investigation of the underlying physics of precursor decay has been conducted on lithium fluoride [e.g., Asay et al., 1972]. Rate sensitivity is an integral ingredient of the computational model for ceramics developed by Steinberg (1991). Recently Partom (1994) has noted certain difficulties in reconciling rate-sensitive viscoelasticity models with experimental wave profiles on ceramics

Studies on the rate sensitivity of ceramics, and on precursor attenuation in particular, are sparse and results to date have been contradictory. The predominant data appears to have been generated on aluminum oxide ceramic. One study has reported elastic precursor attenuation in aluminum oxide over sample thicknesses of a few millimeters to 25 millimeters [Rosenberg et al., 1988]. In contrast, measurements reported by Cagnoux and Longy (1987) for aluminum oxide did not indicate precursor decay.

In the present investigation the precursor waves of experimentally measured wave profiles on selected ceramics using velocity interferometry methods were examined for precursor decay trends. In all cases relatively pure and nearly full density ceramics were tested. In

general very little evidence for precursor attenuation was found for the ceramics investigated. Boron carbide may be the one exception, indicating some precursor attenuation over the thickness range examined.

10.2 Precursor Wave Properties for Ceramics

To investigate the evolution of elastic precursor waves with propagation distance we examine shock wave data on selected ceramics for which the thickness of the test samples have been varied over the range of about 2.5 mm to 15 mm. On all experiments discs of the test ceramic were backed by lithium fluoride window material and full shock compression and release waves were measured at a central point at the interface between sample and window material. Details of the experimental method are described in Grady (1992a, 1992b) and discussed in Section 2 of the present report. In the present study only the precursor wave of the shock profiles have been examined. Ceramics for which samples of different thickness were investigated include aluminum oxide, aluminum nitride, silicon nitride, titanium diboride and boron carbide. Relevant experimental parameters for the data examined are provided in Table 10.1.

Table 10.1:
Properties for Shock-Wave Experiments on Ceramics

Test Number	Material	Density (kg/m^3)	C_l (km/s)	C_s (km/s)	Impact Velocity (km/s)	Sample* Thickness (mm)
AO-03	Al_2O_3	3890	10.56	6.24	1.55	2.48
AO-01	Al_2O_3	3890	10.56	6.24	1.57	4.76
CE-58	Al_2O_3	3890	10.56	6.24	1.57	10.01
CE-43	AlN	3250	10.73	6.32	2.21	2.51
CE-52	AlN	3250	10.73	6.32	2.22	4.18
CE-37	AlN	3250	10.73	6.32	2.24	9.57
CE-101	B_4C	2506	14.07	8.87	3.98	2.99
CE-26	B_4C	2506	14.07	8.87	2.06	9.68
CE-104	Si_3N_4	3130	10.30	5.80	1.05	5.01
SN-02	Si_3N_4	3130	10.30	5.80	1.06	10.02
SN-01	Si_3N_4	3130	10.30	5.80	1.05	15.01
CE-10	TiB_2	4509	10.79	7.43	1.50	5.01
CE-9	TiB_2	4509	10.79	7.43	1.50	10.10
* All tests were ceramic-on-ceramic impacts.						

We first display the measured precursor profiles. (It is noted that there can be an illusory indication of precursor attenuation because of the different wave velocities associated with the precursor wave and following shock wave, and consequently the increasing difference in wave separation with propagation distance.) Precursor waves are then plotted in a manner which scales with propagation distance and examined for self similarity. This method is believed to be the best technique for revealing precursor decay and rate-dependent behavior in the yield process under dynamic uniaxial strain loading. It is concluded that with the exception of boron carbide there is no evidence for elastic precursor decay or rate-dependent yield in the ceramics investigated.

aluminum oxide

Precursor wave profiles for aluminum oxide measured over propagation thicknesses of approximately 2.5, 5.0 and 10.0 mm are shown in Figure 10.1. In (a) measured profiles are shown with the precursor arrival aligned to time zero. In (b) the same profiles are scaled to 10 mm sample thickness by multiplying every time datum by the ratio of 10 mm to sample thickness. The aluminum oxide on which this data was obtained was the Coors Porcelain Company AD-995 (CAP-3) product. The density and elastic properties are provided in Table 10.1.

The precursor profiles for this aluminum oxide are typical of most of the monolithic ceramics tested previously [Grady, 1992a; Grady, 1992b]. There is an initial sharp rise to a velocity level of a few hundred meters per second which is usually not resolved within the resolution of the VISAR system (~2-5 ns). This initial rise is followed by a more gradual ramping rise which merges into a steeper second wave. The second wave is readily resolved with the VISAR diagnostics provided the final shock amplitude is not excessively high. (The second wave rise time steepens with shock amplitude and ultimately also exceeds the resolution limits of the VISAR system.)

The initial sharp rise and more gradual ramping region is identified as the precursor wave or elastic precursor, whereas the second steeper wave is identified as the deformation shock, although a clear transition from one to the other is not always observed. Figure 2.4 and the associated discussion should be considered here.

From examination of the measured wave profiles in (a) of Figure 10.1 it is difficult to conclude with certainty whether or not the amplitude of the precursor wave is decreasing with propagation distance. The scaled plot of the data shown in (b), however, clearly shows self similarity in the amplitude of the initial rise and the shape of the ramping region. This observation suggest no precursor attenuation or rate independent yield and initial post-yield behavior in the present ceramic.

A closer examination of the profiles in Figure 10.1(b) shows the ramp region of the 10 mm sample about 5% lower than the 2.5 mm and 5.0 mm samples. Our experience over a broader range of tests is that this is within the sample to sample scatter associated with these wave profiles measurements. It should be noted, however, that the 10 mm sample was prepared from an earlier supply of the AD-995 (CAP-3) aluminum oxide than that of the 2.5 and 5.0 mm samples.
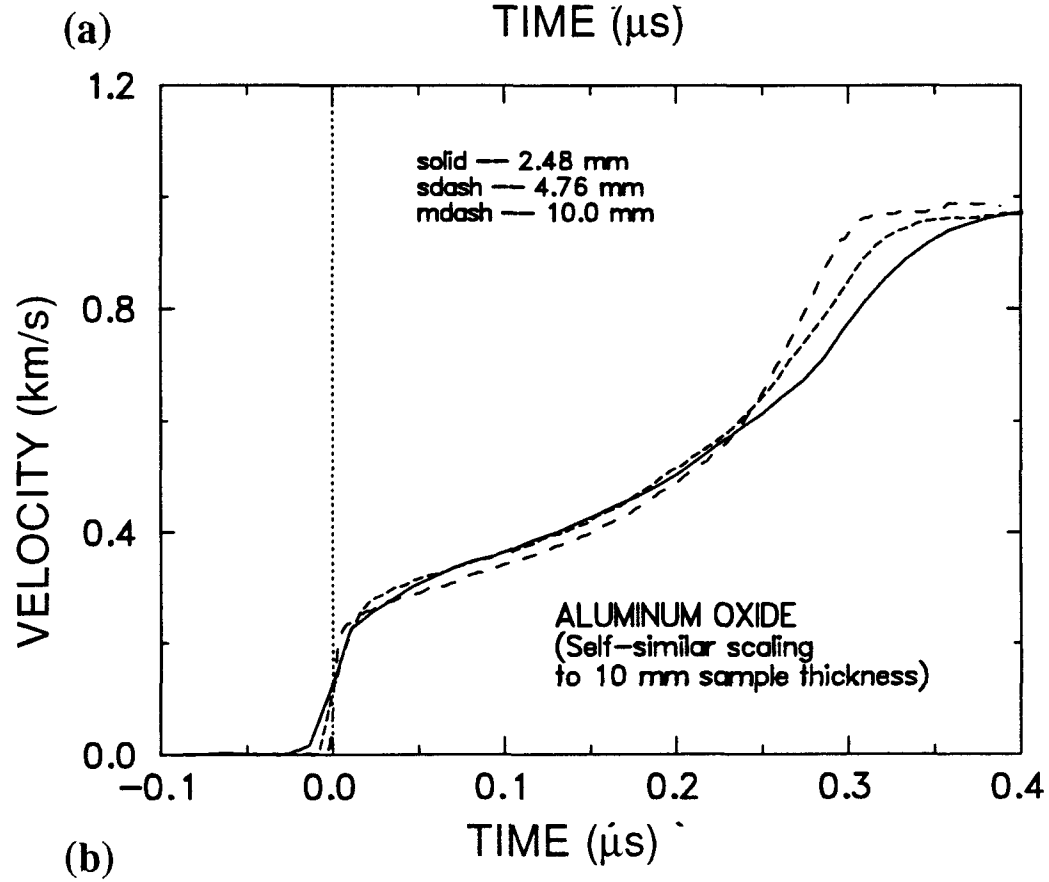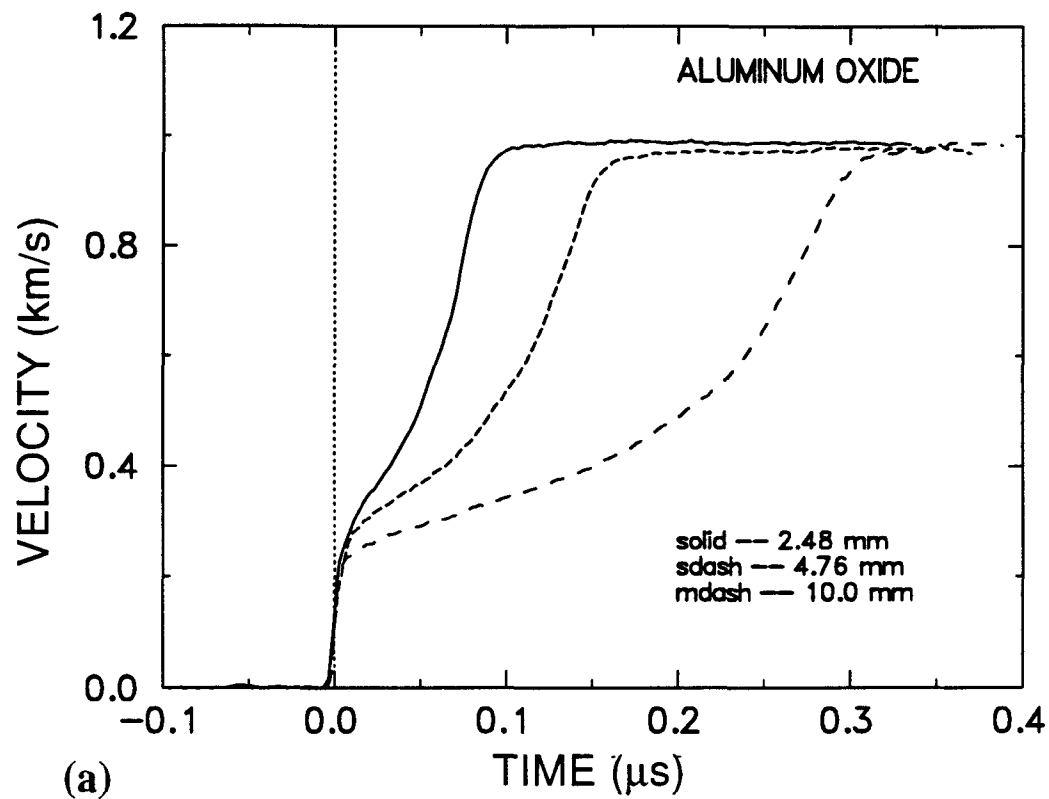
Figure 10.1 Velocity profiles for aluminum oxide. (a) Measured wave profiles.
(b) Self-similar representation of wave profiles.

A further interesting observation in the aluminum oxide profiles is the lack of self similarity of the deformation shock waves. That is in the self-similar plot the deformation shock for the 10 mm test arrives earlier in time than the 5 mm test which in turn proceeds the 2.5 mm test. This implies that shock velocities calculated from the 10 mm test will be higher than shock velocities from the 5 mm or 2.5 mm test. The maximum difference in the present tests is about 3%. This effect is not understood, but one possible explanation is an increased precursor amplitude (and hence precursor attenuation) for very early propagation distances (< 2.5 mm) which would lead to decreased shock velocities within this region.

aluminum nitride
Similar profiles of the precursor wave for aluminum nitride are provided in Figure 10.2(a) and (b). These are the same wave profiles discussed in Section 7 and by Kipp and Grady (1994) where emphasis was on the ~20 GPa shock-induced phase transition. This transition initiates at the top of the second wave shown in Figure 10.2. The aluminum nitride ceramic tested was provided by DOW Chemical Company. The material was near theoretical density although sample-to-sample variations in density and sound speed of about 2% suggested a marked lack of homogeneity.

Like aluminum oxide, the precursor wave is characterized by a sharp rise to an initial yield level followed by a slowly rising ramp. The slope of the ramp is more gradual than that of aluminum oxide and the transition to the second shock is more definitive. Although there is some scatter in the sample-to-sample profile structure, the self similarity in the scaled profiles in Figure 10.2(b) clearly suggests negligible precursor decay and negligible rate dependence in the initial yield and post-yield behavior of aluminum nitride.

The nearly self similar behavior of the second wave in the scaled plot is curious. If it is presumed that this is a steady shock segment over a region of positive stress-strain curvature then self-similar wave profile structure is not expected. Considering scatter in the data this may be fortuitous, however, and further testing would be needed to confirm the observation.

silicon nitride
Precursor profiles for silicon nitride measured at sample thicknesses of 5, 10 and 15 mm are shown in Figure 10.3 (a) and (b). This material is the near theoretical density SN-220 ceramic provided by Kyocera Industrial Ceramics Corporation. Maximum shock amplitude in these tests was somewhat lower than those achieved in the aluminum oxide and aluminum nitride experiments. Consequently, the second shock wave observed in Figure 10.3 is just beginning to develop and has the characteristic large rise time of relatively low amplitude shock waves.

The self similarity of the scaled wave profiles in Figure 10.3(b) is quite remarkable and again provides absolutely no evidence for precursor decay with propagation distance. As in the case of the aluminum nitride, the self similar behavior of the second shock for the silicon nitride, even though just beginning to develop, indicates that it is still evolving over the propagation distance and has not achieved a steady-wave rise time. This assumes,
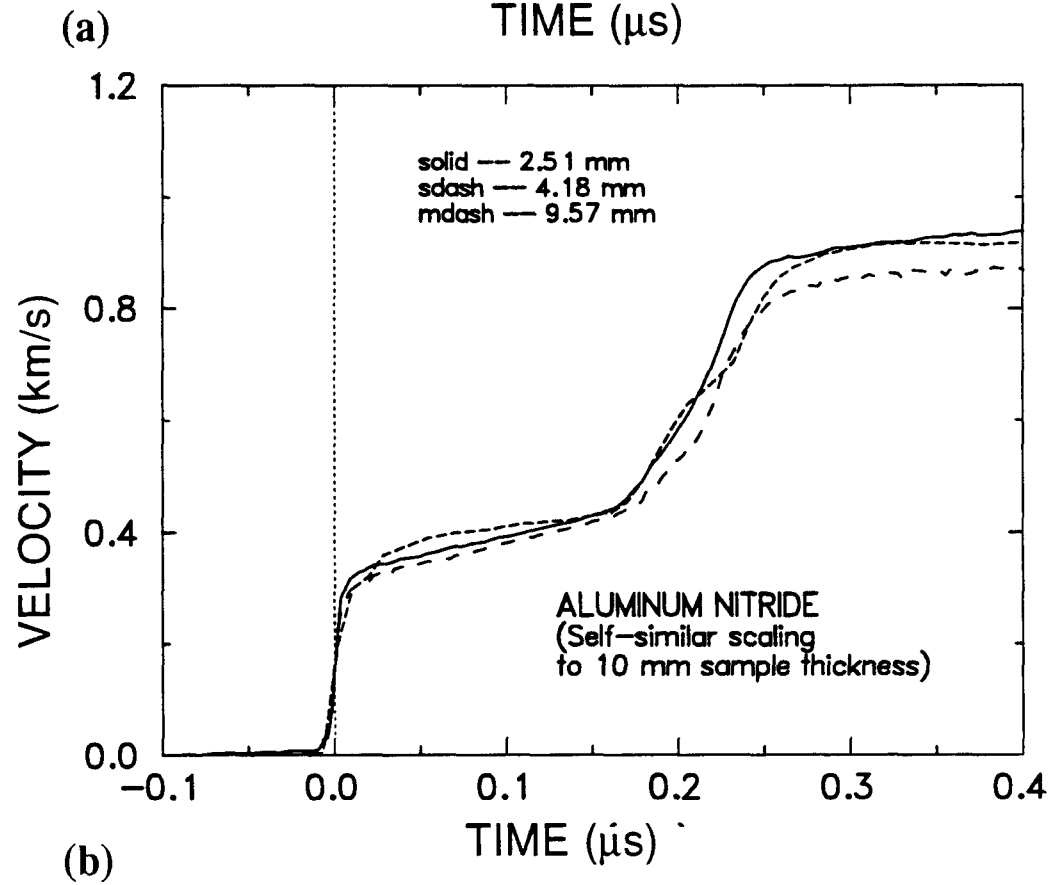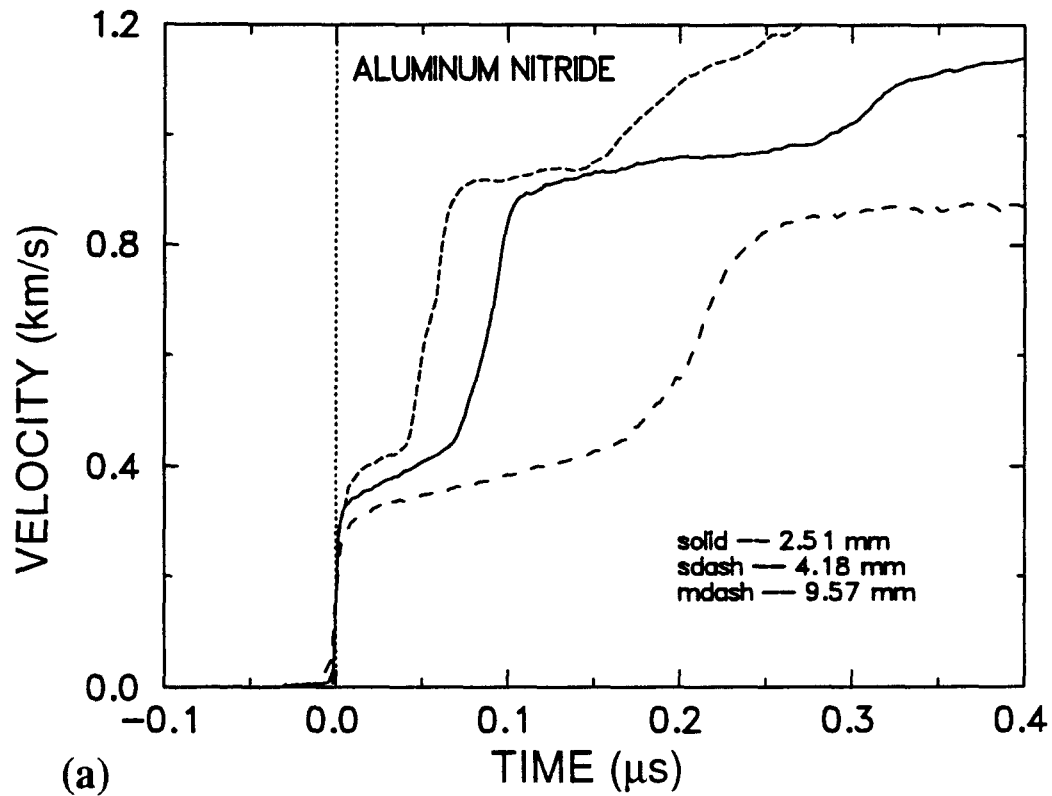
Figure 10.2 Velocity profiles for aluminum nitride. (a) Measured wave profiles.
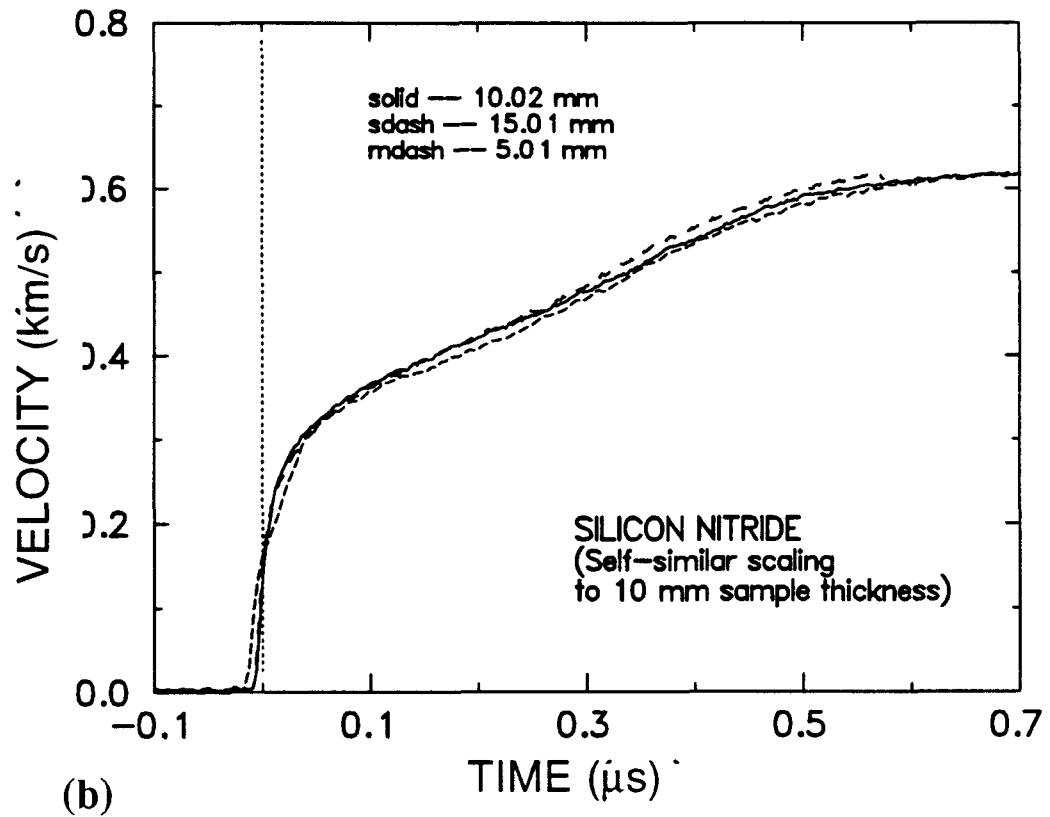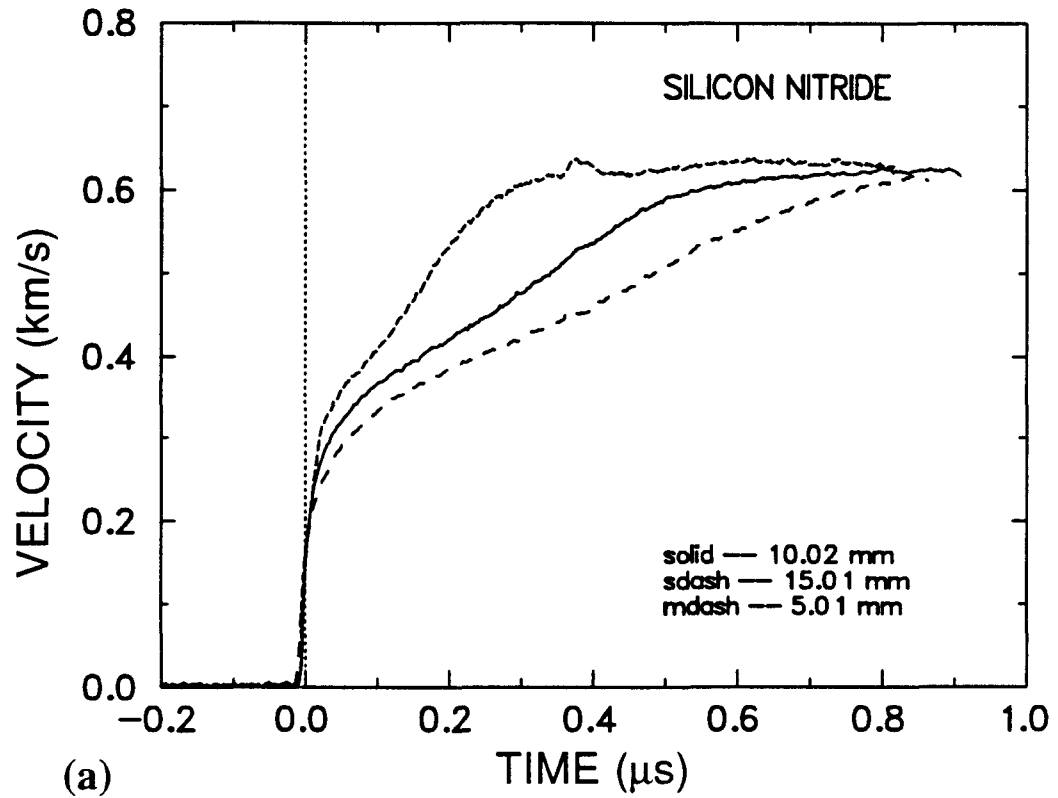(b) Self-similar representation of wave profiles.

Figure 10.3 Velocity profiles for silicon nitride. (a) Measured wave profiles.
(b) Self-similar representation of wave profiles.

of course, that this segment of the wave is evolving toward a steady-wave configuration. More complex constitutive features are quite possible.

titanium diboride

Only two shock-compression experiments on titanium diboride illustrating wave evolution features as a function of propagation distance have been performed. They are nonetheless interesting and are shown in Figure 10.4 (a) and (b). The material is a near full density ceramic prepared by CERCOM Inc.

Titanium diboride ceramic is unique in exhibiting a more complex two wave structure associated with the dynamic yield process although the possibility of a polymorphic phase transformation within this range contributing to the unusual structure has not yet been ruled out [Grady and Wise, 1993].

The scaled profiles illustrated in Figure 10.4(b) indicate some deviation from self similarity although the sample-to-sample scatter in profile structure is uncertain. Both the elastic wave (up to initial yield) and the second shock wave have comparable rise times in the 5 mm and 10 mm samples, indicating quasi-steady behavior. The third wave appears to still be evolving with propagation distance. Neither the first or second yield, as indicated by the cusps in Figure 10.4, show signs of amplitude decay with distance.

boron carbide

Precursor waves observed in the previous ceramics have features in common. A rapidly rising wave front rounds over to a more gentle, but still rising, ramp region which merges in turn into the following deformation shock wave. Precursor waves for boron carbide are unique among the ceramics tested in exhibiting markedly different profile structure. Representative precursor profiles are shown in Figure 10.5. A discontinuous wave front (within the several ns resolution of the VISAR diagnostics) is followed by a somewhat ragged but nonetheless falling ramp region before arrival of the deformation shock wave which transports material to the final shock state.

Precursor waves in boron carbide have been compared in detail with corresponding waves in silicon carbide in Section 6 and also in Grady (1994). Briefly it was suggested that the velocity (and stress) relaxation within the precursor ramp is indicative of a material exhibiting rate-dependent loss of strength in the shock-induced yield process. Further, irregularities in the measured profile may be associated with a heterogeneous yield process on a spacial scale which caused superimposed chaotic motion at the interferometer spot where velocity is measured.

Within the scope of the present examination of precursor wave attenuation, only one experiment (CE-101) on a reduced thickness sample of boron carbide has been performed. These tentative results, however, do indicate a measurable precursor decay with propagation distance. (A 20 GPa Hugoniot elastic limit at a 3 mm sample thickness attenuates to about 16.4 GPa at approximately 10 mm.) Thus boron carbide is also unique among the ceramics examined here in being the only material which may exhibit measurable elastic precursor attenuation within the range of the present data and does not exhibit self-similar scaling of the precursor wave.
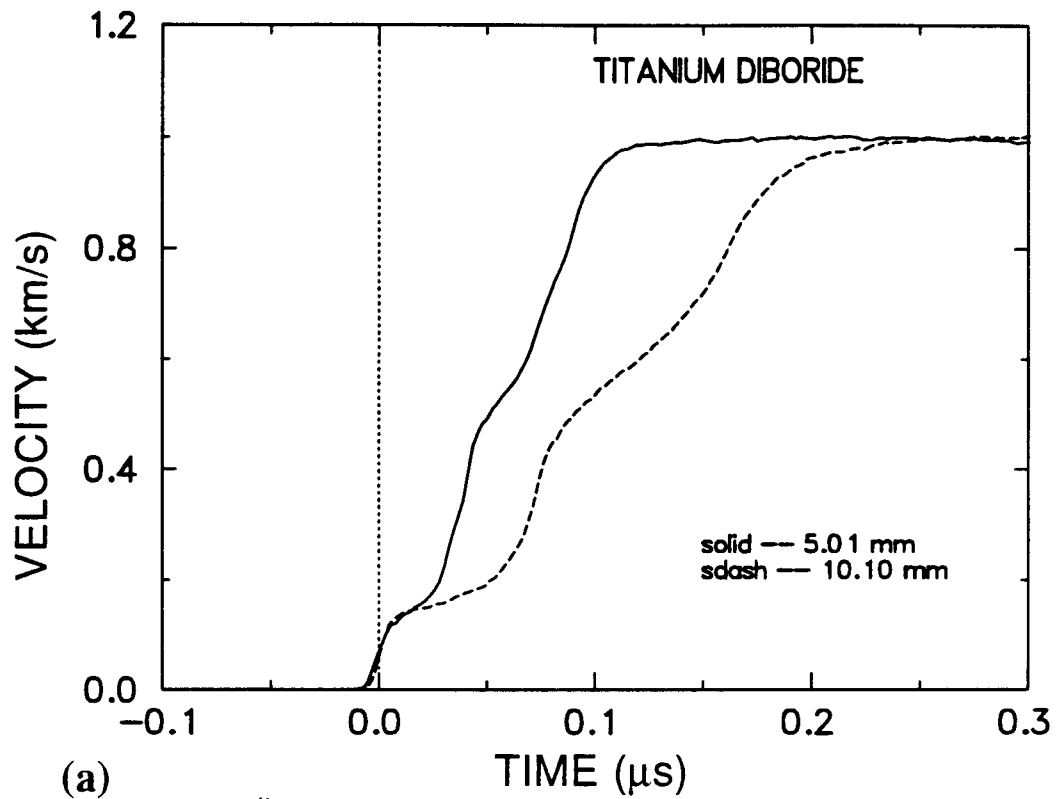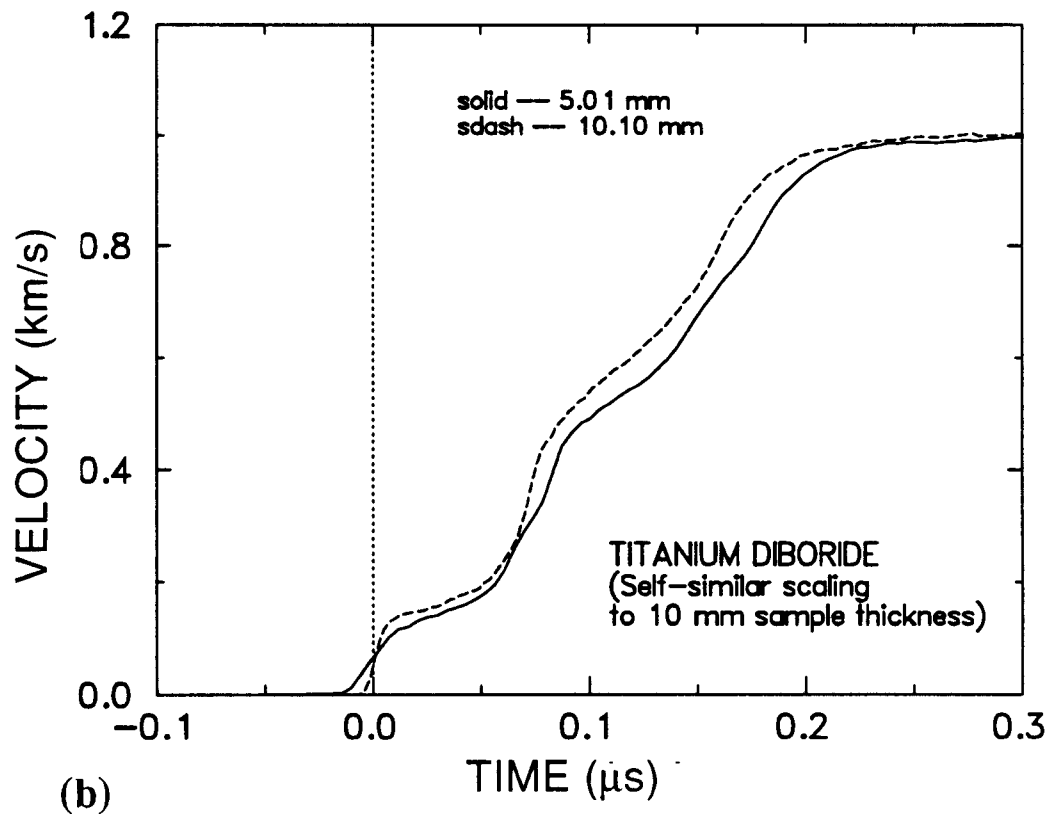
Figure 10.4 Velocity profiles for titanium diboride. (a) Measured wave profiles. (b) Self-similar representation of wave profiles.

10.3 Hugoniot Elastic Limit Data

We have attempted to provide a representation of the Hugoniot elastic limit (HEL) data implied by the present VISAR wave-profile measurements on ceramic specimens of various sample thicknesses. The results, which are tabulated in Table 10.2 and plotted in Figure 10.6, require further discussion.

With the high amplitude and temporal resolution provided by the velocity interferometer profile measurements, the selection of a precursor amplitude with which to correlated with a specific HEL amplitude is no longer obvious. Examination of the data in the previous plots for aluminum oxide, or silicon nitride, for example, reveals a gradual rounding and ramping which makes it difficult to systematically associate a specific amplitude with the HEL amplitude. Recent computational simulations of profiles measured on tungsten carbide, which reveals similar precursor structure, demonstrated that an initial 4 GPa breakover stress can achieve 8 to 9 GPa through the precursor ramp region before merging into the deformation shock wave (Section 8).

In this study we have used the following tactic to systematically establish an HEL precursor amplitude for each profile measurement. A characteristic time τ_d associated with the
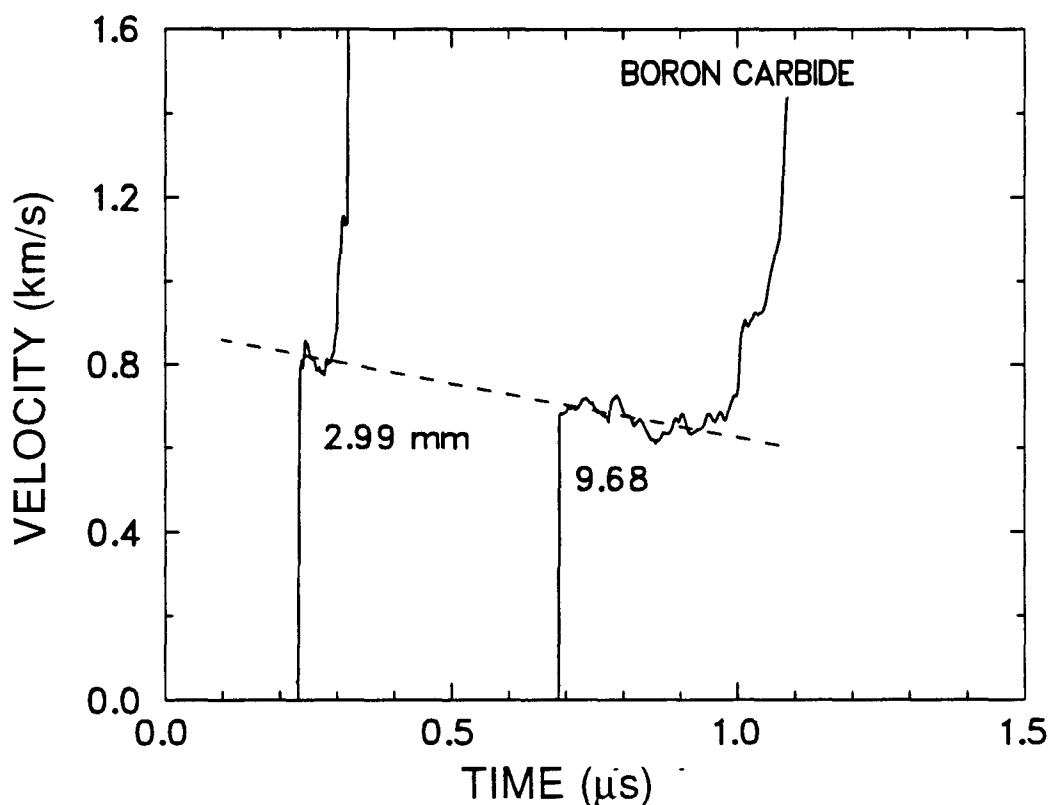

Figure 10.5 Precursor velocity profiles for boron carbide at two sample thicknesses indicating precursor attenuation.

separation of the arrival of the precursor wave and the deformation shock wave at the recording interface is established from the profile. Although some arbitrariness is introduced by the finite rise of the respective waves (primarily the deformation shock), reasonable consistency is relatively easy to achieve. The velocity amplitude, u_e, at the temporal midpoint ($\tau_d/2$) is then accepted as the HEL amplitude. This method is expected to provide comparable HEL amplitudes with lower resolution wave-profile measurement techniques (piezoresistive stress gages, magneto-inductive velocity gages) where details of the precursor structure are frequently not resolved. The HEL stress, reported for the present data in Table 10.2, was then calculated from the u_e data assuming longitudinal acoustical impedance properties for the ceramic and hydrodynamic acoustical properties for the lithium fluoride, respectively. To display the dependence of the HEL stress on sample thickness for the present data we have chosen to establish an effective strain rate corresponding to the dynamic strength measurement. Although loading to the HEL stress is not a constant strain rate process in a shock wave experiment, the time τ_d separating elastic and deformation shocks provides a time scale over which the precursor amplitude is established. Consequently, the ratio of the HEL strain, $\varepsilon_{hel} = \sigma_{hel}/\rho_o c_L^2$, to the appropriate characteristic time τ_d, provides an effective strain rate, $\dot{\varepsilon}_{eff} = \varepsilon_{hel}/\tau_d$, which is also reported in Table 10.2.

Table 10.2:
Hugoniot Elastic Limit Data for Ceramics

Test Number	Material	τ_d (ns)	u_e (m/s)	Strain Rate (10^5/s)	HEL* (GPa)
AO-03	Al_2O_3	68	405	3.8	11.1
AO-01	Al_2O_3	122	395	2.0	10.8
CE-58	Al_2O_3	255	388	0.9	10.6
CE-43	AlN	55	402	4.7	9.75
CE-52	AlN	90	398	2.9	9.65
CE-37	AlN	210	395	1.2	9.58
CE-101	B_4C	80	820	5.1	20.0
CE-26	B_4C	400	670	0.8	16.4
CE-104	Si_3N_4	175	400	1.6	9.16
SN-02	Si_3N_4	345	408	0.8	9.34
SN-01	Si_3N_4	490	402	0.6	9.21
CE-10	TiB_2	38	156	2.4	4.86
CE-9	TiB_2	72	169	1.4	5.26
* Hugoniot elastic limit — see text.					
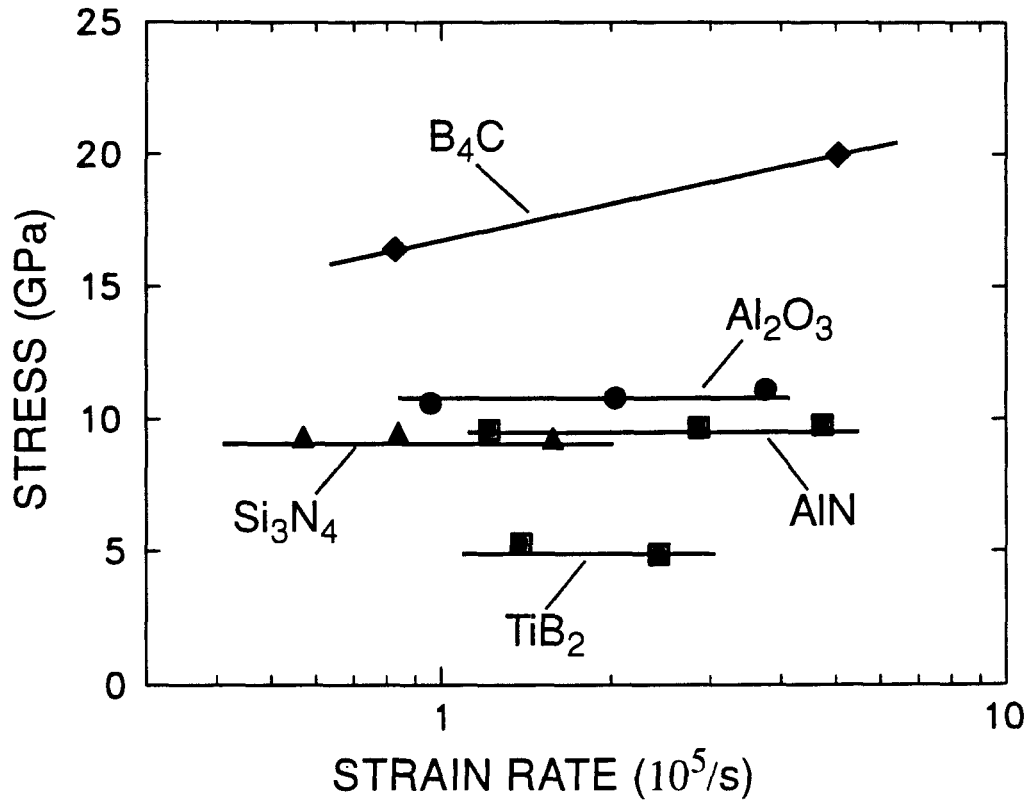
Figure 10.6 Hugoniot elastic limit versus strain rate date inferred from VISAR wave profile data for selected ceramics.

The corresponding HEL stress and strain rate data are plotted in Figure 10.6. Consistent with the earlier examination of the data in the previous section, with the exception of boron carbide, there is little evidence to indicate HEL precursor decay over the approximately half a decade of strain rate inferred from the profile measurements.

10.4 Discussion

' The present survey of compression profiles measured on selected ceramics indicates, for the most part, very little evidence to support the existence of elastic precursor wave attenuation in ceramics. Precursor attenuation is expected to be a natural consequence of the rate sensitive dynamic strength characteristics of solids.

The present investigation, however, has only examined the issues of precursor attenuation within the limited sample thickness range of a few millimeters to a few tens of millimeters. Corresponding effective strain rates are about 5×10^4/s to 5×10^5/s. Rate sensitivities outside of this range, or rate sensitivities within this range of as much as 5% per decade, cannot be commented on.

This notable lack of precursor attenuation and rate sensitivity in ceramics is surprising. Compressive failure in the shock process is believed to be a fracture-controlled mechanism and the nucleation and growth of fracture is known to be a time-dependent process. Such time dependence would be expected to lead to rate-dependent strength and precursor decay in ceramics. Fracture failure in brittle materials under other modes of deformation (spall [Grady, 1980], compression bar [Lankford, 1981]) have shown strength sensitivities on strain rate approaching a one-third power behavior. The model of compressive fracture leading to Equation 30 in Section 5 predicts a one-third power dependence of the Hugoniot elastic limit on strain rate. The present insensitivity to strain rate raises the question of whether failure within the front of a compressive shock wave is indeed a fracture controlled process.

The present results are consistent with the conclusions of Cagnoux and Longy (1987). From their observations of negligible precursor decay in alumina, they concluded that grain plasticity was a more likely mechanism for yield in the compressive shock front than was brittle fracture.

11 Conclusions

Substantial experimental research, both here and in other institutions, on the dynamic response of ceramics has been performed over the past several years. Results of these studies are providing a sound experimental base for the development and validation of computational models focused on the dynamic behavior of brittle materials.

Over the time frame of those experimental research efforts, however, there does not appeared to have been a commensurate improvement in the communities understanding of the mechanisms underlying the transient failure and deformation of brittle solids. Very recently benefits from the several years of research effort are beginning to be realized. Concepts such as failure waves, high-confinement dilatancy, brittle-ductile (deformation stability) transitions and granular flow, although not new, are emerging as very real features to address in the constitutive modeling of ceramics. These issues can be expected to drive the direction of experimental research and modeling over the next several years.

12   References

Section 1

Grady, D. E., *Dynamic Failure in Brittle Solids*, in Proceedings Europe-U.S. Workshop on Fracture and Damage in Quasibrittle Structures: Experiment, Modeling and Computer Analysis, Prague, Czech Republic, September 21-23 (1994a).

Grady, D. E.. *Shock-Wave Strength Properties of Boron Carbide and Silicon Carbide.* in Proceedings of EuroDYMAT 94 - International Conference of Mechanical and Physical Behavior of Materials under Dynamic Loading, Oxford England, September 26-30, (1994b).

Grady, D. E. and J. L. Wise, *Dynamic Properties of Ceramic Materials*, Sandia National Laboratories Report, SAND93-0610, September (1993).

Grady, D. E. and Yu. N. Zhugin, C*ritical Transition Stress in the Shock Compression of SiO$_2$ (abstract only)*, Bull. Am. Phys. Soc., 39, 410-411 (1994)

Kipp, M. E. and D. E. Grady, *Shock Phase Transformation and Release Properties of Aluminum Nitride*, in Proceedings of EuroDYMAT 94 - International Conference of Mechanical and Physical Behavior of Materials under Dynamic Loading, Oxford England, September 26-30 (1994).

Zhugin, Yu. N. and K. K. Krupnikov,, *Structural Peculiarities of Plastic Wave Front in Quartz in the Mixed Phase Region, in, Non-Linear Acoustics Problems*, in Transactions of the XI International (IUPAP-IUTAM) Symposium on Non-Linear Acoustics, Part II, Novosibirsk, 196-200 (1987).

Section 2

Barker, L. M. and R. E. Hollenbach, *Laser Interferometer for Measuring High Velocities of any Reflecting Surface*, J. Appl. Phys., 43, 4669-4680 (1992).

Grady, D. E, *Shock Deformation of Brittle Solids*, J. Geophys. Res., 85, 913-924 (1980).

Grady, D. E., *Local Inertial Effects in Dynamic Fragmentation*, J. Appl. Phys., 53, 322-325 (1982).

Grady, D. E., *The Spall Strength of Condensed Matter*, J. Mech. Phys. Solids, 36, 353-383 (1988).

Grady, D. E., *Shock-Wave Properties of High-strength Ceramics*, in Shock Compression of Condensed Matter - 1991, S. C. Schmidt, R. D. Dick, J. W. Forbes and D. G. Tasker, eds. Elsevier Science Publishing, 455-458 (1992a).

Grady, D. E., *Shock-Compression Properties of Ceramics.* in Recent Trends in High-Pressure Research, A. K. Singh, ed., Oxford and IBH Publishing, 641-650 (1992b).

Grady, D. E., *Shock-Wave Strength Properties of Boron Carbide and Silicon Carbide*, in Proceedings of EuroDYMAT 94 - International Conference of Mechanical and Physical Behavior of Materials under Dynamic Loading, Oxford England, September 26-30 (1994).

Sato, T. and S. Akimoto, *Hydrostatic Compression of Four Corundum-Type Compounds*, J. Appl. Phys. 50, 5285-5291 (1979).

Wise, J. L. and L. C. Chhabildas, *Laser Interferometer Measurements of Refractive Index in Shock-Compressed Materials*, in Shock Waves in Condensed Matter - 1985, Y. M. Gupta, ed., Plenum Press, 441-445 (1985).

Section 3

Brar, N. S., S. J. Bless and Z. Rosenberg, *Impact-Induced Failure Waves in Glass Bars and Plates*, Appl. Phys. Lett., 59, 3396-3398, (1991).

Kanel, G. I., S. V. Rasorenov and V. E. Fortov, *The Failure Waves and Spallations in Homogeneous Brittle Materials*, in Shock Compression of Condensed Matter - 1991, S. C. Schmidt, R. D. Dick, J. W. Forbes and D. G. Tasker, eds., Elsevier Science Publishing, 451-454, 1992.

Raiser, G. V., J. L. Wise, R. J. Clifton, D. E. Grady and D. E. Cox. *Plate Impact Response of Ceramics and Glasses*, J. Appl. Phys., 75, 3862-3872 (1994).

Raiser, G. V. and R. J. Clifton. *Failure Waves in Uniaxial Compression of an aluminosilicate Glass*, in High Pressure Science and Technology — 1993, S. C. Schmidt, J. W. Shaner, G. A. Samara, M. Ross, eds., AIP Press, 1039-1042 (1994).

Section 4

Grady, D. E., *The Mechanics of Fracture under High-Rate Stress Loading*, in Mechanics of Geomaterials, Z. Bazant, ed., John Wiley and Sons, 129-156 (1985).

Grady, D. E., *The Spall Strength of Condensed Matter*, J. Mech. Phys. Solids, 36, 353-383 (1988).

Grady, D. E. and M. E. Kipp, *Fragmentation of Solids under Dynamic Loading*, in Structural Failure, T. Wurzbicki, ed., John Wiley and Sons, 1-39 (1989).

Grady, D. E. and M. E. Kipp, *Dynamic Fracture and Fragmentation,* in High-Pressure Shock Compression of Solids, J. R. Asay and M. Shahinpoor, eds., Springer-Verlag, 265-319 (1993).

Izotov, A. D. and V. B. Lazarev, *Theoretical Strength of Ceramic Materials*, Inorg. Mater., 21, 612-617 (1985).

Kipp, M. E., D. E. Grady and E. P. Chen, *Strain-Rate Dependent Fracture Initiation*, Int. J. Fracture, 16, 471-478 (1980).

Kozhusko, A. A., I. I. Rykova, A. D. Izotov and V. B. Lazarev, *Strength and Fracture of Ceramic Materials*, in High-Velocity Deformation. Inorg. Mater., 23, 1820-1824 (1987).

Lawn, B. R. and T. R. Wilshaw, *Fracture of Brittle Solids*, Cambridge University Press, (1975).

Section 5

Curran, D. R., L. Seaman and D. A. Shockey, *Dynamic Failure of Solids*, Physics Reports, 147, 253-388 (1987).

Curran, D. R., L. Seaman, T. Cooper and D. A. Shockey, *Micromechanical Model for Comminution and Granular Flow of Brittle Materials under High Strain Rate Application to Penetration of Ceramic Targets*, Int. J. Impact Eng., 13, 53-84 (1993).

Griffith., A. A., *Theory of Rupture*, Proceedings First International Congress Applied Mechanics, Delft, 55-63 (1924).

Janach, W., *Failure of Granite under Compression*, Int. J. Rock Mech. Min. Sci., 14, 209-215 (1977).

Johnson, G. R. and T. J. Holmquist, *Improved Computational Constitutive Model for Brittle Materials*, in High Pressure Science and Technology — 1993, S. C. Schmidt, J. W. Shaner, G. A. Samara, M. Ross, eds., AIP Press, 981-984 (1994).

Murrel, S. A. F., *A Criterion for Brittle Fracture of Rocks and Concrete under Triaxial Stress and the Effect of Pore Pressure on the Criterion*, in Rock Mechanics, C. Fairhurst, ed., Oxford, Pergamon, 563-577 (1963).

Rosenberg, Z., *On the Relation Between the Hugoniot Elastic Limit and the Yield Strength of Brittle Materials*, J. Appl. Phys., 74, 752-753 (1993).

Steinberg, D. J., *Computer Studies of the Dynamic Strength of Ceramics*, in 3rd International Conference on Mechanical and Physical Behavior of Materials under Dynamic Loading, les Editions des Physique, 837-844 (1991).

Section 6

Atroshenko S. A., Vasil'kov V. B., Meshcherykov Yu. I., Savenkov G. G. and Chernyshenko A. I., *High-Frequency Vibration of Grains Excited by Pulsed Loading*, Sov. Phys. Tech. Phys., 35, 336-341 (1990).

Barker, L. M. and R. E. Hollenbach, *Laser Interferometer for Measuring High Velocities of any Reflecting Surface*, J. Appl. Phys., 43, 4669-4680 (1972).

Grady, D. E., *Shock Deformation of Brittle Solids*, J. Geophys. Res., 85, 913-924 (1980).

Grady, D. E., *Shock-Wave Properties of High-strength Ceramics*, in Shock Compression of Condensed Matter - 1991, S. C. Schmidt, R. D. Dick, J. W. Forbes and D. G. Tasker, eds. Elsevier Science Publishing, 455-458 (1992a).

Grady, D. E., *Shock-Compression Properties of Ceramics*, in Recent Trends in High-Pressure Research, A. K. Singh, ed., Oxford and IBH Publishing, 641-650 (1992b).

Grady, D. E., and M. E. Kipp, *Shock Compression Properties of Silicon Carbide*, Sandia National Laboratories Report, SAND92-1832, July (1993).

Grady, D. E., *Impact Strength and Indentation Hardness of High-Strength Ceramics*, in High Pressure Science and Technology — 1993, S. C. Schmidt, J. W. Shaner, G. A. Samara, M. Ross, eds., AIP Press, 741-744 (1994).

Emin D., *Icosahedral Boron-Rich Solids*, Physics Today, 1, 1-8 (1987).

Kipp, M. E. and D. E. Grady, *Shock Compression and Release in High-Strength Ceramics*, Sandia National Laboratories Report, SAND89-1461, July (1989).

Kipp, M. E. and D. E. Grady, *Elastic Wave Dispersion in High-Strength Ceramics*, in Shock Compression of Condensed Matter - 1991, S. C. Schmidt, R. D. Dick, J. W. Forbes and D. G. Tasker, eds., Elsevier Science Publishing, 459-462 (1992).

Manghnani, M. H, *Elastic Properties and Compressibility of Advanced Ceramic Composites*, J. Appl. Phys., to be submitted (1994).

Meshcheryakov, Yu. I., S. A. Atroshenko, V. B. Vasil'kov and A. I. Chernyshenko, *Criteria of Transition from Translational to Rotational Motion of Media under Shock Loading*, in Shock Compression of Condensed Matter - 1991, S. C. Schmidt, R. D. Dick, J. W. Forbes and D. G. Tasker, eds., Elsevier Science Publishing, 407-410 (1992).

Section 7

Brar, N. S., S. J. Bless, and Z. Rosenberg, *Response of Shock-Loaded AlN Ceramics Determined with In-Material Manganin Gauges*, in Shock-Wave and High-Strain-Rate Phenomena in Materials, M. A. Meyers, *et al.* eds., Marcel Dekker, Inc., 1023-1030 (1992).

Chhabildas, L. C., J. R. Asay, and L. M. Barker, *Shear Strength of Tungsten Under Shock- and Quasi-Isentropic Loading to 250 GPa*, Sandia National Laboratories Report, SAND88-0306, April (1988).

Chhabildas, L. C. and J. R. Asay, *Dynamic Yield Strength and Spall Strength Measurements Under Quasi-Isentropic Loading*, Shock-Wave and High-Strain-Rate Phenomena in Materials, M. A. Meyers, L. E. Murr and K. P. Staudhammer, eds., Marcel Dekker, Inc., 947-955 (1992).

Dandekar, D. P., A. Abbate and J. Frankel, *Equation of aluminum Nitride and its Shock Response*, J. Appl. Phys., 76, 4077-4085 (1994).

Gerlich, D., S. L. Dole, and G. A. Slack, *Elastic Properties of Aluminum Nitride*, J. Phys. Chem. Solids, 47, 437-441 (1986).

Grady, D. E., *Shock-Compression Properties of Ceramics*. in Recent Trends in High-Pressure Research, A. K. Singh, ed., Oxford and IBH Publishing, 641-650 (1992b).

Jeanloz, R., *Shock Wave Equation of State and Finite Strain Theory*, Journal of Geophysical Research, 94, 5873-5886 (1989).

Kipp, M. E. and R. J. Lawrence, *WONDY V - A One-Dimensional Finite-Difference Wave Propagation Code*, Sandia National Laboratories Report, SAND81-0930, June (1982).

Kipp, M. E. and D. E. Grady, *Shock Compression and Release in High-Strength Ceramics*, in Shock Compression of Condensed Matter - 1989, S. C. Schmidt, J. N. Johnson and L. W. Davison, eds., North-Holland, Amsterdam, 377-380 (1990).

Kondo, K., A. Sawaoka, K. Sato and M. Ando, *Shock Compression and Phase Transformation of AlN and BP*, AIP Conference Proceedings No. 78, Shock Waves in Condensed Matter - 1981 (Menlo Park), W. J. Nellis, L. Seaman, and R. A. Graham, eds., AIP Press, 303-305 (1982).

Nakamura, A. and T. Mashimo, *Shock-Induced Phase Transition of AlN*, in High Pressure Science and Technology — 1993, S. C. Schmidt, J. W. Shaner, G. A. Samara, M. Ross, eds., AIP Press, 981-984 (1994).

Van Camp, P. E., V. E. Van Doren and J. T. Devreese J. T., *Theoretical High Pressure Studies of the Binary Nitrides*, in Recent Trends in High-Pressure Research, A. K. Singh, ed., Oxford and IBH Publishing, *322-327*, (1992).

Vollstädt, H., E. Ito, M. Akaishi, S. Akimoto, and O. Fukunaga, *High Pressure Synthesis of Rocksalt Type of AlN*, Proc. Japan Acad., 66 Ser. B, 7-9 (1990).

Wise, J. L. and L. C. Chhabildas, *Laser Interferometer Measurements of Refractive Index in Shock-Compressed Materials*, in Shock Waves in Condensed Matter - 1985, Y. M. Gupta, ed., Plenum Press, 441-445 (1985).

Section 8

Grady, D. E. and M. E. Kipp, *Dynamic Fracture and Fragmentation*, in High-Pressure Shock Compression of Solids, J. R. Asay and M. Shahinpoor, eds., Springer Verlag, 285-322 (1993).

Gust, W. H., *Hugoniot Elastic Limits and Compression Parameters for Brittle Materials*, in High Pressure Science and Technology, Vol. 2, B. Vodar and Ph. Marteau, eds., Pergamon Press, 1009-1016 (1980).

Holmquist, T. J., Unpublished. (1994).

Kipp, M. E. and R. J. Lawrence, *WONDY V - A One-Dimensional Finite-Difference Wave Propagation Code*, Sandia National Laboratories Report, SAND81-0930, July (1982).

Marsh, S. P., *LASL Shock Hugoniot Data*, S. P. Marsh, Ed., University of California Press, (1980).

McQueen, R. G., *The Equation of State of Mixtures, Alloys, and Compounds, in Seismic Coupling*, G. Simmons, Ed., Proceedings of a Meeting sponsored by the Advanced Research Projects Agency at Stanford Research Institute, Menlo Park, California, January 15-16, (1968).

McQueen, R. G., S. P. Marsh, J. W. Taylor, J. N. Fritz, W. J. Carter, *The Equation of State of Solids from Shock Wave Studies*, in High-Velocity Impact Phenomena, R. Kinslow, Ed., Academic Press, 293-417, 521-568 (1970).

Morris, C. E., *LASL Shock Wave Profile Data*, C. E. Morris, Ed., University of California Press, (1980).

Steinberg, D. J., *Equation of State and Strength Properties of Selected Materials*, Lawrence Livermore National Laboratories Report, UCRL-MA-106439, (1991).

Section 9

Barker, L. M. and R. E. Hollenbach, *Laser Interferometer for Measuring High Velocities of any Reflecting Surface*, J. Appl. Phys., 43, 4669-4680 (1992).

Chaplot, S. L. and S. K. Sikka, *Molecular Dynamics Simulations of Pressure Induced Crystal to Amorphous Transitions in Some Corner Linked Polyhedral Compounds*, in Recent Trends in High Pressure Physics, A. K. Singh, ed., Oxford and IBH publishing, 259-261 (1992).

Grady, D. E., W. J. Murri and G. R. Fowles, *Quartz to Stishovite: Wave Propagation in the Mixed Phase Region*, J. Geophys. Res., 79, 332-338 (1974).

Grady, D. E., W.J. Murri and P. S. DeCarli, *Hugoniot Sound Velocities and Phase Transformation in Two Silicates*, J. Geophys. Res., 80, 4857-4861 (1975).

Grady, D. E., *Shock Deformation of Brittle Solids*, J. Geophys. Res., 85, 913-924 (1980).

Grady, D. E. and Yu. N. Zhugin, *Critical Transition Stress in the Shock Compression of SiO_2 (abstract only)*, Bull. Am. Phys. Soc., 39, 410-411 (1994).

Hemley, R. J., A. P. Jephcoat, H. K. Mao, L. C. Ming, M. H. Manghnani, *Pressure-Induced Amorphization of Crystalline Silica*, Nature, 334, 52-54 (1988).

Sikka, S. K., *Pressure Induced Glasses*, in Recent Trends in High Pressure Physics, A. K. Singh, ed., Oxford and IBH publishing, 254-258 (1992).

Tse, J. S. and D. D. Klug, (1992), *High Pressure Phase Transitions in Silica and Berlinite by Molecular Dynamics Simulations*, in Recent Trends in High Pressure Physics, A. K. Singh, ed., Oxford and IBH publishing, 274-279 (1992).

Zhugin, Yu. N. and K. K. Krupnikov, *Structural Peculiarities of Plastic Wave Front in Quartz in the Mixed Phase Region*, in Transactions of the XI International (IUPAP-IUTAM) Symposium on Non-Linear Acoustics, Part II, Novosibirsk, 196-200 (1987).

Section 10

Ahrens, T. J. and G. E. Duvall, *Stress Relaxation Behind Elastic Shock Waves in Rocks*, J. Geophys. Res., 71, 4349-4360 (1966).

Asay, J. R., G. R. Fowles and Y. Gupta, *Determination of Material Relaxation Properties from Measurements on Decaying Elastic Shock Fronts*, J. Appl. Phys., 43, 744-746 (1972).

Cagnoux, J. and F. Longy, *Is the Dynamic Strength of Alumina Rate Dependent*, in Shock Compression of Condensed Matter - 1987, S. C. Schmidt and N. C. Holmes, eds. Elsevier, 293-296 (1987).

Duvall, G. E., *Maxwell-Like Relations in Condensed Materials. Decay of Shock Waves*, Iranian Journal Sci. Tech., 7, 57-69 (1978).

Grady, D. E., *Criteria for Impulsive Rock Fracture*, Geophys. Res. Letters, 7, 255-258 (1980)

Grady, D. E., *Shock-Wave Properties of High-Strength Ceramics*, in Shock Compression of Condensed Matter - 1991, S. C. Schmidt, R. D. Dick, J. W. Forbes and D. G. Tasker, eds. Elsevier Science Publishing, 455-458 (1992a).

Grady, D. E., *Shock-Compression Properties of Ceramics*. in Recent Trends in High-Pressure Research, A. K. Singh, ed., Oxford and IBH Publishing, 641-650 (1992b).

Grady, D. E. and J. L. Wise, *Dynamic Properties of Ceramic Materials*, Sandia National Laboratories Report, SAND93-0610, September (1993).

Grady, D. E., *Shock-Wave Strength Properties of Boron Carbide and Silicon Carbide*, in Proceedings of EuroDYMAT 94 - International Conference of Mechanical and Physical Behavior of Materials under Dynamic Loading, Oxford England, September 26-30 (1994).

Kipp, M. E. and D. E. Grady, *Shock Phase Transformation and Release Properties of Aluminum Nitride*, in Proceedings of EuroDYMAT 94 - International Conference of Mechanical and Physical Behavior of Materials under Dynamic Loading, Oxford England, September 26-30 (1994).

Lankford, J., *Mechanisms Responsible for Strain-Rate-Dependent Compressive Strength in Ceramic Materials*, J. Am. Ceram. Soc., 64, C33-C34 (1981).

Partom, Y., *Difficulties in Modeling the High Rate Viscoplastic Response of AD995 Alumina*, Institute of Advanced Technology Tech. Note, IAT.TN0035, April (1994).

Rosenberg, Z., N. S. Brar and S. J. Bless, *Elastic Precursor Decay in Ceramics as Determined with Manganin Stress Gauges*, in 2rd International Conference on Mechanical and Physical Behavior of Materials under Dynamic Loading, les Editions des Physique, 707-711 (1988).

Steinberg, D. J., *Computer Studies of the Dynamic Strength of Ceramics*. in 3rd International Conference on Mechanical and Physical Behavior of Materials under Dynamic Loading, les Editions des Physique, 837-844 (1991).

DISTRIBUTION:

INTERNAL

1400	E. H. Barsis
1404	J. A. Ang
1421	S. S. Dosanjh
1422	R. C. Allen
1423	E. F. Brickell
1424	A. L. Hale
1431	J. M. McGlaun
1431	E. S. Hertel
1431	J. S. Peery
1431	A. C. Robinson
1431	T. G. Trucano
1431	M. K. Wong
1432	P. Yarrington
1432	P. J. Chen
1432	H. E. Fang
1432	A. V. Farnsworth
1432	G. I. Kerley
1432	M. E. Kipp
1432	S. A. Silling
1432	P. A. Taylor
1433	P. L. Stanton
1433	J. A. Ang
1433	L. C. Chhabildas
1433	M. D. Furnish
1433	D. A. Crawford
1433	D. E. Grady (35)
1434	D. R. Martinez
1500	D. J. McCloskey
1511	J. S. Rottler
1512	A. C. Ratzel
1561	H. S. Morgan
1562	R. K. Thomas
1562	J. W. Swegle
2565	S. T. Montgomery
7141	Technical Library (5)
7151	Technical Publications
7613	Document Processing for DOE/OSTI (10)
8523-2	Central Technical Files
9121	W. Tucker
9121	J. Hickerson
9723	M. J. Forrestal

EXTERNAL

T. F. Adams
Los Alamos National Laboratory
MS F663
Los Alamos, NM 87545

T. J. Ahrens
Geophysics Division MS/252-21
California Institute of Technology
Pasadena, CA 91125

F. Allahdadi
Phillips Laboratory
PL/WSSD
Kirtland AFB, NM 87117-6008

M. L. Alme
102 Stevens Forrest Professional Center
9650 Santiago Road
Columbia, MD 21045

C. E. Anderson
Southwest Research Institute
6220 Culebra Road
San Antonio, TX 78284

J. A. Bailey
U.S. Army Research Office
P. O. Box 12211
Research Triangle Park, NC 27709

E. Baker
Army ARDE Center
SMCAR-AEE-WW
Picatinny Arsenal, NJ 07806-5000

P. Bartkowski
Army Research Laboratory
Materials Directorate
AMSRL-MA-PD
Watertown, MA 02172-0001

D. W. Baum
L-35
Lawrence Livermore National Laboratory
Livermore,CA 94550

P. Beaulieu
Army Research Laboratory
Materials Directorate
AMSRL-MA-PD
Watertown, MA 02172-0001

G. Bishop
Army Research Laboratory
Materials Directorate
AMSRL-MD
Watertown, MA 02172-0001

S. J. Bless
Institute for Advanced Technology
4030-2 W. Braker Lane
Austin, TX 78759-5329

W. J. Bruchey
Army Research Laboratory
Weapons Technology Directorate
AMSRL-WT
Aberdeen Proving Ground, MD
21005-5066

G. Bulmash
Army Research Laboratory
Weapons Technology Directorate
AMSRL-WT-TA
Aberdeen Proving Ground, MD
21005-5066

Kyu Cho
Army Research Laboratory
Materials Directorate
AMSRL-MA
Watertown, MA 02172-0001

S. Chou
Army Research Laboratory
Materials Directorate
AMSRL-MA
Watertown, MA 02172-0001

R. Clifton
Brown University
Division of Engineering
Providence, RI 02912

J. A. Collins
U.S. Air Force Armament Laboratory
AD/MNW
Eglin Air Force Base, FL 32542-5434

J. W. Coltman
Simula Inc.
10016 South 51st Street
Phoenix, AZ 85044

D. Curran
SRI International
333 Ravenswood Avenue
Menlo Park, CA 94025

D. Dandekar
Army Research Laboratory
Materials Directorate
AMSRL-MA
Watertown, MA 02172-0001

J. Dehn
Army Research Laboratory
Weapons Technology Directorate
AMSRL-WT-TA
Aberdeen Proving Ground, MD
21005-5066

K. Epstein
DOW Chemical USA
Ordnance Systems, 800 Building
Midland, MI 48667

J. C. Foster, Jr.
U.S. Air Force Armament Laboratory
AD/MNW
Eglin Air Force Base, FL 32542-5434

K. Frank
Army Research Laboratory
Weapons Technology Directorate
AMSRL-WT-TD
Aberdeen Proving Ground, MD
21005-5066

G. Gazonas
Army Research Laboratory
Weapons Technology Directorate
AMSRL-WT-PD
Aberdeen Proving Ground, MD
21005-5066

W. Gillich
Army Research Laboratory
Weapons Technology Directorate
AMSRL-WT-TA
Aberdeen Proving Ground, MD
21005-5066

W. Gooch
Army Research Laboratory
Weapons Technology Directorate
AMSRL-WT-TA
Aberdeen Proving Ground, MD
21005-5066

Y. Gupta
Washington State University
Department of Physics
Pullman, WA 99163

G. T. Gray
Los Alamos National Laboratory
Los Alamos, NM 87545

W. Haskell
Army Research Laboratory
Materials Directorate
AMSRL-MA-PA
Watertown, MA 02172-0001

T. Holmquist
Alliant Techsystems, Inc.
7225 Northland Drive
Brooklyn Park, MN 55428

Y. Horie
North Carolina State University
Dept. of Civil Engineering
Raleigh, NC 27607

C. Hubbard
Army Research Laboratory
Materials Directorate
AMSRL-MA-CA(APG)
Aberdeen Proving Ground, MD
21005-5066

K. Iyer
U.S. Army Research Office
P. O. Box 12211
Research Triangle Park, NC 27709

G. Johnson
Alliant Techsystems, Inc.
7225 Northland Drive
Brooklyn Park, MN 55428

J. N. Johnson
Los Alamos National Laboratory
MS B221
Los Alamos, NM 87545

R. Katz
Army Research Laboratory
Materials Directorate
AMSRL-MD
Watertown, MA 02172-0001

P. Kingman
Army Research Laboratory
Weapons Technology Directorate
AMSRL-WT
Aberdeen Proving Ground, MD
21005-5066

K. Kimsey
Army Research Laboratory
Weapons Technology Directorate
AMSRL-WT
Aberdeen Proving Ground, MD
21005-5066

R. W. Kocher
Advanced Research Projects Agency
Land Systems Office
3701 North Fairfax Drive
Arlington, VA 22203-1714

J. Lankford
Southwest Research Institute
6220 Culebra Road
San Antonio, TX 78284

D. Lassila
L-35
Lawrence Livermore National Laboratory
Livermore,CA 94550

K. T. Leighton
Lanxide Armor Products, Inc.
1300 Marrows Road
P. O. Box 6077
Newark, DE 19714-6077

D. Lovelace
Army Missile Command
AMSMI-RD-ST-WF
Redstone Arsenal, AL 35898-5240

D. Mandell
Los Alamos National Laboratory
MS F663
Los Alamos, NM 87545

M. Manghnani
Mineral Physics Group
University of Hawaii
2525 Correa Rd.
Honolulu, HA 96822

H. W. Meyer
Army Research Laboratory
Weapons Technology Directorate
AMSRL-WT-TA
Aberdeen Proving Ground, MD
21005-5066

M. Meyer
Univ. of Calif. at San Diego
Dept. of Applied Mech. & Eng. Sciences
La Jolla, CA 92093

J. D. Morrow
FMC Corporation
Ground Systems Division
1107 Coleman Avenue Box 367
San Jose, CA 95103

S. Nemat-Nasser
Univ. of Calif. at San Diego
Dept. of Applied Mech. & Eng. Sciences
La Jolla, CA 92093

T. Nicholas
Air Force Wright Aeronautical Labs.
Air Force Systems Command
Materials Laboratory
Wright-Patterson AFB, OH 45433

D. Orphal
California Research and Technology, Inc.
5117 Johnson Drive
Pleasanton, CA 94566

R. Palicka
CERCOM, Inc.
1960 Watson Way
P. O. Box 70
Vista, CA 92083

R. Paricio
Coors Ceramics Company
600 Ninth Street
Golden, CO 80401

A. Prakash
Army Research Laboratory
Weapons Technology Directorate
AMSRL-WT-WD
Aberdeen Proving Ground, MD
21005-5066

W. W. Predebon
College of Engineering
Michigan Technological University
Houghton, MI 49931

G. F. Raiser
Washington State University
Department of Physics
Pullman, WA 99163

E. Rapacki
Army Research Laboratory
Weapons Technology Directorate
AMSRL-WT-TA
Aberdeen Proving Ground, MD
21005-5066

A. M. Rajendran
Army Research Laboratory
Materials Directorate
AMSRL-MA
Watertown, MA 02172-0001

G. Randers-Pehrson
Army Research Laboratory
Weapons Technology Directorate
AMSRL-WT
Aberdeen Proving Ground, MD
21005-5066

G. Ravichandran
Graduate Aeronautical Laboratories
California Institute of Technology
MS 105-50
Pasadena, CA 91125

M. Scheidler
Army Research Laboratory
Weapons Technology Directorate
AMSRL-WT
Aberdeen Proving Ground, MD
21005-5066

S. Segletes
Army Research Laboratory
Weapons Technology Directorate
AMSRL-WT
Aberdeen Proving Ground, MD
21005-5066

M. Slavin
Army Research Laboratory
Materials Directorate
AMSRL-MA
Watertown, MA 02172-0001

D. Steinberg, MS L35
Lawrence Livermore National Laboratory
P. O. Box 808
Livermore, CA 94550

J. Thompson
U.S. Army Tank-Automotive Command
AMSTA-RSS
Warren, MI 48397-5000

D. J. Viechniki
Army Research Laboratory
Materials Directorate
AMSRL-MA
Watertown, MA 02172-0001

T. Weerasooriya
Army Research Laboratory
Materials Directorate
AMSRL-MA-PD
Watertown, MA 02172-0001

T. Wright
Army Research Laboratory
Weapons Technology Directorate
AMSRL-WT
Aberdeen Proving Ground, MD
21005-5066